

**Masterarbeit**

zur Erlangung des akademischen Grades

Master of Science im Fach Physik

**Optimizing the triggering strategy for the detection of  
cosmic rays with the Radio Neutrino Observatory  
Greenland (RNO-G)**

von

Lilly Marie Pyras

geboren am 10. Dezember 1995

in Kassel, Deutschland

Gutachterinnen:

Dr. Anna Franckowiak

Prof. Dr. Anna Nelles

Mathematisch-Naturwissenschaftliche Fakultät

Institut für Physik

Humboldt-Universität zu Berlin

Eingereicht am 6. November 2020

## Abstract

A promising technique to measure neutrinos above 10 PeV is the detection of radio signals generated by the Askaryan effect. The effect is caused by neutrino-induced particle cascades in dense media e.g. ice. Starting in 2021, RNO-G, a new detector using this technique and containing in-ice detector strings will be deployed in Greenland. One of the main challenges of the data analysis will be distinguishing between a cosmic ray muon and a real neutrino event. By building the detector with surface antennas we can use the established method of radio detection of air showers to identify incoming muons and use these signals as veto mechanism in the neutrino detection. An efficient veto trigger will lend higher confidence in identifying neutrinos and prevent the false positive neutrino detection caused by muons. To obtain an efficient veto, a surface trigger mechanism has to be developed and optimized. The trigger is based on the trace envelope in a frequencyband from 80 MHz to 180 MHz. A coincidence of two channels is required in order to trigger. One RNO-G station will be sensitive to air showers from  $1 \times 10^{17}$  eV on. The expected number of detected cosmic rays is  $3.17 \pm 1.69$  per day and station. The overall veto efficiency on a muon event is 29 %.

## Zusammenfassung

Eine vielversprechende Technik, um Neutrinos mit einer Energie größer als 10 PeV zu messen, ist die Detektion von Radiowellen, die durch den Askaryan-Effekt erzeugt werden. Der Effekt basiert auf Teilchenkaskaden in dichten Medien (z.B. Eis), die durch ein Neutrino ausgelöst werden. Ab 2021 wird in Grönland das Radio Neutrino Observatory (RNO-G) gebaut. Eine große Herausforderung in der Datenanalyse wird sein, eine echte Neutrinomessung von einem gemessenen Myon zu unterscheiden, das von einem Luftschauer erzeugt wurde. Da der Detektor mit Antennen an der Oberfläche ausgestattet wird, ist es möglich, die etablierte Technik der Radiodetektion von Luftschauern zu nutzen, um Myonen zu identifizieren. Dieses Signal kann als Veto in der Neutrinodetektion verwendet werden, um so einer falsch positiven Neutrinodetektion vorzubeugen. Um ein effizientes Veto zu erreichen, muss ein Triggermechanismus für den Oberflächendetektor entwickelt und optimiert werden. Der Trigger basiert auf der Einhüllenden der Wellenform in einem Frequenzbereich von 80 MHz bis 180 MHz. Um zu triggern, ist eine Koinzidenz von zwei Kanälen erforderlich. Eine RNO-G Station ist sensitiv für Luftschauer mit einer Energie von  $1 \times 10^{17}$  eV oder höher. Die erwartete Anzahl an detektierten Luftschauern ist  $3.17 \pm 1.69$  pro Tag und Station. Die Veto-Wahrscheinlichkeit für ein Myon-Event liegt bei 29 %.

# Contents

<b>1</b>	<b>Introduction</b>	<b>1</b>
<b>2</b>	<b>Radio detection of neutrinos</b>	<b>5</b>
2.1	Shower development . . . . .	5
2.1.1	Of cosmic ray induced air showers . . . . .	6
2.1.2	Of neutrino induced showers in ice . . . . .	10
2.2	Radio emission . . . . .	11
2.2.1	From air showers . . . . .	12
2.2.2	From neutrino induced showers in ice . . . . .	15
2.3	Experimental approaches . . . . .	17
2.3.1	Previous experiments . . . . .	17
2.3.2	Concept of RNO-G . . . . .	20
2.4	Radio background . . . . .	25
2.4.1	Atmospheric muon background . . . . .	25
<b>3</b>	<b>Triggering radio signals</b>	<b>32</b>
3.1	Signal chain . . . . .	32
3.2	Envelope trigger . . . . .	37
3.3	Triggering strategy . . . . .	41
<b>4</b>	<b>Monte Carlo simulations</b>	<b>46</b>
4.1	Air shower set and procedure . . . . .	46
4.2	Noise . . . . .	51
4.3	Threshold and frequency band . . . . .	54
4.4	Coincidence . . . . .	61
4.5	Optimal trigger settings . . . . .	64
<b>5</b>	<b>Efficiency analysis</b>	<b>66</b>
5.1	Air shower efficiency . . . . .	66
5.2	Expected number of events . . . . .	68
5.3	Muon veto efficiency . . . . .	70
5.4	Implications for RNO-G and further improvements . . . . .	76

<b>6 Summary and Conclusions</b>	<b>78</b>
<b>References</b>	<b>80</b>
<b>List of Abbreviations</b>	<b>88</b>
<b>Acknowledgements</b>	<b>90</b>

# 1 Introduction

When looking in the sky, not only does light from the sun and other objects reach us, but also all kinds of particles which are invisible to our eyes. While a typical astronomer observes the radiation in the electromagnetic spectrum, an astroparticle physicist measures particles such as atomic nuclei or neutrinos connected with astronomical objects. In contrast to typical particle physicists, who work with man-made accelerators to produce the particles of interest (which are then measured by a corresponding detector), astroparticle physicists do not have a man-made accelerator. Astrophysical particles stem from astronomical objects and can reach higher energies than any man-made accelerator developed to date. The challenge is that the particle type is not known before the detection, as well as the place where the particle interacts. Moreover, the sources itself are still unknown.

A particle of special interest is the neutrino. Neutrinos are ideal messengers to identify sources of ultra high energy (UHE) cosmic rays in the universe. The main mechanism at the origin of neutrinos is the production of pions in the interactions of cosmic rays with other hadrons or photons. The pions produced later decay into  $\gamma$ -rays in case of neutral pions ( $\pi^0 \rightarrow \gamma + \gamma$ ) or produce neutrinos  $\nu$  in case of charged pions. The charged pion decays into a muon and a muon-neutrino, the muon can later decay into an electron and an electron-neutrino ( $\pi^\pm \rightarrow \mu^\pm + \nu_\mu \rightarrow e^\pm + \nu_e + \nu_\mu$ ). Because neutrinos are electrically neutral, their trajectories will not be bent by the galactic and inter-galactic magnetic fields, meaning that their arrival direction will point back directly to their production site. Because neutrinos only interact weakly, they can escape from denser regions in the universe, where acceleration of hadrons may occur and then propagate unhindered over long distances. This is in contrast to the highest energy cosmic rays, whose range is limited by interactions with matter and in particular by the background photon field such as extra-galactic background light, the infra-red background, or the cosmic microwave background. The observation of high-energy neutrinos from astronomical objects provides incontrovertible evidence for cosmic-ray acceleration, which is in contrast to  $\gamma$ -rays, which can also be created by inverse Compton scattering.

IceCube, the neutrino observatory at South Pole, has measured the neutrino energy spectrum to above 1 PeV, which are the highest-energy neutrinos ever observed [42, 51, 2]. In Fig. 1 the neutrino flux measured by IceCube is shown, together with the diffuse flux

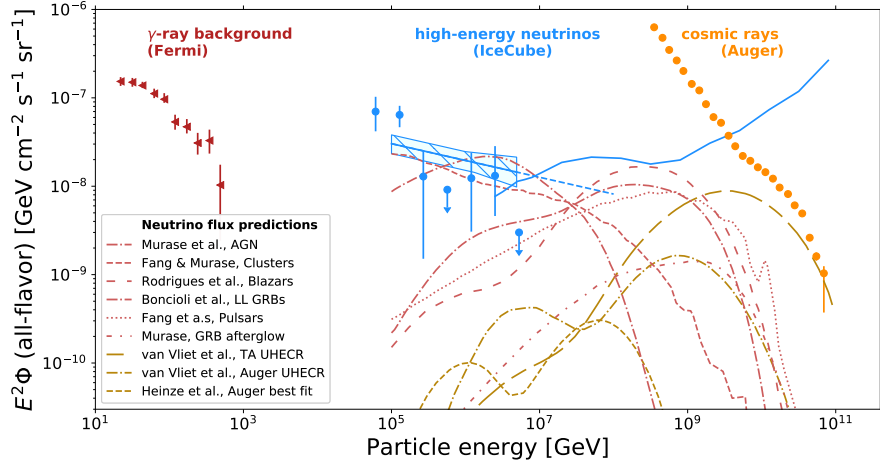


Figure 1: A multi-messenger view of the high-energy universe. Shown are the the  $\gamma$ -ray measurements from Fermi, the IceCube neutrino measurements and the fit to the muon neutrino spectrum, as well as the spectrum of ultra-high energy cosmic rays as reported by the Pierre Auger Observatory. Between  $10^{14}$  eV and  $10^{20}$  eV models are shown, predicted neutrinos from sources (in light red) and those from the interaction of the ultra-high energy cosmic rays with various photon backgrounds (in dark yellow). Fig. from [63].

of  $\gamma$ -rays measured by Fermi [5] and the cosmic-ray spectrum measured by Auger [1]. The similar energy density of the three spectra let us suspect a common origin. The Figure also shows the gap in observations of UHE neutrinos beyond the energies reachable by IceCube.

The Radio Neutrino Observatory Greenland (RNO-G) is one effort to measure UHE neutrinos. It is also capable to detect cosmic rays. In dense media, e.g. ice, neutrinos can induce particle cascades which then create radio emission. This radio emission is detectable with radio antennas. The same effect is known for cosmic ray induces showers in air. To detect a sufficient number of these neutrinos monitoring large target masses is required. Greenland has a natural occurrence of radio transparent ice, where this detector will be built starting in 2021. In Fig. 2 the expected sensitivity for the full array of 35 stations is shown, compared to existing experiments and predicted fluxes. RNO-G gets close to predicted IceCube like fluxes of the astrophysical neutrinos above 100 PeV. Neutrinos at this energies could stem from interactions of ultra high energy cosmic rays with photon fields like the extra-galactic background light, the infra-red background, or the cosmic microwave background [63]. The flux and spectrum of these neutrinos

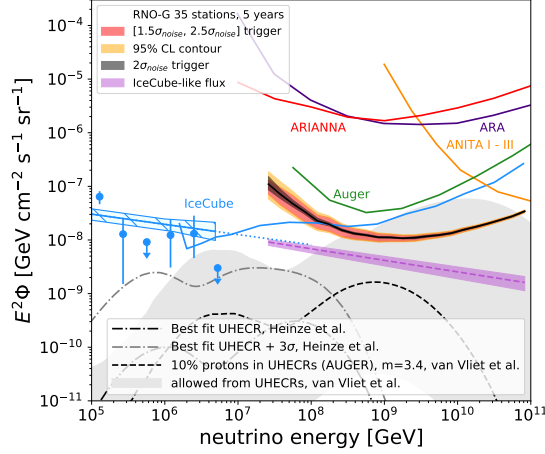


Figure 2: The five-year sensitivity of RNO-G to the all-flavor diffuse flux for 35 stations, compared with existing experiments and several predicted fluxes. The red band represents the sensitivity band for a range of trigger options. The purple band depicts 90% CL upper limits for an IceCube-like flux. RNO-G will be able to set constraints on several models of energetic astrophysical neutrinos such as neutrinos from AGN jets and pulsars, as well as cosmogenic neutrinos. Fig. from [63].

are related to the mass composition of ultra high energy cosmic rays. Measurements of RNO-G could constrain models for cosmogenic neutrinos assuming a significant proton fraction in UHE cosmic-rays.

This thesis deals with the radio detection of cosmic rays as part of RNO-G. It is equipped not only with antennas deep in the ice, but also with a surface antennas to detect cosmic rays. They can be used to calibrate the total system and to reduce the background stemming from the surface. This thesis aims to provide a trigger strategy to detect air showers and optimize the different trigger parameters. Sec. 2 *Radio detection of neutrinos* is divided in four subsections, focusing on different parts of the radio detection. Sec. 2.1 will introduce the physics behind shower development, while Sec. 2.2 will explain how the radio emission is created. Both sections are distinguish between the cosmic ray case in the atmosphere and the neutrino case in ice. It follows a discussion of different experimental approaches and a detailed description of RNO-G. Sec. 2.4.1 states the current knowledge of the expected muon background for the detector and suggests to implement surface antennas to veto on a muon event in case of an air shower detection. Sec. 3 provides an insight into the hardware used in the signal chain following the surface antennas and unfolds the multidimensional problem of the trigger strategy. In the following Sec. 4



the procedure and the results of detailed Monte Carlo simulations are presented. Sec. 5 evaluates the calculated parameters and estimates the efficiency in detecting air showers and veto on muon events.

## 2 Radio detection of neutrinos

The phenomena of extensive air showers was discovered by Pierre Victor Auger and collaborators in 1938 [18]. Over the last years the radio detection of air showers has become an established technique to measure cosmic rays [71]. Following this approach, several experiments aim for the radio detection of neutrinos. Due to their low cross-section, most neutrinos pass the atmosphere unhindered without inducing a particle shower. The likelihood of an interaction increases with the density of the medium. Therefore, a neutrino induced particle shower is more likely to be measured in a large volume of e.g. ice or rock. The radio emission generated by particle cascades in dense media was proposed in 1962 by Gurgen Askaryan [17]. By now, the first radio-neutrino detectors operate successfully and the quantitative understanding of the radio emission from particle cascades in dense media has increased [73]. The non-detection of neutrinos so far led to an upper limit at energies of  $E_\nu > 10^{19}$  eV [46].

The following sections explain the shower development of air showers (Sec. 2.1.1) and neutrino induced shower in ice (Sec. 2.1.2). Afterwards the radio emission of the particle cascades will be explained. The section dealing with neutrinos build on the previous sections. Afterwards different experimental approaches are introduced. Sec. 2.4 deals with other sources of radio emission, and the muon background.

### 2.1 Shower development

To understand the radio emission created by a particle shower, it is essential to understand the underlying processes of these phenomena, namely the evolving particle cascade. Air showers are cascades of secondary particles initiated by a primary particle such as a gamma ray photon, electron, positron, proton, nuclei or neutrino which strikes an atom's nucleus (see Fig. 3). These cascades are conceptually similar to the ones developing in dense media, like water or ice. Air showers are much more extensive with length scales of kilometers while particle cascades in dense media develop within meters [73]. Both showers propagate through their medium at a speed close to the speed of light.

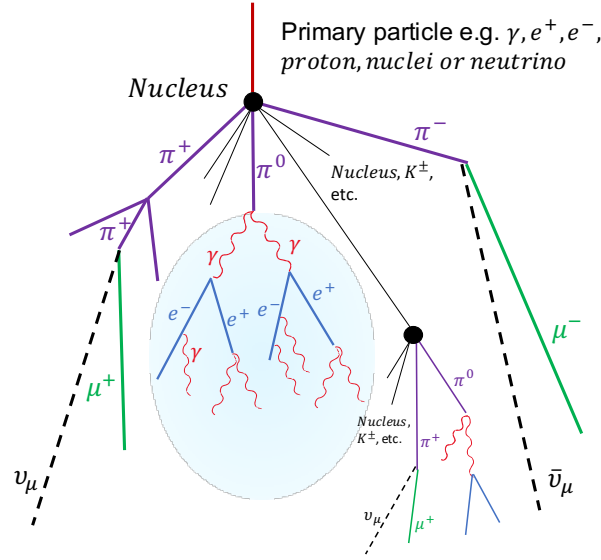


Figure 3: Simplified sketch of an air shower. Real air showers contain more particle types than displayed. Shown are different processes that lead to the electromagnetic component (blue backed), the hadronic component (violet), and the muonic component (green). Radio detectors detect emission only from the electromagnetic cascade.

### 2.1.1 Of cosmic ray induced air showers

In the first interaction of an air shower, the incoming primary particle interacts hadronically with an atom's nucleus of the atmosphere. The interaction produces mostly pions ( $\pi^0, \pi^\pm$ ) and other hadrons, such as kaons, protons and neutrons. The pions produced have different decay modes and interaction channels. Because neutral pions have a short decay length, ( $l_{\text{decay}} = \gamma \cdot \tau \cdot c = \gamma \cdot 2.5 \times 10^{-8} \text{ m}$ , where  $\gamma$  is the relativistic gamma factor) they decay into a photon pair ( $\pi^0 \rightarrow \gamma + \gamma$ , with a branching fraction of 98.82%) before they can interact. This decay leads to the *electromagnetic component* of the shower.

The dominant process in the electromagnetic component is the production of photons by Bremsstrahlung ( $e^\pm \rightarrow e^\pm + \gamma$ ) and the production of electron and positron pairs by a photon ( $\gamma \rightarrow e^- + e^+$ ). Simultaneously occurring are the Coulomb scattering of electrons, and ionization and excitation by electrons. At low energies, the Compton effect with a wavelength shift of the photon plays a role. The created electrons, positrons and photons continue to interact, on average after one radiation length, and the cascade continues. The shower development stops when the individual particle energy of  $e^\pm$  and  $\gamma$  falls below the critical energy and the inelastic interaction cross-section drops to zero.

The *critical energy* is the energy at which losses by ionization are equal to losses by radiation<sup>1</sup> [41]. The critical energy can be written in the form  $E_c \approx \frac{a}{Z+b}$ , where  $a$  is the energy loss due to ionization,  $b$  is the contribution from the bremsstrahlung and  $Z$  is the atomic number of the medium. An empirical approximation for solids and liquids is  $E_c^{\text{s,l}} \approx \frac{610 \text{ MeV}}{Z+1.24}$  and for gases  $E_c^{\text{gas}} \approx \frac{710 \text{ MeV}}{Z+0.92}$ , they differ mainly because of the density effect. The value of an electron in air is  $E_c^{\text{air}} \approx 84 \text{ MeV}$  [41]. Particles below the critical energy will continue to propagate until they reach the ground, but because they are low in energy, the particles are likely to be captured by atmospheric molecules. Therefore only a small fraction of the electromagnetic component reaches the ground.

The charged pions and the remaining protons and neutrons fuel the *hadronic component* of the shower. As long as their decay length ( $l_{\text{decay}} = \gamma \cdot \tau \cdot c = \gamma \cdot 7.8 \text{ m}$ ) is larger than their interaction length, the high-energy charged pions ( $\pi^\pm$ ) will continue to interact with nuclei in the atmosphere, creating more pions and expanding the shower. In contrast to the electromagnetic cascade, hadrons interact via the strong force. Due to the strong force's short range, interactions are more rare and hadrons can penetrate the atmosphere unhindered over several interaction lengths. When the energy of the pions becomes so low that their decay length is shorter than their interaction length, the charged pions decay due to the weak interaction. Most often, they decay into a muon and a muon neutrino  $\pi^\pm \rightarrow \mu^\pm + \bar{\nu}_\mu$ . The resulting particles travel without further interaction towards the ground. The muon can later decay into an electron and its corresponding neutrino:  $\mu^\pm \rightarrow e^\pm + \bar{\nu}_\mu + \bar{\nu}_e$ . The decay time of a muon is usually longer than the relativistic time that the muon needs to reach the ground.

Both, electromagnetic and hadronic cascade reach a point at which the number of particles in the shower is at a maximum and the shower is largest. After this point the number of particles decreases until only neutrinos and muons are left.

The height above the ground at which the first interaction takes place is related to the type of primary particle. Heavy nuclei such as iron have a higher cross-section with air, which will lead on average to an earlier interaction than protons. Due to shower universality the height of the first interaction is related to the height of the maximum shower development [54]. The concept of *air shower universality* emerged initially from cascade theory, expressing the similarity of all showers in a broad sense, and allowed

---

<sup>1</sup>A different definition of the critical energy is used by Rossi and Greisen [65].

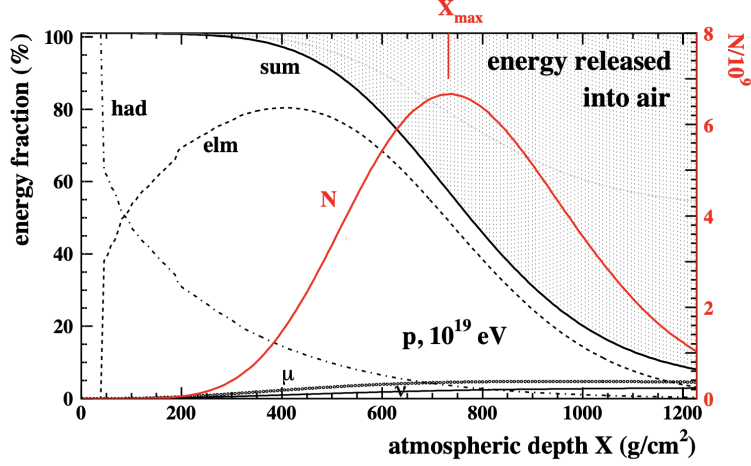


Figure 4: Energy flow in extensive air shower as obtained by CORSIKA shower simulations for an individual  $10^{19}$  eV primary proton event. The energy fractions stored in hadrons, electromagnetic particles, muons, and neutrinos are shown. The difference between their sum to the initial energy indicates the total amount of energy already released into the air (shaded area). The red line is the cascade profile  $N(X)$ , where  $X_{\max}$  indicates the maximum number of shower electrons and positrons. Figure adapted from Ref. [62].

showers to be described in terms of the primary energy and the shower age [41].

In Fig. 4 the longitudinal development of an air shower is illustrated. At the beginning, the hadronic cascade develops. From its products the electromagnetic cascade starts and continues to be fed in the subsequent shower process. A significant energy fraction is transferred to the electromagnetic component, consequently the energy left in the hadrons decreases exponentially. The energy fraction of muons and neutrinos is almost negligible ( $\sim 5\%$ ), as can be seen only at later stages of the shower development. Most of the initial energy is deposited into the atmosphere. The maximum of energy stored in electromagnetic particles (dashed line) is reached before the shower maximum (red line). The shower maximum is defined as the depth where the shower contains the largest electron multiplicity. This difference is due to the fact that at an early cascade stage, a large energy fraction is deposited in only a few high-energy particles. The high-energy particles then create new particles, to which the energy is transferred.

Simple models such as the Heitler model for electromagnetic cascades (1936) [45], later expanded by Matthews for extensive air showers [56], can be used to describe the shower development and calculate shower properties, such as location of the shower maximum,

and the related energy and number of particles. Once the shower development of a proton induced shower is understood, heavier primary particles can be modeled as a superposition of proton showers. The shower maximum of a simple proton induced shower is described by [56] with:

$$X_{\max}^{\text{proton}} = X_0 + \lambda_r \ln \frac{E_0}{3N_{\text{ch}}E_c^e} \quad (1)$$

Where  $X_0 = \lambda_{\text{int}} \ln 2$  is the atmospheric depth at which the first interaction occurs and  $\lambda_{\text{int}}$  is the interaction length of the primary proton.  $\lambda_r$  indicates the radiation length,  $E_0$  the primary energy,  $N_{\text{ch}}$  the multiplicity of charged particles and  $E_c^e$  the critical energy of an electron. In the shower development the primary energy  $E_0$  is distributed to the sub-showers with  $E_0/A$ , where  $A$  is the mass of the nucleus (e.g. the proton number).

The maximum of an hadronic shower can be written as:

$$X_{\max}^A = X_0 + \lambda_r \ln \frac{E_0}{3N_{\text{ch}}E_c^e A} \quad (2)$$

or simplified as:

$$X_{\max}^A \sim \lambda_{\text{int}} + \lambda_r \ln \frac{E_0}{A}. \quad (3)$$

This relation shows that the shower maximum is reached earlier for heavier nuclei, because their interaction length is shorter (e.g.  $\lambda_{\text{int}}^{\text{proton}} \approx 70 - 90 \frac{\text{g}}{\text{cm}^2}$  and  $\lambda_{\text{int}}^{\text{iron}} \approx 15 - 20 \frac{\text{g}}{\text{cm}^2}$  [41]). This makes it possible to distinguish between lighter and heavier primary particles.

With advances in computation, Monte Carlo simulation for air showers become possible. In contrast to the simplified models, the Monte Carlo calculation is based on stochastic processes, which rely on the interaction cross-section of single particles. The programs include all relevant processes, such as particle propagation, interaction and/or decay needed to simulate complete air showers in space and time. Software like CORSIKA [44] include a realistic model of the atmosphere, the magnetic fields and an interface for detector simulations. The applied cross-section are measurements from accelerators that get as close to a realistic cascade development as possible. Currently, cross-section at the highest energy level are missing and have to be extrapolated, introducing new uncertainties. The Monte Carlo simulations used for this thesis are described in Sec. 4.

### 2.1.2 Of neutrino induced showers in ice

The shower development of a neutrino induced shower in ice is conceptually similar to air showers described previously. A neutrino strikes a nucleon in the ice which induces a particle cascade.

The neutrino interactions are distinguished in charged-current (CC) interactions mediated by  $W^+$  and  $W^-$  bosons and neutral current (NC) reactions, where a  $Z^0$  boson is exchanged. In a CC interaction the particle type before and after the interaction differ:

$$\nu_l + \text{nucleon} \longrightarrow l + \text{hadron(s)} \quad (4)$$

with  $l = e, \mu, \tau$  and nucleon could be  $p$  or  $n$ . In an NC interaction the lepton flavor does not change, as in:

$$\nu_l + \text{nucleon} \longrightarrow \nu_l + \text{hadron(s)} \quad (5)$$

The neutrino reactions which lead to particle cascades in dense media occur in nucleons of the nuclei of the ice. For the different neutrino flavors and their antiparticles the reactions shown in Tab. 1 can take place.

From these considerations it becomes clear that all neutrino flavors ( $\nu_e, \nu_\mu, \nu_\tau$ ) create only a hadronic particle cascade when interacting via an NC reaction because the lepton stays unchanged.

In a CC reaction the lepton changes. Therefore a  $\bar{\nu}_e$  creates almost immediately two showers, a hadronic and an electromagnetic one, initiated by the resulting electron. The same holds true for a  $\nu_e$  and the resulting positron. At high energies, the

Quasi-elastic reactions	Inelastic reactions
$\bar{\nu}_e + p \longrightarrow e^+ + n$	$\bar{\nu}_e + N \longrightarrow e^+ + \text{hadrons}$
$\nu_e + n \longrightarrow e^- + p$	$\nu_e + N \longrightarrow e^- + \text{hadrons}$
$\bar{\nu}_\mu + p \longrightarrow e^+ + n$	$\bar{\nu}_\mu + N \longrightarrow \mu^+ + \text{hadrons}$
$\nu_\mu + n \longrightarrow e^- + p$	$\nu_\mu + N \longrightarrow \mu^- + \text{hadrons}$
$\bar{\nu}_\tau + p \longrightarrow e^+ + n$	$\bar{\nu}_\tau + N \longrightarrow \tau^+ + \text{hadrons}$
$\nu_\tau + n \longrightarrow e^- + p$	$\nu_\tau + N \longrightarrow \tau^- + \text{hadrons}$

Table 1: Charged-current neutrino reactions.  $N$  stands for a nucleon ( $p$  or  $n$ ). Analogous reactions can be listed for elastic and inelastic neutral-current reactions, whereby the same lepton stands on either side of the arrow. Table adapted from Ref. [41].

Landau–Pomeranchuk–Migdal (LPM) effect becomes relevant and the cross-section of bremsstrahlung and pair production is reduced. This leads to an elongation and distortion in the shower. Also, the creation of multiple sub-showers over tens of meters is possible.

In the CC reaction of  $(\bar{\nu})_\mu$  and  $(\bar{\nu})_\tau$  a hadronic shower is created as well. The resulting leptons ( $\mu^\pm$  and  $\tau^\pm$ ) propagate through the medium generating lots of secondary showers over a range of kilometers until they decay [36]. Muons lose most of their energy through bremsstrahlung, pair production, and nuclear interactions inducing new sub-showers. Taus radiate mainly electron-positron pairs, but larger amounts of energy via photo-nuclear interaction, which leads to hadronic cascades. Also the decay of a tau into hadronic and leptonic channels can create showers.

## 2.2 Radio emission

The existence of radio emission of air showers has been known since the 1960s [6], but the limitations of the analog instruments available at the time made it seem impossible to gain an insight into the underlying processes. The emission mechanisms were not well understood and no viable theory was available at that time to make predictions of the field strength to be expected or the effective frequency bands in which such transient effects would occur.

In recent years, the interest in radio detection has increased again. With detailed Monte Carlo shower simulations, digital data-taking and processing methods, the understanding of radio emission has made considerable progress. Currently several radio-based air shower detectors like AERA [40], LOFAR [47] and Tunka-Rex [72], as well as radio-based neutrino detectors like ARIANNA [57] and ARA [10] are operational and are taking data.

Two mechanisms have been identified to be the main contributors to the radio emission: The geomagnetic emission, caused by the deflection of charged particles in the Earth’s magnetic field, and the Askaryan effect, caused by a time-varying negative net charge in the shower front (see Fig. 5).



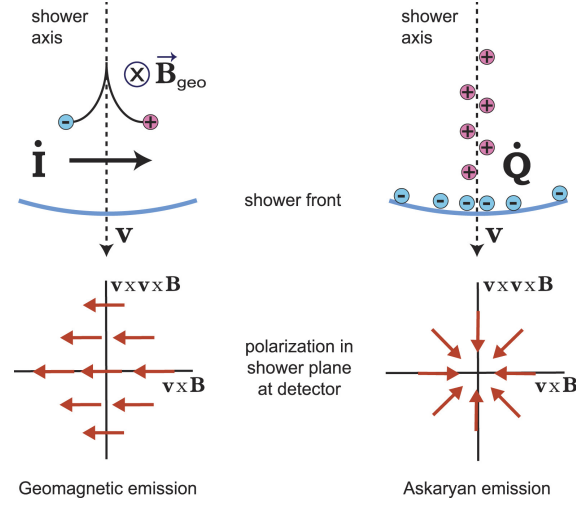


Figure 5: The two main emission processes of radio signals from particle cascades: Geomagnetic emission (left) and charge-excess (Askaryan) emission (right). The geomagnetic emission due to the induction of a transverse current is polarized in the direction of the geomagnetic Lorentz force (east-west for vertical air showers, see bottom left). In air it is typically stronger than the radially polarized Askaryan emission (bottom right) due to the time variation of the net charge excess in the shower front, which is the main mechanism in dense media. Figure from Ref. [71].

### 2.2.1 From air showers

In the geomagnetic field of the Earth the moving electrons and positrons in the shower front are separated in opposite direction due to the Lorentz Force  $\vec{F}_L = q \cdot \vec{v} \times \vec{B}$  ( $q$  is the particle charge,  $\vec{v}$  the velocity vector or propagation direction and  $\vec{B}$  is the magnetic field vector). This leads to a net-drift of the electrons and positrons moving perpendicularly to the shower axis, which can be described as a transverse current ( $\dot{q} = I$ ). This current varies in time ( $\dot{I}$ ), depending on the amount of charge present in the air shower and the interaction with molecules in the atmosphere [69]. This mechanism is referred to as the *geomagnetic effect* or as the time varying transverse current. As this is the dominant component in radio emission of extensive air showers, the signal strength scales with the number of electrons and positrons in the shower, which scales with the energy of the primary particle. Furthermore, the electric field of the emission  $\vec{E}$  scales with the angle between shower direction ( $\vec{v}$ ) and the local magnetic field ( $\vec{B}$ ), following the relation  $\vec{E} \sim \vec{v} \times \vec{B}$  [68].

The so-called *Askaryan effect* [17], or charge-excess, is based on the fact that the shower front has a net negative charge which varies over time. Shortly summarized, the

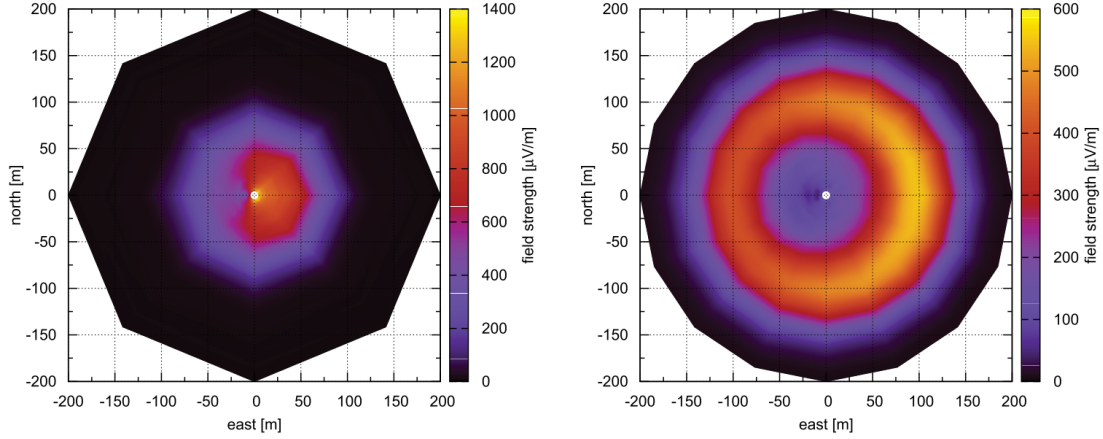


Figure 6: Footprint simulations done with COREAS of the total field strength for a vertical  $10^{17}$  eV air shower induced by a proton (left) and an iron atom (right) in a 300 MHz to 1200 MHz frequency band. The asymmetry due the interference of geomagnetic and Askaryan emission is visible. The shape of the footprint is influenced strongly by the distance to the shower maximum and the frequency range. Fig. from Ref. [48].

charge excess arises due to the ionization of the surrounding media by the moving shower. The now free electrons move with the shower front, whereas the heavier positive ions stay behind (see 5). The underlying process which leads to that charge asymmetry has to do with the fact that the matter in the medium contains only electrons and no positrons. The interactions leading to ionization and free electrons can be described by Møller scattering ( $e^- + e^-_{\text{medium}} \rightarrow e^- + e^-$ ), Bhabha scattering ( $e^+ + e^-_{\text{medium}} \rightarrow e^+ + e^-$ ) and Compton scattering ( $\gamma + e^-_{\text{medium}} \rightarrow \gamma + e^-$ ). Moreover, Bhabha scattering decelerates the shower positrons. Electrons and positrons annihilate ( $e^+ + e^- \rightarrow \gamma + \gamma$ ), which leads again to a negative charge excess in the shower front. The Askaryan effect plays a sub-dominant role in air showers, while it is the dominant contribution to the radio signal of showers in dense media.

Both time varying effects induce linearly polarized radiation, but differ in their polarization direction. It is useful to describe the polarization in a coordinates system where one axis is parallel to the shower's direction of movement  $\vec{v}$ . The second axis,  $\vec{v} \times \vec{B}$ , is perpendicular to both,  $\vec{v}$  and the geomagnetic field  $\vec{B}$ . The third axis is perpendicular to the others two axes and called  $\vec{v} \times (\vec{v} \times \vec{B})$ . In Fig. 5 the polarization for geomagnetic and charge excess emission are shown in the  $\vec{v} \times \vec{B}$  and  $\vec{v} \times (\vec{v} \times \vec{B})$  plane.

The polarization of emission produced by the geomagnetic effect is aligned with the

Lorentz force ( $\vec{v} \times \vec{B}$ ). The polarization angle is therefore independent of observer location with respect to the shower axis.

The varying net-charge responsible for the Askaryan effect is symmetrically distributed in a radial position around the shower axis. Therefore, the induced electric field vector points radially towards the shower axis, so the orientation of the electric field vector depends on the location of an observer with respect to the shower axis.

The measured polarization angle, combining both effects, is consequently also dependent on the position of the observer. The electric field of the resulting emission can be written as:

$$\vec{E} \propto -\sin(\alpha) \cdot \vec{e}_{\vec{v} \times \vec{B}} + a \cdot \vec{e}_r \quad (6)$$

where  $\vec{e}_r$  is a unit vector pointing towards the shower axis and  $a$  is the so-called relative charge excess strength, which varies from event to event and is also dependent of the distance to the shower axis. The interference of co-aligned and opposite aligned polarization leads to an observed asymmetric radiation pattern around the shower axis (see Fig. 6).

For wavelengths larger than the thickness of the emitting shower front, and for  $c \sim c_0$ , the vectorial electric field adds up coherently (MHz regime). This leads to a coherent broad-band pulse.

The media in which the particle shower propagates adds another effect. Because the refractive index in air is  $n_{\text{air}} > 1$  with a typical value at sea level of  $n_{\text{air}} \approx 1.0003$  and decreasing with atmospheric density to higher altitudes, the radio waves travel slightly more slowly through the air (speed of light in the media) than the relativistically moving particle front. This causes a strong forward-beaming of the emission, and to a compression of the emission in time (Cherenkov-compression). Under a certain observing angle, the radiation emitted by the whole shower arrives simultaneously. This leads to an enhancement of the pulse with a length of a few nanoseconds [78].

The Cherenkov-compression introduces an additional geometric component to the emission pattern. The main enhancement can be found at the so-called Cherenkov angle, given by:

$$\cos(\theta_c) = \frac{1}{n \cdot \beta} \quad (7)$$

where  $n$  is the refractive index and  $\beta = \frac{v}{c}$  the relativistic velocity. For air,  $\theta_c^{\text{air}}$  has a value of  $1^\circ$ , which leads to a typical radius on the ground of 100 m to 200 m around the

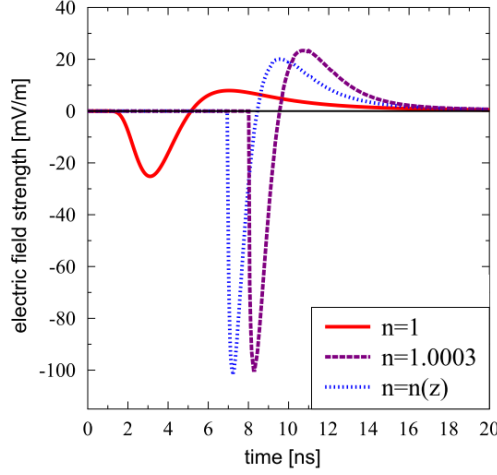


Figure 7: Simulated radio pulses of a  $5 \times 10^{17}$  eV air shower as received by an observer at an axis distance of 100 m. The refractive index  $n$  has been set to unity (vacuum), 1.0003 (sea level) and a realistic gradient in the atmosphere  $n(z)$ , demonstrating the resulting time compression of the radio pulses. The particle distribution is approximated to have no lateral extent. Fig. from Ref. [49].

shower axis for a vertical  $10^{17}$  eV air shower. Fig. 7 illustrates the difference between the refractive index of the vacuum, air and an atmospheric model dependent on the height. This relation makes clear that a good understanding of the media and their properties is an important factor.

### 2.2.2 From neutrino induced showers in ice

In dense media the only relevant emission mechanism for the radio emission is the Askaryan effect, where a charge excess arises due to the ionization of the surrounding media by the moving shower. The shower dimensions are in the order of meters, and coherence extends to high frequencies, typically GHz. Large formations of dense media such as ice exist in e.g. Antarctica or Greenland with an attenuation length in radio frequencies of a few hundred meters.

As in the atmosphere, the refractive index of the ice causes a compression of the emission in time due to Cherenkov like effects (see Sec. 2.2.1). The refractive index of ice is  $n_{\text{ice}} \approx 1.78$ , which leads to a Cherenkov angle of  $\theta_c^{\text{ice}} \approx 56^\circ$ . A significant emission strength is only observed close to the Cherenkov angle [12]. In Fig. 8 typical radio pulses for an in-ice shower in time and frequency domain are shown. In the time-domain the signal itself is a broad-band bipolar pulse only a couple of nanoseconds long. At the

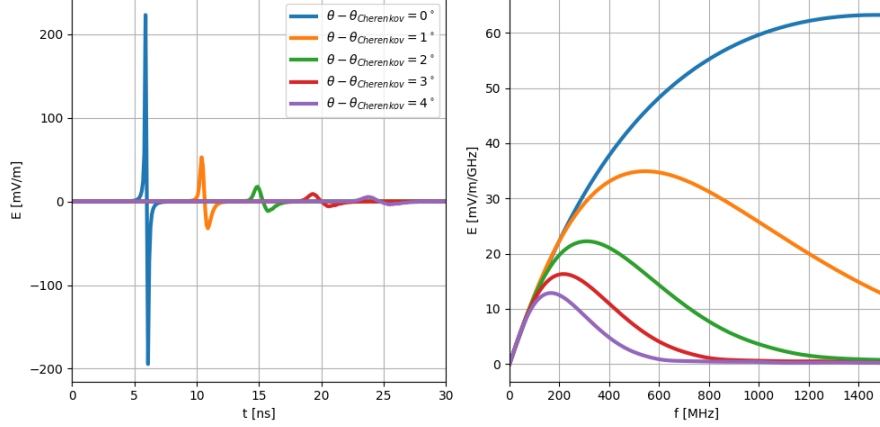


Figure 8: Electric field waveforms (left) and spectra (right) of the radio signal emitted at different viewing angles relative to the Cherenkov angle by a shower depositing 1 EeV in ice. For better readability, the waveforms have been shifted in time. Fig. from Ref. [63].

Cherenkov angles coherence is given over frequencies ranging from a few MHz to tens of GHz. If the viewing angle is off the Cherenkov angle, the coherence disappears first at high frequencies, which indicates that the Cherenkov ring is rather narrow at high frequencies and broader at low frequencies. Therefore, the signal changes with the viewing angle. As the viewing angle increases the high frequencies disappear and only low frequencies are detectable.

As described in Sec. 2.1.2, a neutrinos which interaction via a NC reaction creates only a hadronic particle cascade. The radio emission from hadronic component is negligible. Due to the decay of neutral pions into two photons ( $\pi^0 \rightarrow \gamma + \gamma$ ) an electromagnetic component is created which then emits a radio signal.

In a CC interaction of a  $\nu_e$  the resulting electron creates almost immediately two showers, a hadronic and an electromagnetic one. At low energies, the showers are created roughly at the same place and the radio emission interferes mostly constructively. At high energy the shower development is influenced by the LPM effect which leads to an elongation and distortion in the shower. Also, the creation of multiple sub-showers over tens of meters is possible. The electromagnetic shower maximum can be far away from the hadronic shower maximum, so the showers can interfere or their radio signal can be seen as two (or more) independent pulses.

In the CC reaction of  $(\bar{\nu})_\mu$  and  $(\bar{\nu})_\tau$  a hadronic shower is created as well. The resulting

leptons ( $\mu^\pm$  and  $\tau^\pm$ ) propagate through the medium generating lots of secondary showers over a range of kilometers until they decay [36]. The appearance of a tau neutrino induced shower closely followed by a shower generated by the created taus decay is described as double-cascade neutrino signature, and reported by IceCube in 2019 [75]. Simulations also indicate that the background of atmospheric muons from cosmic rays which create a shower through catastrophic energy loss is non-negligible for in-ice arrays [36] and will be investigated in Sec. 2.4.1

## 2.3 Experimental approaches

An overview of modern radio detectors and their measurements can be found [73]. In Tab. 2 selected major modern radio experiments for cosmic ray and neutrino detection are listed. In [49] radio detectors are roughly divided into first generation digital experiments, such as CODALEMA (COsmic Detection Array with Logarithmic ElectroMagnetic Antennas) [15] and LOPES (LOFAR PrototypE Station) [31], which provided evidence for the geomagnetic and Askaryan emission mechanisms and several other proof-of-principle detections. The second generation digital experiments consist in particular of the Auger Engineering Radio Array (AERA) [74], the cosmic ray detection capabilities of the Low Frequency Array (LOFAR) [67] and the Tunka Radio Extension Tunka-Rex [26]. The experiments have different key aspects, like the air-shower detection in parallel to astronomical observations by LOFAR or the cross-calibration of radio and air-Cherenkov measurements with Tunka-Rex. AERA aims at a variety of different technical and scientific goals, which makes it a pathfinder for future applications of the radio technique.

The radio detection in dense media is most advanced in ice. In the next section the key aspect of previous experiments such as ANITA, ARA and ARIANNA will be introduced. Afterwards the concept of the Radio Neutrino Observatory Greenland (RNO-G) will be described.

### 2.3.1 Previous experiments

The first prototype experiments for the radio detection of neutrinos in ice were RICE (Radio Ice Cherenkov Experiment) [53], and AURA (Antarctic Under-ice Radio Array)

Experiment	Operation period	Aiming at cosmic rays	Aiming at neutrinos	Medium of ra- dio emission
Yakutsk array	since 1972	x		air
RICE	1999–2010		x	ice
LOPES	2003–2013	x		air
CODALEMA	since 2003	x		air
ANITA(-lite)	first flight 2004	x	x	air and ice
AURA	2006–2009		x	ice
TREND	2009–2014	x		air
AERA	since 2010	x		air
ARA	since 2010	(x)	x	ice
LOFAR	since 2011	x	x	air and moon
Tunka-Rex	since 2012	x		air
ARIANNA	since 2012	x	x	air and ice
TAROGÉ	since 2014	x		air
RNO-G	in 2021	(x)	x	ice (and air)
SKA-low	planned	x	x	air and moon
GRAND	planned	x	x	air and rock
IceCube Gen2	planned	(x)	x	ice (and air)

Table 2: Major modern radio experiments for high-energy cosmic rays and neutrinos. Current radio arrays for neutrino detection are still under construction and the starting year refers to first prototype setups. Tab. adapted from Ref. [73].

[55], both located at the South Pole. Ice, in comparison to other dense media, such as rock or the lunar regolith, has the advantage of a larger attenuation length of radio waves and the large available ice volumes in Antarctica and Greenland. For future large-scale detectors of several  $10 \text{ km}^3$  or  $100 \text{ km}^3$ , ice seems to be the medium of choice [43].

By now, the next generation of prototype arrays have been deployed. Most important are ARA (Askaryan Radio Array) [7, 9, 10, 14] close to IceCube at the South Pole, ARIANNA (Antarctic Ross Ice Shelf Antenna Neutrino Array) [13, 23, 25] on the Ross Ice Shelf on the Antarctic coast and ANITA (Antarctic Impulsive Transient Antenna), which is a balloon-borne experiment flying over Antarctica.

ARA currently runs with five stations at a frequency band of 150 MHz to 850 MHz. Each station features six in-ice strings at a depth of 200 m. The four receiver strings are equipped with two vertically-polarized birdcage dipole antennas (Vpol) and two ferrite-loaded slot antennas (Hpol) to resolve the radio signals. The two other strings contain a calibration unit. Some stations have four additional antennas at the surface for air-shower and background measurements [14]. One station has an extra phased array, which makes ARA the first deploying this technique into a bore hole [8].

ARIANNA currently consist of twelve stations, with four antennas each, searching for in-ice showers in the frequency band of 50 MHz to 1000 MHz [13]. The antennas are located just slightly below the ice surface. This location makes it possible to detect a downward going Askaryan pulse after it is reflected at the water interface below the ice. ARIANNA is also sensitive to radio signals of cosmic-ray air showers [23]. Without external infrastructure, the stations operate autonomously in low-power and wireless communication mode.

ANITA made its initial flight with its prototype ANITA-lite in 2004 [24]. It has flown four times on-board a balloon over Antarctica, searching for ultra-high-energy neutrinos. The 32 – 48 horn antennas which are sensitive to radio emission at high frequencies of 200 MHz to 1200 MHz, are placed below the balloon. In order to detect a neutrino signal, the neutrino first interaction has to be below the ice surface, going upwards to leave the ice itself. ANITA was the first radio-neutrino experiment to report the detection of cosmic ray induced air showers [70]. Most of the cosmic ray signals were not measured directly, but were detected after reflection on the ice. Several techniques used by ANITA are also applied in ground-based arrays, e.g., individual antennas are combined by interferometric



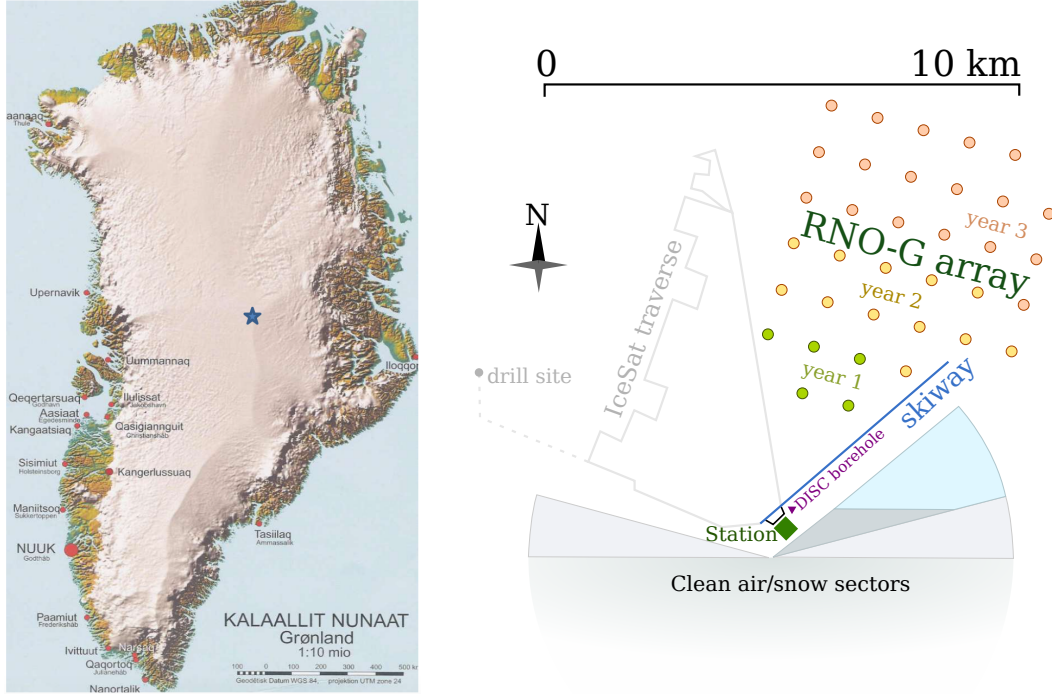


Figure 9: Left: Map of Greenland, the blue star marks Summit Station. Right: Map of the planned RNO-G array at Summit Station. Fig. from Ref. [63]

beamforming (as for LOPES) and polarization characteristics are used to discriminate air showers from background (as for AERA).

Currently, a proposals for a renewed ballooning effort are pending, as well as an extension of the ARIANNA array at Moore’s Bay. The existing ARA stations will continue to operate under the umbrella of IceCube and it successor IceCube Gen2.

### 2.3.2 Concept of RNO-G

The design of the Radio Neutrino Observatory Greenland (RNO-G) combines the experience gained with prior in-ice radio neutrino experiments, especially from ARA and ARIANNA. Located in Greenland at Summit Station ( $72^{\circ}35'46''$  N,  $38^{\circ}25'19''$  W, see Fig. 9) RNO-G will be atop of more than 3km of glacial ice that has been measured to be radio transparent [19] and with a  $\sim 100$  m deep firn layer that has been preliminarily characterized [29]. The detector (see Fig. 9) will include 35 stations, ten of them will be deployed in 2021. The whole detector will be powered by renewable energies, such as solar panels. The communication will be wireless via LTE.

Each station will consist of three in-ice strings at 100 m depth to measure particle

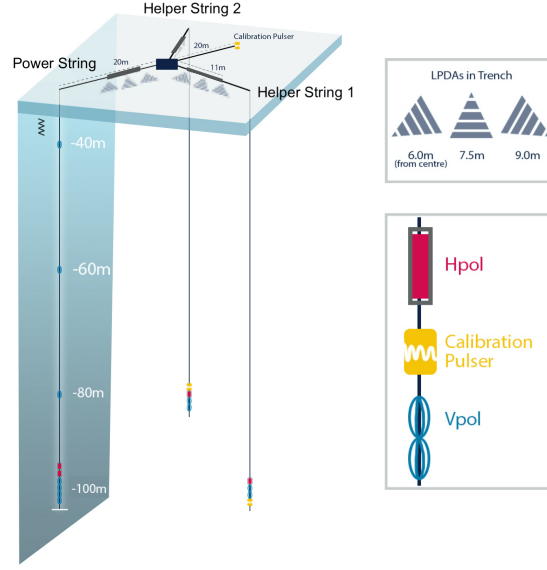


Figure 10: A single RNO-G station consists of three 100 m long in-ice strings with different antenna configurations. On the surface are nine LPDAs in total, three along each arm. They are covered by  $\sim 1$  m of snow. See Fig. 11 for the exact positions of the antennas. Fig. adapted from Ref. [63]

cascades in ice and a surface component that is also sensitive to cosmic rays (see Fig. 10 and Fig. 11). The strings will be arranged in a tri-point shape, with a distance of 20 m to the center.

The downhole antenna designs are driven by the 11.2" diameter of the boreholes. The vertically-polarized (Vpol) antennas will be a *fat dipole* design, which have an azimuthally symmetric beam pattern and usable bandwidth ranging from 150 MHz to 600 MHz [52, 20]. For horizontal polarization (Hpol), nearly azimuthally-symmetric cylindrical tri-slot antennas will be used. The Hpol antennas have a narrower usable bandwidth than the fat dipoles, due to their geometry in the narrow borehole (see Fig. 12).

The main string contains the interferometric phased array at  $\sim 100$  m depth, above two Hpol antennas, and three additional Vpol antennas with a 20 m spacing towards the surface. The phased array consists of four Vpols with an antenna spacing of 1 m. The phased array will trigger on radio signals of particle showers in ice in a frequency band of  $\sim 80$  MHz to  $\sim 240$  MHz. Due to the proximity of the antennas, the arriving signal is almost the same, except for a time delay. The trigger coherently sums the waveforms, giving a boost in signal-to-noise ratio (SNR), because the noise is expected not to be correlated (see Fig. 13).

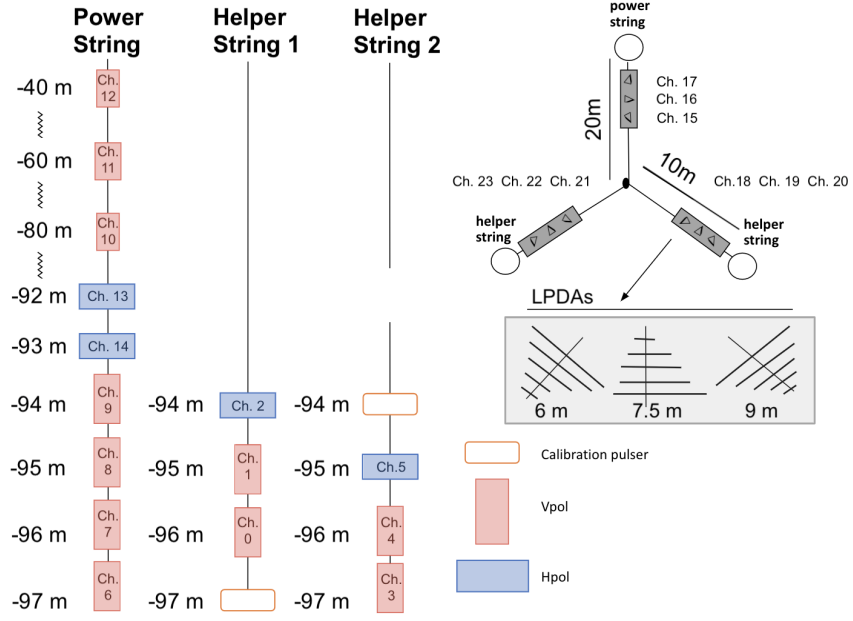


Figure 11: Schematic illustration of a RNO-G station. The channel number of one antenna is placed inside the antenna. Shown are the in-ice strings with the position of each antenna. The LPDAs are on the surface placed along the three arms. The position of the LPDAs is measured from the station center. The LPDA in the center of each arm is oriented upwards. The LPDA at 6 m is orientated diagonally downwards to the center, the one at 9 m is orientated diagonally downwards away from the center. Fig. adapted from Ref. [63]

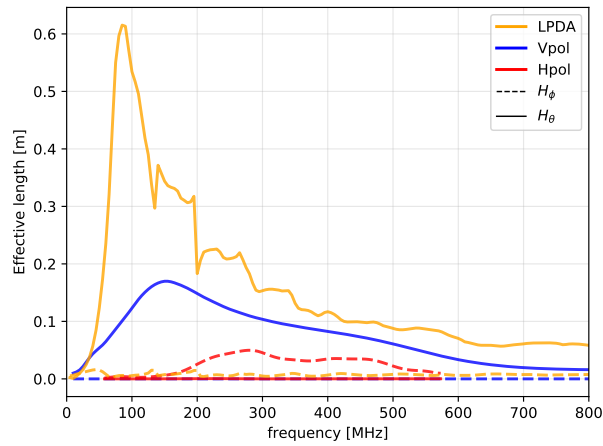


Figure 12: The absolute value of the effective length for the LPDA, Vpol and Hpol for the direction of maximum gain  $H_\theta$  (V-pol and LPDA) or  $H_\phi$  (H-pol). For detailed explanation of effective length and the signal chain see Sec. 3.1. Fig. from Ref [63].

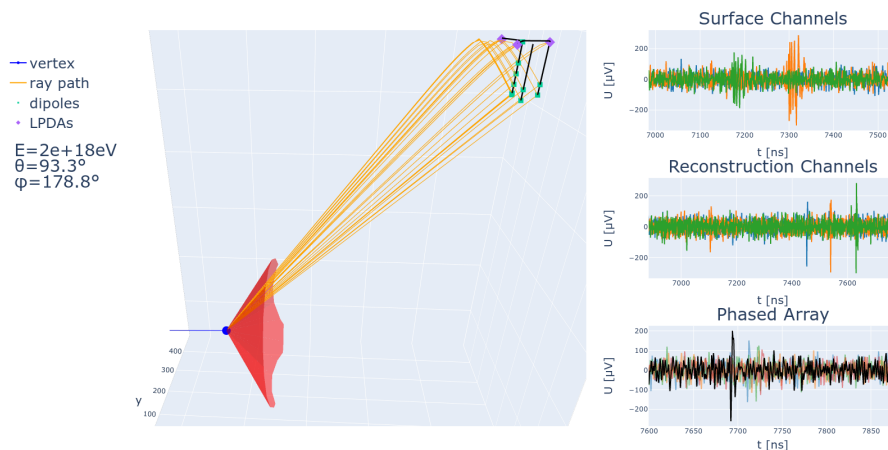


Figure 13: A simulated neutrino event in RNO-G showing the direct and reflected ray-paths to the antennas, the waveforms in the antennas, and the noise reduction obtained by the phased array (black vs. other colors, bottom row). The phased array combines the signals to increase the signal-to-noise ratio and reduce the trigger threshold [8]. This simulation and online event display are a result of the community-wide collaboration [38, 39]. For better visibility, selected channels are shown. Fig. from Ref. [63]

The three additional Vpols are used to reconstruct the vertex position of the first interaction and the arrival direction of the radio signal. The two Hpols improve the reconstruction possibilities of the full electric field. Due to their proximity, the Vpol antennas in the phased array should measure the same electric field, except for a time delay, as the Hpol antennas. Together they should provide sufficient information to reconstruct the polarization of the signal.

In order to reconstruct the azimuth angle of the arrival direction, three independent measurements with a sufficient distance between the Vpol antennas are needed. Therefore, one station consists of the main string and two additional helper strings. Each helper string has one Hpol, two Vpols and one calibration pulser between a depth of 94 m and 97 m. The Hpol antennas provide information for signals with a horizontal polarization component. The calibration pulser ensures a regular monitoring of the performance of the station and provides information about the position accuracy of all antennas.

The surface component consists of nine log-periodic dipole antennas (LPDAs), three at each detector arm with varying orientation (one upward facing and two diagonally-downward facing). LPDAs are broad-band sensitive, which helps determine the radio detection angle with respect to the Cherenkov cone, improving energy reconstruction

and pointing resolution. Although the surface component extends the neutrino effective volume only slightly, precision polarization measurements for all components and timing information for all events detected at the surface will be delivered. With these LPDAs, a clear separation of upgoing versus downgoing signals is provided. Due to their size the LPDAs have the largest gain of all employed antennas and will provide the best frequency coverage of the signals detected. Moreover, the surface channels measure air showers which can be used to reduce background.

## 2.4 Radio background

The three major sources of background for the detection of neutrinos are incoherent thermal noise, impulsive man-made noise, and radio impulses resulting from cosmic ray air showers and their remnants.

Man-made noise can be reduced by an optimal choice of measurement location. Narrow-band transmitters such as AM/FM radio frequencies or communication radio are the most dominant sources of interference. Short radio pulses are also created by any kind of electrical equipment, usually in combination with sparking (spark plugs, switches, etc.). ARA has proven that thermal background and man-made noise decreases for receivers deployed deeper in the ice [11].

The surface detector provides measurements to estimate the non-thermal background from the surface. The following section, Sec. 2.4.1, investigates the importance of muons stemming from cosmic ray air showers as a background.

The surface detector is exposed to further noise stemming from the Galaxy and introduces an irreducible noise floor. The diffuse emission, mostly from the Galactic plane, shows a strong contribution with an exponential spectrum [64] throughout the whole MHz-band. Air shower pulses are therefore only detectable above this noise level, when the cosmic ray had an energy above  $10^{16}$  eV. A detailed discussion about the galactic noise will follow in Sec. 4.2.

### 2.4.1 Atmospheric muon background

As a product of cosmic ray air showers muons are created that reach ground level (see Sec. 2.1.2). As they radiate in the ice, they can induce a particle cascade. The particle shower in the ice creates radio emission via the Askaryan effect (see Sec. 2.2.2). If the muon and the subsequent shower has sufficient energy, it could be measured by the detector (see Fig. 14).

The radio signal following a muon stems either from hadronic or electromagnetic particle cascade. For a radio detector, it would in principle look identical to the signal created by a neutrino-induced particle shower. The specifics of neutrino induced showers are explained in Sec. 2.1.2 and Sec. 2.2.2.

To estimate the number of expected muons, detailed simulations were made as shown

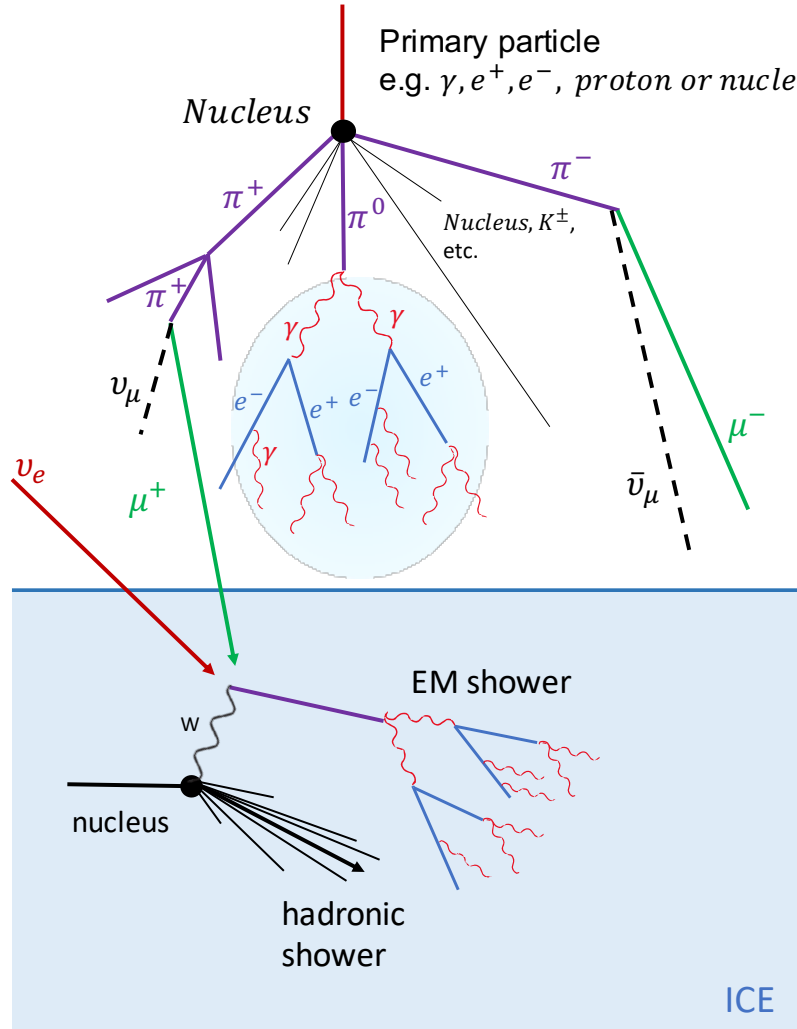


Figure 14: Illustration of an air shower above a volume of ice. In the ice, a particle cascade is visible as well. The in-ice shower could either be induced by an astrophysical neutrino (dark red arrow), or by a muon stemming from the air shower above (green arrow). To exclude the muon case, an air shower veto could be useful.

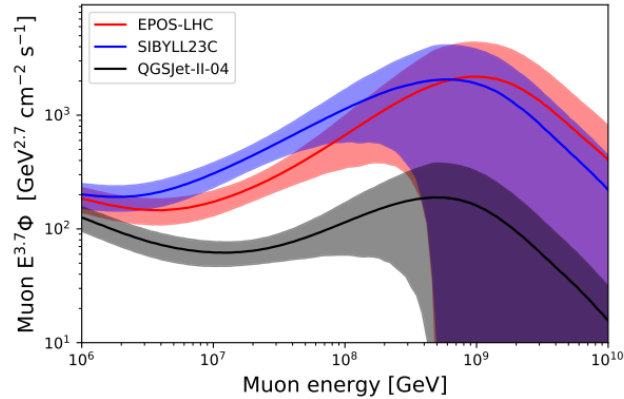


Figure 15: Muon flux rescaled with muon energy to the power of 3.7 and integrated on the upper hemisphere as a function of the muon energy. The different colours indicate the different interaction models. The shaded area represents the uncertainties due to cosmic ray flux models and hadronic interaction models (68% CL). Fig. from Ref. [36].

in [36]. Up to PeV scale, IceCube has directly measured the muon flux [3], above this energy the muon flux uncertainties are dominated by the cosmic ray flux uncertainties [32]. The muon flux was simulated for different interaction models, which predict a large range of possible muon fluxes [36]. Fig. 15 illustrates the muon flux integrated over the upper hemisphere. In the relevant energy scale, the predictions vary by about an order of magnitude.

For the radio detection of neutrinos, only muons which are capable of introducing a particle shower are relevant for the background. Therefore, a second set of simulations was made, propagating the muons to determine which ones create showers above the 1 PeV threshold. Afterwards the showers were applied to different detector configuration to calculate the number of triggers induced by these muons. From this, an estimation of the average effective area for each energy and zenith bin was made. The average number of events triggered by atmospheric muons can be obtained by multiplying the effective area with an incident muon flux integrated in an energy bin and a zenith band.

The results for a 35-station array at Summit Station per year, using a 100 m-deep dipole with an amplitude threshold between  $1.5\sigma_{\text{noise}}$  and  $2.5\sigma_{\text{noise}}$  as a proxy for the phased array are shown in Fig. 16. On the left-hand side the expected detected number of muons per year as a function of shower energy is shown, while Fig. 16, right, shows it as a function of cosmic ray energy. The shaded area shows the 68% CL interval for



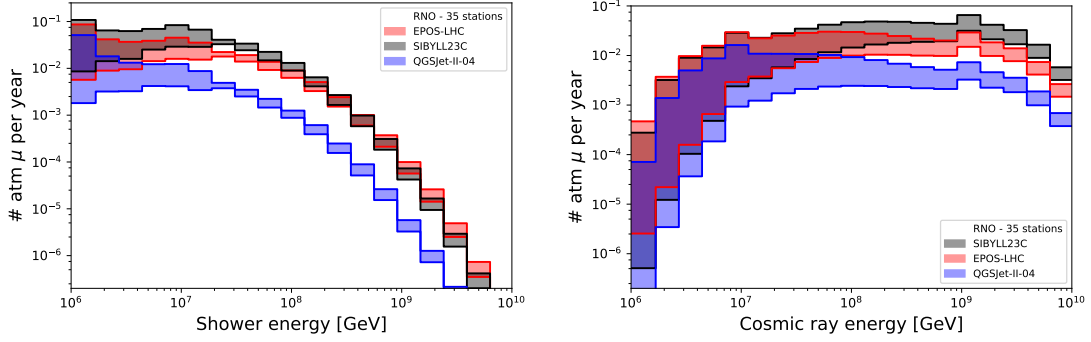


Figure 16: Number of atmospheric muons expected for a 35-station array at Summit Station. The phased array is modeled with dipoles having amplitude thresholds varying from  $1.5$  to  $2.5\sigma_{\text{noise}}$ , at 100 m of depth. Each color represents a different hadronic model, as specified in the legend. The bands include the range of expected events for the different simulated triggers as well as the 68% CL contour corresponding to the effective area uncertainty. Left: Number of expected atmospheric muons per year as a function of shower energy. Right: Same results, presented as a function of cosmic ray energy. Fig. from Ref. [63]

	$2.5\sigma_{\text{noise}}$ 68% CL LB	$2.0\sigma_{\text{noise}}$ average	$1.5\sigma_{\text{noise}}$ 68% CL UB
SIBYLL 2.3C	0.212	0.296	0.684
EPOS-LHC	0.129	0.173	0.444
QGSJet-II-04	0.031	0.044	0.180

Table 3: Number of expected atmospheric muons per year for a 35-station layout. Three hadronic models are shown. The numbers shown are the 68% CL lower bound for  $2.5\sigma_{\text{noise}}$  trigger (first column), the average values for a  $2.0\sigma_{\text{noise}}$  trigger (second column), and the 68% upper bound for a  $1.5\sigma_{\text{noise}}$  trigger (third column). See text for details.

the uncertainty due to cosmic ray flux, hadronic modeling and effective area. Each band represents the results for a hadronic interaction model.

The lower and upper bounds of the expected number of detected atmospheric muons per year for a 35-station layout, as well as the average number for a  $2.0\sigma_{\text{noise}}$  trigger, can be found in Tab. 3. Although the values seem benign, they imply that the expected muon flux is a non-negligible background, if the expected number of detected neutrino events in a 100-station array is about one per year. Since the predicted neutrino fluxes vary by about an order of magnitude, a cosmic-ray veto seems advisable [36].

Other parameters to distinguish a muon induced shower from a real neutrino event could be provided by the position of a reconstructed vertex and the particle arrival di-

rection. These calculations have been made by [36]. In Fig. 17 the vertices where the first interaction of a shower takes place for muons (left) and neutrinos (right). The distributions are similar in the way, that they are dominated by allowed ray-tracing paths. In contrast to the muon interaction vertices, neutrinos seem to interact deeper in the ice. Therefore, it might be possible to distinguish events on a statistical basis.

In Fig. 18 the zenith distributions for incoming particles (neutrinos in black, muons in red) are illustrated for two energy bins. Muons start to trigger at around  $40^\circ$ , which is also the elevation where neutrino events start to be observed. Near the horizon, the number of muons decreases due to absorption in earth, while neutrinos are still observable due to their low cross-section. Below the horizon ( $> 90^\circ$ ) the earth is opaque for neutrinos above tens of PeV, so few neutrinos are seen from below the horizon. Muons seem to peak around  $50^\circ$ , while neutrinos are more likely to come from close to the horizon. The combination of vertex position and arrival direction may allow the removal of a fraction of atmospheric muon background, given a good reconstruction of both parameters and at the cost of a reduced neutrino efficiency [36].

However, given all the uncertainties in cosmic ray flux and their composition, expected neutrino events etc. a cosmic ray veto seems useful. It was shown that the zenith angles from the incoming muons are typically more inclined than  $40^\circ$ , a value, where air shower detectors are sensitive. The associated air showers have energies above a few tens of PeV, which is coincidentally roughly the threshold for a sparse air-shower radio array. Moreover, a surface array of radio detectors is based on the same technology as in-ice radio arrays. The in-ice detector requires only additional antennas at the surface. Further investigation will be described in Sec. 4 and Sec. 5 and form the main research of this thesis.

In Fig. 19 the footprints for different inclined air showers are illustrated. The footprint scales with the zenith angle of the air shower, while the maximum amplitude is higher at vertical showers for the same shower energy. Therefore, horizontal air showers are more likely to be measured by a station of the detector if their energy is high enough. A quantitative study of the efficiency as a function of energy and arrival direction will follow in Sec. 5.

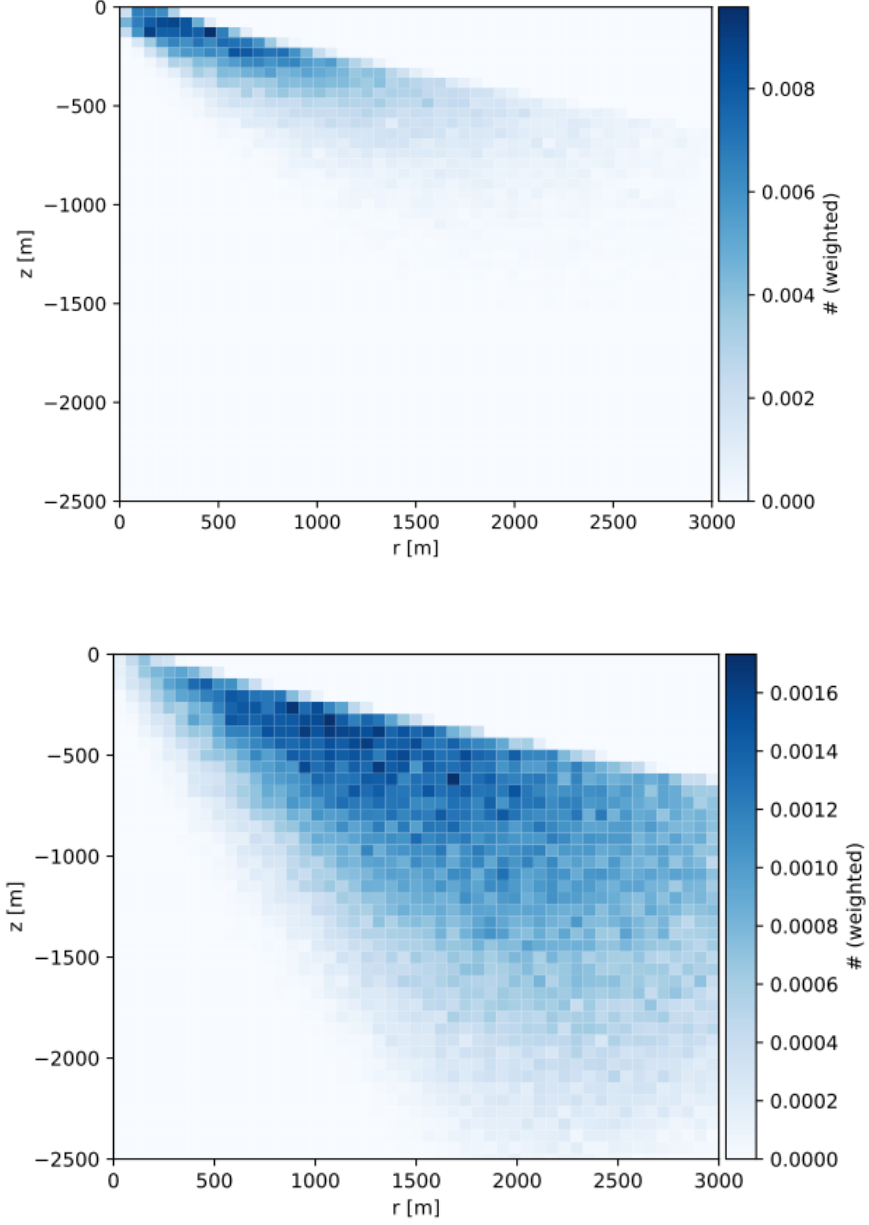


Figure 17: Top: 2D triggering muon vertex distribution as a function of radial and vertical distances to antenna, for a  $1.5\sigma_{\text{noise}}$  dipole at 100 m. Muon energies lie between 300 PeV and 6100 PeV. Bottom: same as top, but for triggering events induced by neutrino first interactions. Neutrino energies lie between 1200 PeV and 2300 PeV. Fig. from Ref. [36]

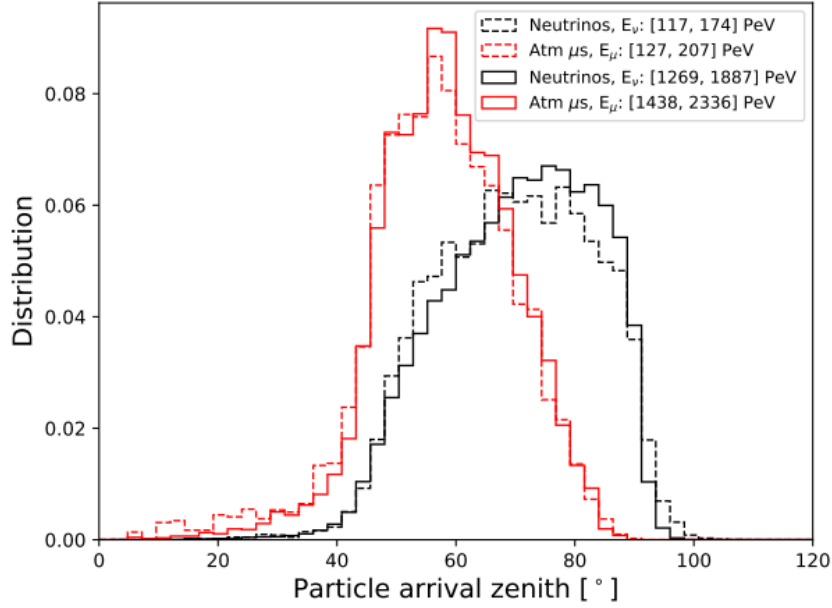


Figure 18: Neutrino (black) and atmospheric muon (red) zenith arrival directions. Solid and dashed lines indicate two different energy bins with ranges stated in the legend. For these two bins, the energy dependence seems to be weak. All the shown distributions are normalized to 1. The most delicate arrival direction is between  $60^\circ$  and  $80^\circ$ . Fig. from Ref. [36]

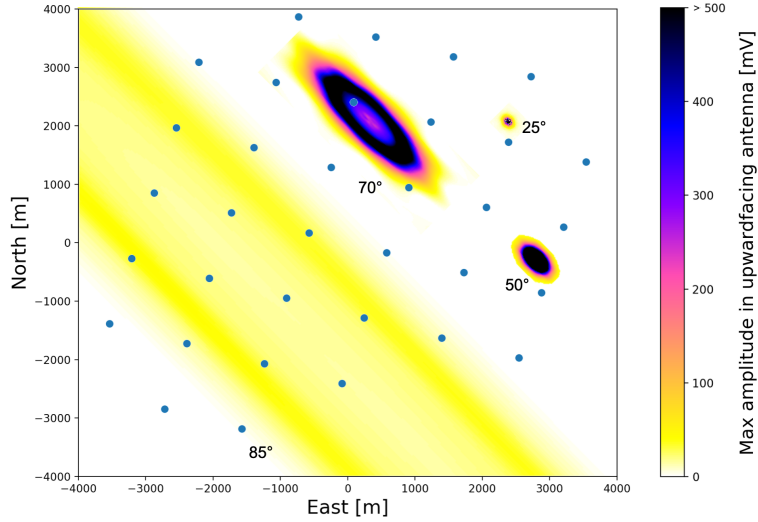


Figure 19: Different simulated radio air shower footprints. Simulations were done using CORSIKA and the site (magnetic field and height above sea level) for Greenland, including the response of upward facing logarithmic periodic dipole antennas. The air shower energy is  $3.2 \times 10^{18}$  eV for all showers, and the zenith angles as indicated in the figure.

### 3 Triggering radio signals

The RNO-G detector is planned to continuously measure and take data. In order to collect a feasible amount of data, a trigger is needed, which decides if the signal is stored or discarded. All signals that pass the trigger will be stored and analyzed later. By pre-selecting events, the trigger will determine the efficiency of the experiment. The in-ice detector will have the phased array as a trigger, while the surface detector will trigger on a simple threshold of the envelope from the LPDA traces. An efficient surface trigger will give higher confidence in identifying neutrinos and prevent false positive neutrino detections caused by muons. It is necessary to have a good understanding of the signal chain, the triggered quantities and a reasonable trigger strategy. This section gives an overview of the hardware used in the surface detector, the trigger set-up and the dependencies of the trigger parameters. A detailed explanation of the software based optimization will follow in Sec. 4.

#### 3.1 Signal chain

The electric field generated by the radio emission of an air shower contains two components  $E_\theta$  and  $E_\phi$  that denote two independent polarization directions. The electric field is contained in the plane spanned by the unity vectors  $\vec{e}_\theta$  and  $\vec{e}_\phi$  of a spherical coordinate system. In Fig. 20 the electric field of a cosmic ray induced shower is shown in the time domain (left-hand side) and in the frequency domain (right-hand side). The time trace shows a sharp nano-second pulse in the MHz regime while it has a broad spectrum in the frequency domain.

The electric field will eventually be measured by the surface antennas of the detector. RNO-G hosts nine logarithmic periodic dipole antennas (LPDA, Create CLP-5130-2N) per station with various orientations. They are sensitive in a range of 105 MHz to 1300 MHz. The antennas are covered by two meters of snow, which has a higher refraction index than air, therefore the frequency  $f$  decreases.

$$f_{\text{firn}} = \frac{f}{n_{\text{firn}}} \quad (8)$$

For  $n_{\text{firn}} = 1.3$  the lower limit of the sensitivity decreases from 100 MHz to  $\sim 77$  MHz. The signal measured with the antenna depends on the incoming field  $\vec{E}(t)$  and its direction

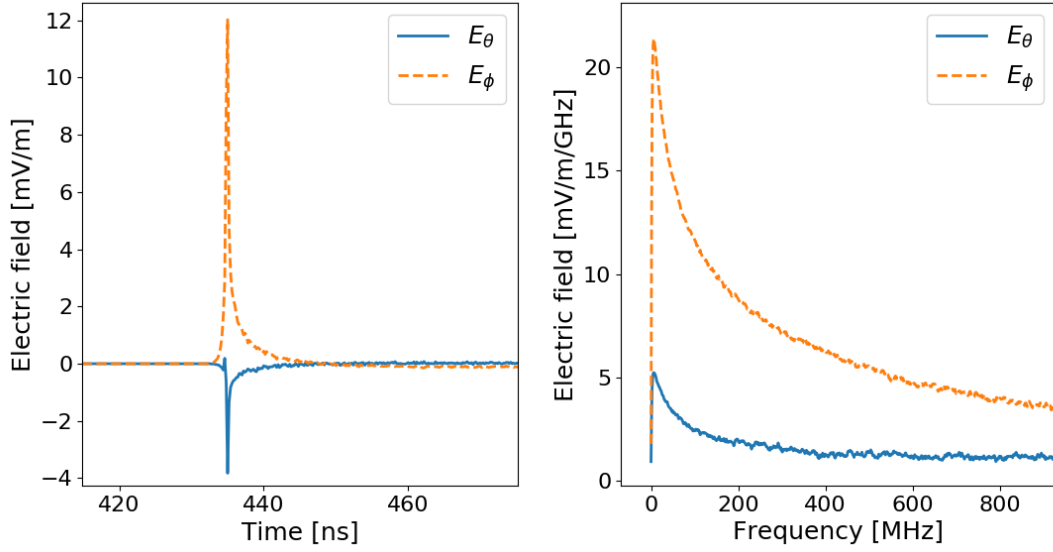


Figure 20: Shown are the two components  $E_\theta$  and  $E_\phi$  of the electric field generated by the radio emission of a cosmic ray induced shower. The shower energy is  $10^{18}$  eV, arriving at  $\theta_{\text{ant}} = 55^\circ$ ,  $\phi_{\text{ant}} = 0^\circ$ . The left figure shows the radio pulse in the time domain. On the right-hand side the frequency spectrum is shown.

with zenith angle  $\theta$  and azimuthal angle  $\phi$ . In simulations the angles of the arriving signal are defined with respect to the antenna as shown in Fig. 21. The zenith angle with respect to the antenna is named  $\theta_{\text{ant}}$  and measured from the longitudinal axis of the antenna,  $\phi_{\text{ant}}$  describes the azimuth where  $0^\circ$  is perpendicular to the longitudinal axis of the antenna and its tines.

The response pattern of an antenna to an electric field can be described as the vector effective length (VEL). The VEL of the antenna represents the mapping between the voltage induced over the antenna and the electric field of the signal [61].

$$\mathcal{U}(\theta, \phi, f) = \vec{H}(\theta, \phi, f) \cdot \vec{\mathcal{E}}(f) \quad (9)$$

Where  $\mathcal{U}$  is the Fourier transformed observed voltage,  $\vec{H}(\theta, \phi, f)$  is the antenna response pattern expressed in terms of the VEL and  $\vec{\mathcal{E}}(f)$  is the Fourier transformed electric field.

In Fig. 22, the VEL for a signal arriving at  $\theta_{\text{ant}} = 55^\circ$  and  $\phi_{\text{ant}} = 0^\circ$  is depicted. Within the bandwidth the VEL decreases with increasing frequency. The additional variations of the VEL in the  $\phi$  component within the frequency band occur due to the interplay of the LPDA's dipole elements, which resonate at different frequencies [4]. The corresponding induced voltage over the antenna is shown in Fig. 23. The pulse broadens in the time

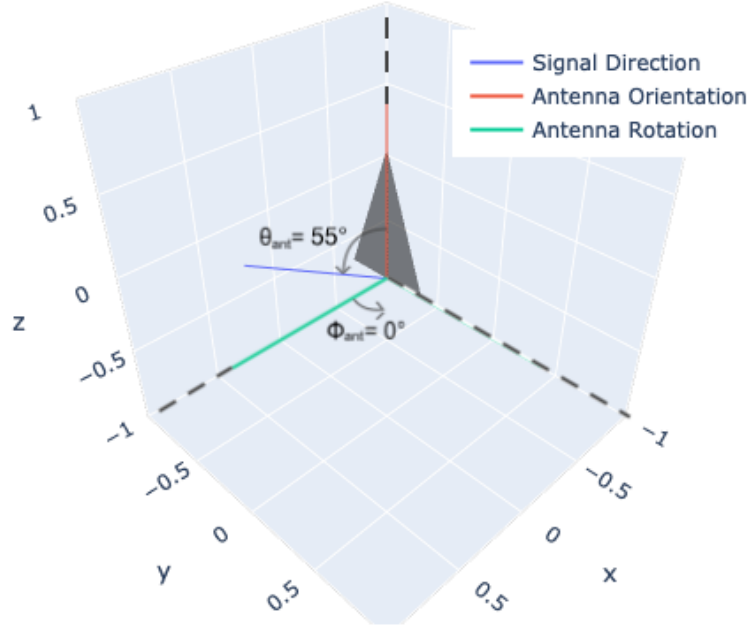


Figure 21: Visualization of a LPDA structure. The orientation (red) indicates the direction of the antenna tip (a rotation along the y-axis), the rotation (green) specifies the direction perpendicular to the tines (a rotation along the z-axis). The antenna orientation and rotation are always perpendicular to each other. The blue line represents a signal arriving at  $\theta_{\text{ant}} = 55^\circ$  and  $\phi_{\text{ant}} = 0^\circ$ . The zenith angle  $\theta_{\text{ant}}$  is counted from the top, the azimuth angle  $\phi_{\text{ant}}$  counterclockwise from the x-axis of the coordinate system.

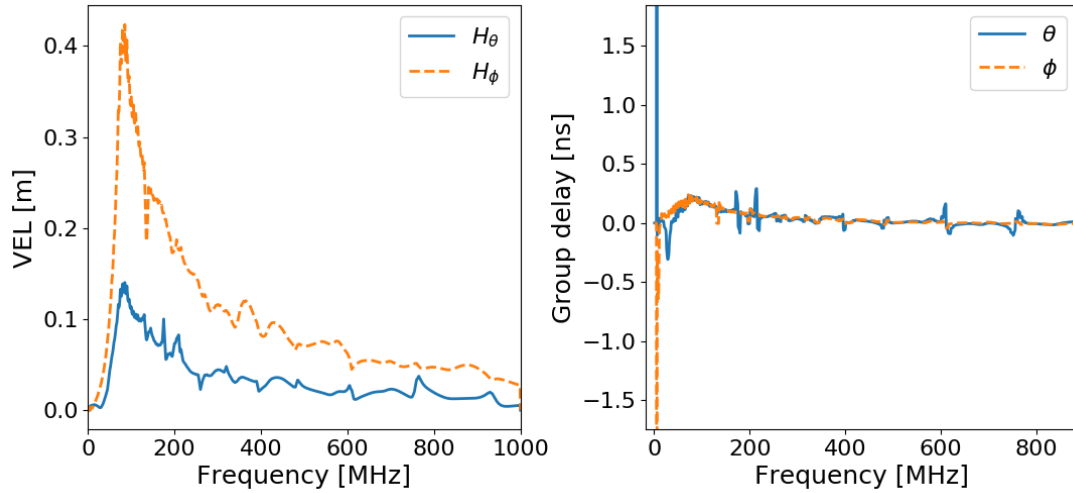


Figure 22: The absolute value of the vector effective length of the LPDA for the signal shown in Fig. 20. The signal arrives at  $\theta_{\text{ant}} = 55^\circ$  and  $\phi_{\text{ant}} = 0^\circ$  with respect to the antenna.

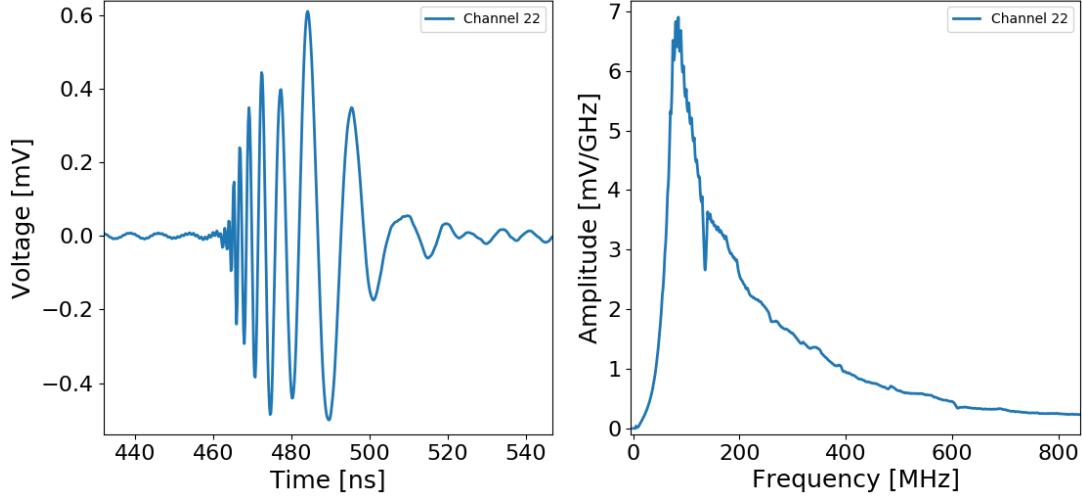


Figure 23: Simulated induced antenna voltage for the electric field shown in Fig. 20. The signal arrives at  $\theta_{\text{ant}} = 55^\circ$  and  $\phi_{\text{ant}} = 0^\circ$  with respect to the antenna. The shown signal is without amplification. Left: timed domain. Right: Frequency domain.

domain due to losses in the high frequency range, and because the antennas have group delay, that induces dispersion which broadens the pulse.

A schematic visualization of the whole signal chain of the surface detector is shown in Fig. 24. After the signal is measured by the antenna, it will be filtered and amplified through the SURFACE board. This board is specially designed for the requirements of the RNO-G detector. To reduce background noise from Galactic radio background radiation frequencies below 80 MHz are suppressed (see Fig. 25 left). To account for the LTE data transfer at 880 MHz, frequencies above 700 MHz are also suppressed. The highest amplification of  $\sim 60$  dB is between 100 MHz and 400 MHz. This is in order to optimize the detector not only for cosmic rays but also to reconstruct the direction and energy from a possible neutrino and determine the viewing angle according to the Cherenkov cone. Fig. 25 right shows the measured group delay for the SURFACE board. In the frequency band from 80 MHz to 200 MHz it has a group delay of approximately 15 ns. This leads again to a higher dispersion in the pulse. Between 200 MHz and 600 MHz the group delay is constant.

The LPDA and SURFACE board together yield the impulse response of the system. This is the combination of VEL determined by the LPDA and amplification determined by the SURFACE board. The impulse response is shown in Fig. 26. Frequencies lower



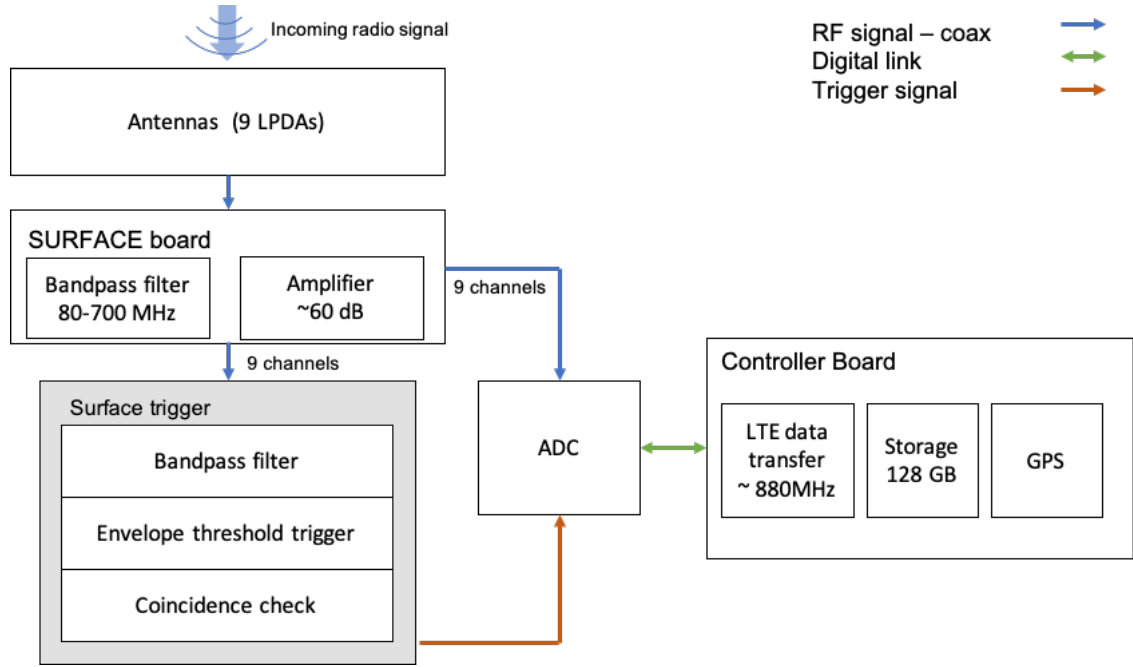


Figure 24: Schematic visualization of the signal chain for the surface component of one station. After the electric field is registered by the antennas, the signal is processed by the SURFACE board with bandpass filter and amplifier. The signal is then split into a trigger signal and a signal going directly to the analog to digital converter (ADC). A digital link sends the ADC output to the controller board.

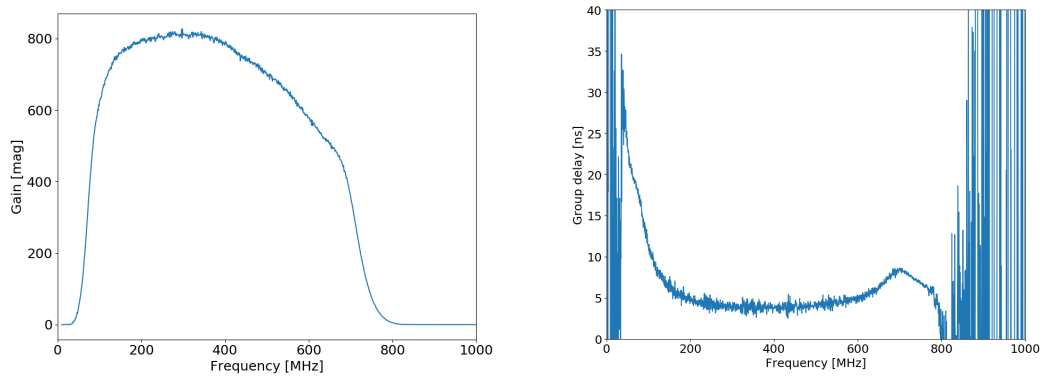


Figure 25: Measurements of the SURFACE board from [35]. Left: Gain. Right: Group delay.

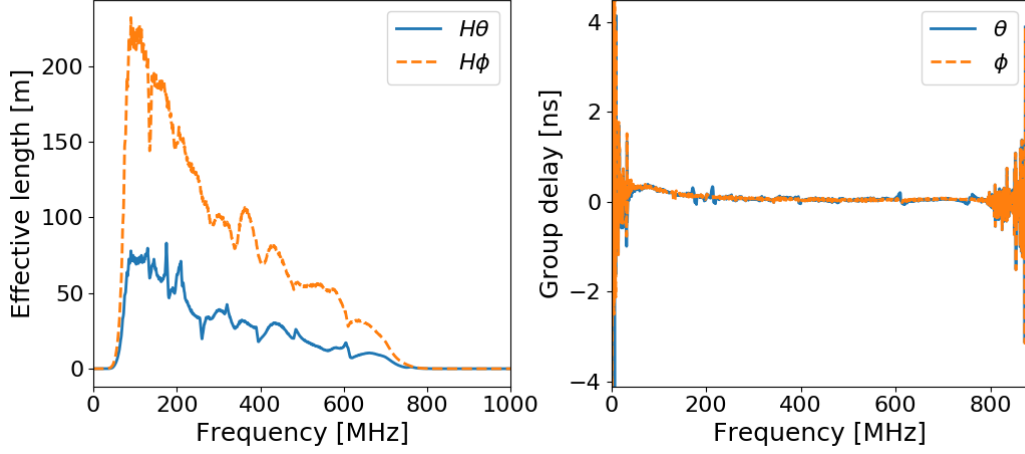


Figure 26: Impulse response, which is the combination of VEL of the LPDA and the amplification from the SURFACE board. The impulse response is simulated for the electric field shown in Fig. 20. The signal arrives at  $\theta_{\text{ant}} = 55^\circ$  and  $\phi_{\text{ant}} = 0^\circ$  with respect to the antenna. Left: Effective length. Right: Group delay.

than 80 MHz and above 750 MHz are strongly suppressed. Towards higher frequencies, the effective length flattens more slowly, which matches with the amplification from the SURFACE board for frequencies between 100 MHz and 400 MHz.

The observed voltage over time and frequency is depicted in Fig. 27. Due to the group delay of the SURFACE board, the dispersion has increased. The highest amplification is by a factor of  $\sim 60$  dB in the range of 200 MHz. With the understanding of the combination of LPDA and amplifying SURFACE board on the incoming signals, the characteristics and requirements of the trigger can be discussed.

### 3.2 Envelope trigger

This section describes the implementation of the trace envelope and the trigger band-pass filter and introduces the concept of a coincidence check. The discussion of their dependencies is part of section 3.3.

The quantity which is most relevant for the air shower detection are the traces of the LPDAs that point upwards. An example of this channel trace is shown in Fig. 28. The traces measure different voltages. This is due to their orientation with respect to the signal. The time shift is due their location within the station. The selected parameters for the trigger are the threshold of the voltage, the frequency band, and the coincidence

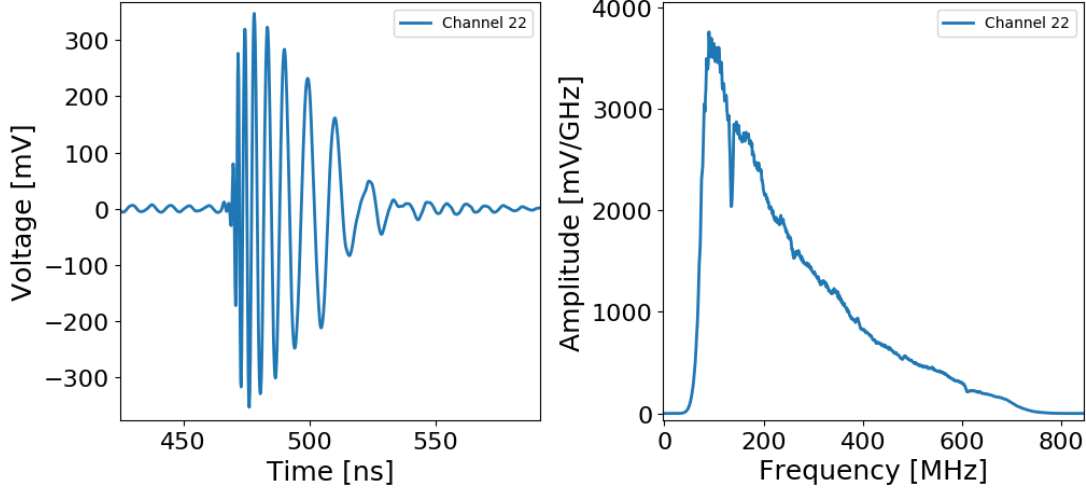


Figure 27: Simulated induced antenna voltage for the electric field shown in Fig. 20. The signal arrives at  $\theta_{\text{ant}} = 55^\circ$  and  $\phi_{\text{ant}} = 0^\circ$  with respect to the antenna. The shown signal is with amplification from the SURFACE board. Left: timed domain. Right: Frequency domain.

of a certain number of channels that exceed the trigger threshold within a given time interval.

The threshold for the trigger will be tested on the signal envelope, which is driven by the hardware design. The implementation of an envelope in hardware is done with fast Schottky diodes. They are easy to install and have the advantage of low power consumption, which is necessary because the energy supply for a station is limited by two solar panels. The trace envelope is generally less sensitive to small fluctuations of noise than the trace itself. In this study, an envelope is used calculated with the Hilbert-Method as suggested in [16]. The Hilbert transformation is described in [28] with:

$$H\{f\} = \frac{1}{\pi} \int_{-\infty}^{\infty} \frac{f(x')dx'}{x' - x} = \frac{-1}{\pi x} * f(x) \quad (10)$$

The imaginary part  $s_{\text{I}}(t)$  of the simulated data  $s_{\text{R}}(t)$  can be identified as the Hilbert transform  $s_{\text{I}}(t) = H\{s_{\text{R}}(t)\}$ . The Fourier transform of  $(-\pi x)^{-1}$  is  $i \cdot \text{sgn}(a)$  which leads to the consequence that the amplitude of the spectral components are left unchanged, but their phases are altered by  $+\pi/2$  for negative frequency components and  $-\pi/2$  for positive ones. The multiplication with  $i$  restores the positive frequency components, while shifting the negative ones by additional  $+\pi/2$ , which results in their negation. The envelope  $s_{\text{env}}(t)$  can then be calculated with:

$$s_{\text{env}}(t) = \sqrt{(s_{\text{R}}(t))^2 \cdot (H\{s_{\text{R}}(t)\})^2} = \sqrt{(s_{\text{R}}(t))^2 \cdot (s_{\text{I}}(t))^2} \quad (11)$$

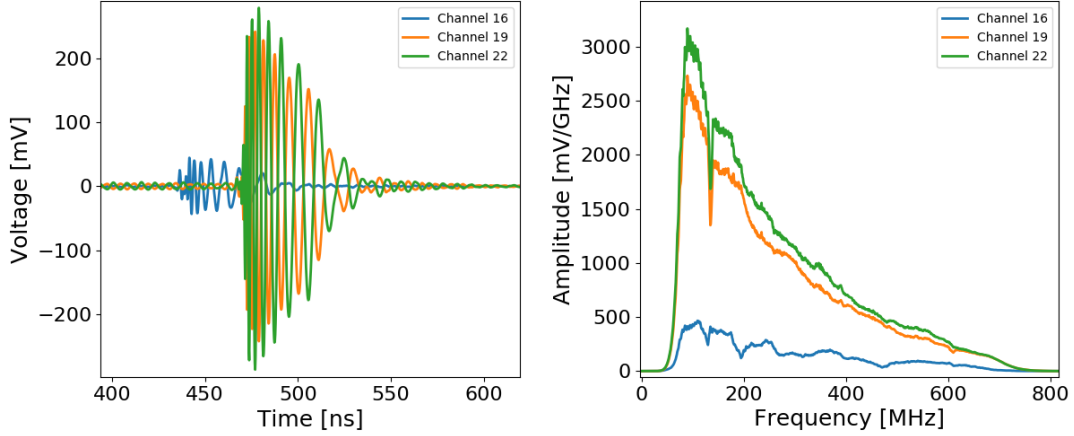


Figure 28: Channel traces of three LPDAs that point upwards (channel 16, 19, 22), filtered and amplified by the SURFACE board. Each color belongs to one channel. On the left-hand side the pulse is shown in the time domain while on the right-hand side the corresponding frequency spectrum is depicted.

In Fig. 29 the Hilbert envelope covering a pulse stemming from an air shower is shown.

The trigger set-up for the surface antennas contains its own bandpass filter. As visible in Fig. 24, the trigger set-up is separated from the main signal chain. As a consequence, the smaller bandpass is not applied to the original signal. With an additional bandpass filter the background noise can be reduced and the threshold can be lowered. This is due to the fact, that frequencies between 80 MHz to 500 MHz contribute almost equally to the total noise. The signal has the highest contribution from lower frequencies around 100 MHz. Afterwards the amplitude of the frequencies drops. Fig. 30 top shows a comparison between noise modified by the SURFACE board and noise modified by the SURFACE board and an additional filter in the trigger module. In Fig. 30 bottom the same hardware path is shown for a signal from a cosmic ray induced air shower. The differences in the frequency spectrum of signal and noise are clearly visible. In Fig. 31 a comparison of signal and signal and noise is shown. The combination of signal and noise is the quantity which is measured. If a bandpass filter is applied, the signal to noise ratio (SNR) is improved. On the top left, the signal has the same voltage as the trace including signal and noise. On the top right, the trace is filtered. The signal is clearly visible in the signal and noise trace. Therefore, a bandpass filter for the lower frequencies improves the signal to noise ration and lowers the trigger threshold.

Each of the nine channels is evaluated separately for the envelope trigger. With three

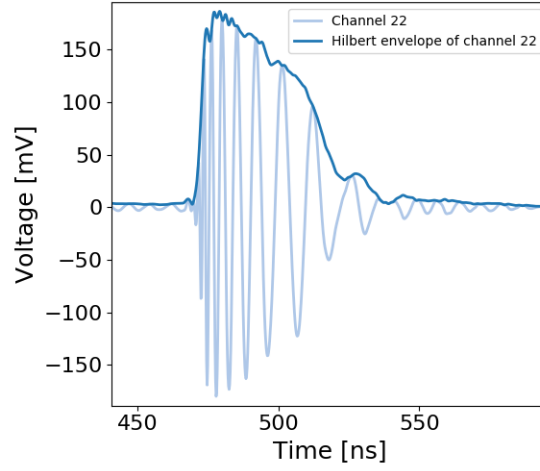


Figure 29: Channel trace in the time domain with amplification of the SURFACE board. The dark blue line represents the signal Hilbert envelope.

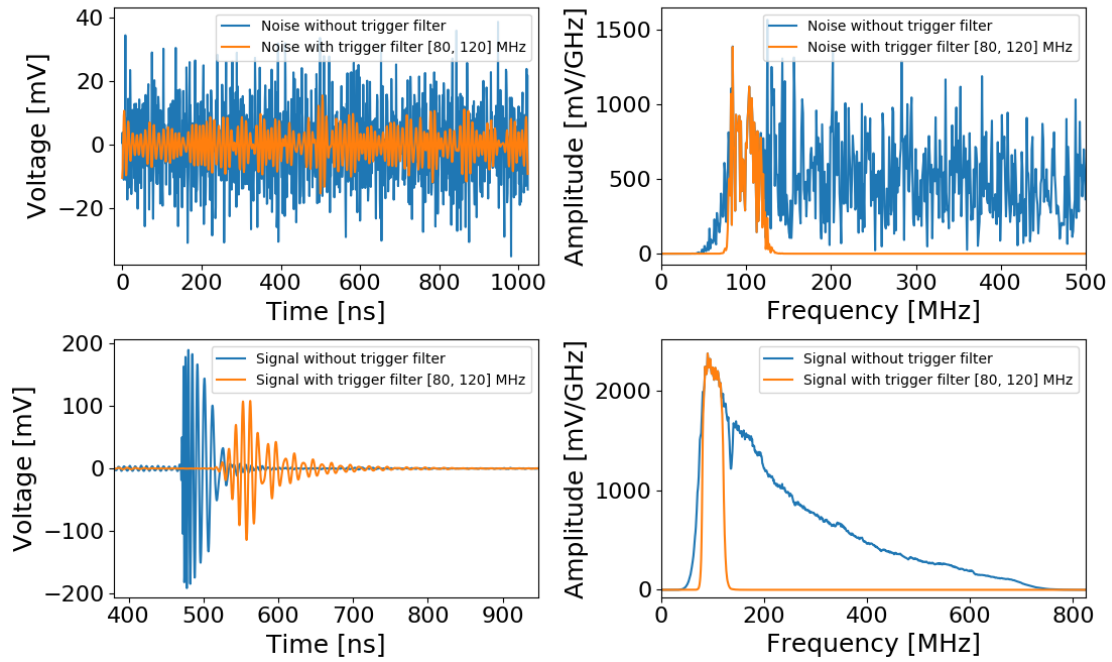


Figure 30: Comparison of thermal and galactic noise (top) and an air shower signal with a CR energy of  $10^{18}$  eV (bottom) both simulated with LPDAs and SURFACE board. The blue line is unmodified while the orange lines includes a bandpass filter in the trigger module of 80 MHz to 120 MHz. The left figures show the voltage while the figure at the right represents the frequency spectrum.

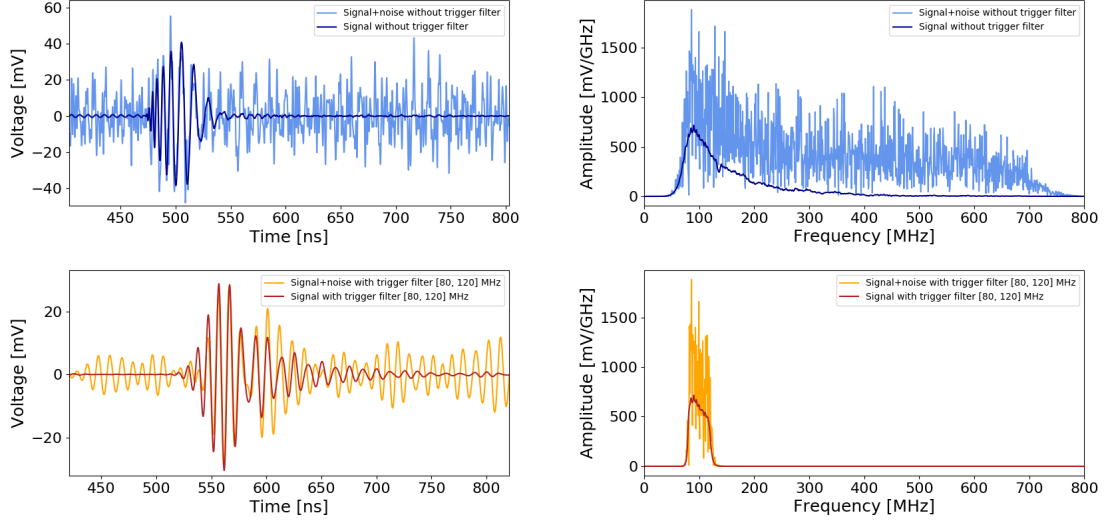


Figure 31: Comparison of a trace including thermal and galactic noise and an air shower signal with a CR energy of  $10^{18}$  eV (faded colors) with the air shower signal. The left figures show the voltage while the figures at the right represent the frequency spectrum. Top: Without filter. Bottom: With bandpass filter in the trigger module of 80 MHz to 120 MHz.

antennas that point upwards it is expected that more than one antenna exceeds the threshold in case of an air shower event. Therefore, a coincidence window is determined in which a certain number of antennas is required to pass the threshold (see Fig. 32). The background noise is expected not to be correlated. Therefore a coincidence check reduces the noise trigger rate.

### 3.3 Triggering strategy

This section investigates the dependencies of the different trigger parameters and proposes a strategy to optimize the trigger settings. An overview of the trigger parameters and their behavior is given in Tab. 4.

The optimization of the trigger parameters is a multidimensional problem. Ideally, all air showers should trigger. Because the signal amplitude scales linearly with shower energy, the trigger threshold should be as low as possible to detect even shower with a small energy. A smaller threshold however, leads to a higher data rate because the noise passes the threshold more often. The in-ice component has the phased array as trigger and yields a trigger rate of 1 Hz. In order to keep the data rate low, the parameters of the

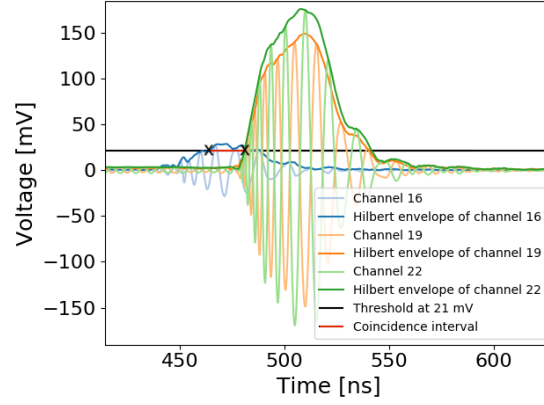


Figure 32: Channel traces of three LPDAs which point upwards, simulated with SURFACE board. The black line indicates the threshold. The crosses mark the points in time where the two signal envelopes exceed the threshold. The red line between the two crosses is the coincidence interval. All channels pass the threshold.

	Threshold	Frequency band	Coincidence window	Number coincidence
<b>too big</b>	Cosmic ray events of low energies will be missed	additional noise; requires higher threshold to keep the trigger rate low	random coincidences	missed events
<b>too small</b>	random triggers; trigger rate too high	missed events	missed events	random coincidences

Table 4: General trigger parameters and their behavior. The parameters are not independent of each other.

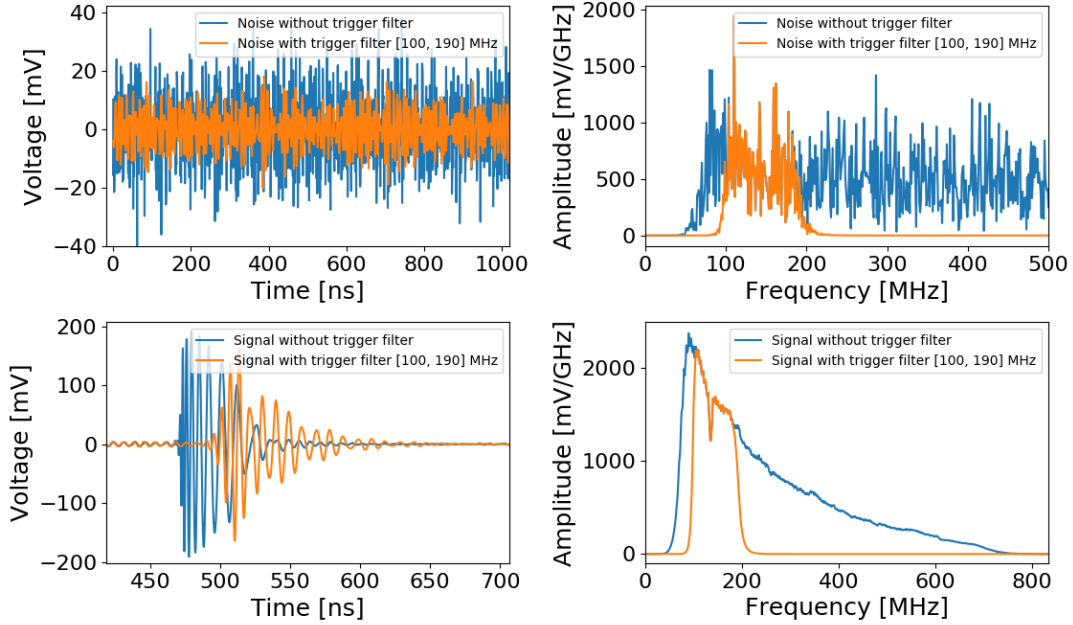


Figure 33: Comparison of the expected thermal noise (340 K) and galactic noise (left) and an air shower signal with a CR energy of  $3.16 \times 10^{18}$  eV (right) both simulated with LPDAs and SURFACE board. The blue line is unmodified while the orange lines includes a bandpass filter in the trigger settings of 100 MHz to 190 MHz. The top figures show the voltage while the figure at the bottom represents the frequency spectrum.

surface trigger are adjusted to match a noise trigger rate  $< 0.5$  Hz. The expected noise is the sum of thermal noise of  $T = 340$  K and galactic background emission.

The threshold for a noise trigger rate  $< 0.5$  Hz can be simulated using CoREAS files and the NuRadioReco software. The challenging point in this calculation is that the amplitude of the trace changes with different passbands, as seen in Fig. 33 right. A broad frequency band will introduce additional noise (see Fig. 33 left) while a narrow band will lead to missed events, because in narrowing the bound, the maximum voltage level is also reduced. Due to the amplifier used, the noise varies within the frequency range. This variation makes it necessary to test different bandwidth and limits of the bandpass. This becomes clear with the comparison of a 40 MHz passband starting at 80 MHz versus starting at 120 MHz in Fig. 34. Both simulations are done with a passband of 40 MHz width, but the maximal voltage of the trace differs.

To determine the optimal parameter for the threshold and frequency band the threshold for a noise trigger rate  $< 0.5$  Hz will be simulated for various frequency bands. The



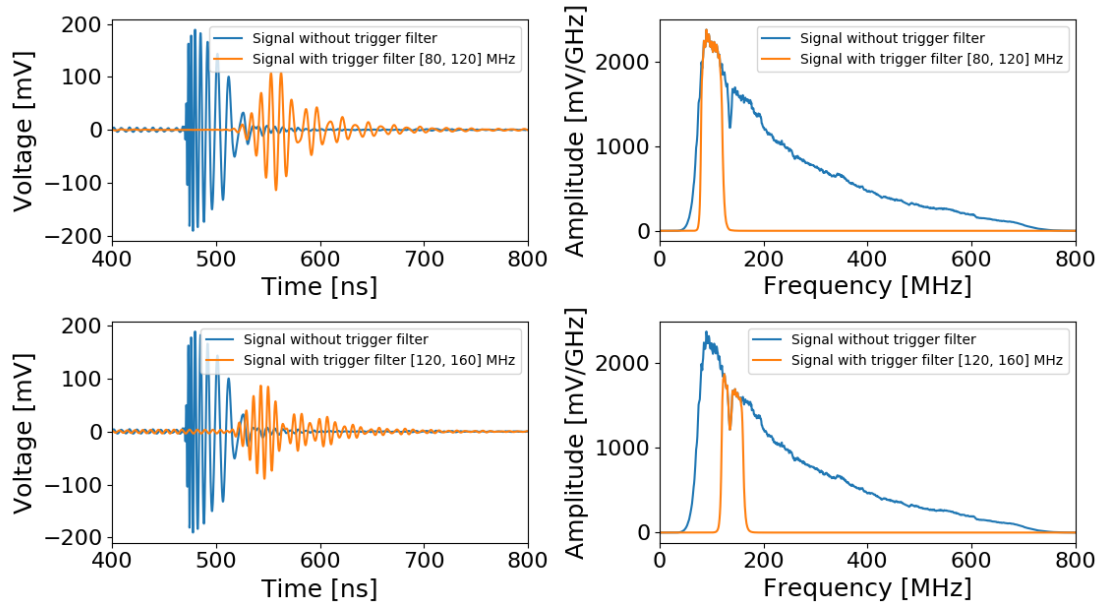


Figure 34: Simulations of an air shower signal with a CR energy of  $3.16 \times 10^{18}$  eV with LPDA and SURFACE board for a passband of 40 MHz width at different frequencies. The blue line is unmodified while the orange lines includes a bandpass filter in the trigger settings. The left figures show the voltage while the figures at the right represents the frequency spectrum of the signal. Top: Bandpass of 80 MHz to 120 MHz. Bottom: Bandpass of 120 MHz to 160 MHz.

lower limit starts at 80 MHz and goes up to 150 MHz in 10 MHz steps. The upper limit is tested starting from a bandwidth of 30 MHz and increasing in 10 MHz steps up to 400 MHz. The obtained thresholds and corresponding frequency bands are then applied to air shower signals. The results of the different settings can then be compared. The most efficient combination will also depend on the expected properties of air shower in Greenland. Once the detector is deployed, the threshold can still be changed, but the passband cannot. Therefore this parameter is especially delicate.

After the threshold and passband are determined, different coincidence windows and the required number of antennas can be tested. Since the velocity of electromagnetic waves is well understood and the number of antennas is limited, this part of the optimization is less complex.

The coincidence check is based on a time interval as described in 3.2. If this time window is too small events will be missed because the signal needs time to pass the distance between two or more antennas. A long time interval will lead to random coincidences and increases the noise trigger rate.

If the number of channels which are required to exceed the threshold in the given time interval, is too high there will be missed events. Differences in antenna orientation and footprint properties make it so that not every antenna will register an air shower signal. If only a small number of antennas is required to pass the threshold, random coincidences occur more often.

## 4 Monte Carlo simulations

To simulate particle showers and the radio signal created by them a Monte Carlo approach is used. The method is based on stochastic processes, which rely on the interaction cross-section of single particles. With the numeric results, different parameters can be tested, e.g. for the detector layout and the parameters set in the hardware. In the following, the simulated air shower set and the procedure is described. Afterwards different parameters for the envelope trigger are investigated.

### 4.1 Air shower set and procedure

For the surface detector, only air shower simulations are necessary. A total of 407 air showers assuming protons as primary particle were produced using CORSIKA 7.6400 [44] with QGSJetII.04 [59] and UrQMD [27] as hadronic interaction models. The radio emission is generated by the CoREAS plug-in [48].

CORSIKA is a program for detailed simulation of extensive air showers initiated by high energy cosmic ray particles. Different primaries such as protons and iron atoms are taken into account. The particles are tracked through the atmosphere until they undergo reactions with the air nuclei or decay. In particle decays all decay branches down to the 1% level are taken into account.

To simulate the radio emission created by the air showers, an extension called CoREAS is used. It implements the endpoint formalism for the calculation of electromagnetic radiation directly in CORSIKA. The endpoint formalism is based on the fact that: "all radiation from particle acceleration can be described as superpositions of instantaneous accelerations (endpoints)" [50]. The electric field contribution can be either derived in the frequency domain:

$$\vec{E}_{\pm}(\vec{x}, \nu) = \pm \frac{q}{c} \frac{e^{ikR(t'_0)}}{R(t'_0)} \frac{e^{2\pi i \nu t'_0}}{1 - n\vec{\beta}^* \cdot \hat{r}} \hat{r} \times [\hat{r} \times \vec{\beta}^*] \quad (12)$$

or in the time domain:

$$\vec{E}_{\pm}(\vec{x}, t) = \pm \frac{1}{\Delta t} \frac{q}{c} \left( \frac{\hat{r} \times [\hat{r} \times \vec{\beta}^*]}{(1 - n\vec{\beta}^* \cdot \hat{r})R} \right) \quad (13)$$

These equations describe the electric field  $\vec{E}$  for an acceleration at time  $t = t_0$  to a velocity  $\vec{\beta} = \frac{\vec{v}}{c} = \vec{\beta}^*$ . The indices  $\pm$  indicates an acceleration from rest (positive), or an

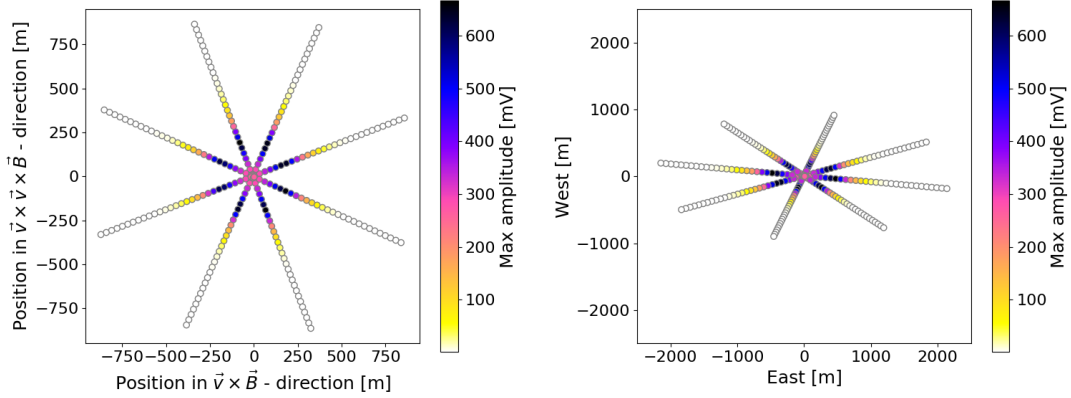


Figure 35: Grid of 240 antenna positions on which the air shower was simulated. Left: Observer positions in shower plane. The direction of the shower axis is  $\vec{v}$ , the direction of the magnetic field  $\vec{B}$ . Right: Positions of the observers projected onto ground. The electric field of the CoREAS simulations is combined with the impulse response of a RNO-G station. The color code shows the maximal amplitude measured by an upward facing channel of the station. The simulated air shower arrived under a zenith angle  $\theta = 65^\circ$  with a shower energy of  $3.16 \times 10^{18}$  eV.

acceleration to rest (negative). The charge of the particle (in CGS units) is  $q$ ,  $R$  is the distance from the point of emission to the observer,  $\hat{r}$  is a unit vector in the direction of the observer, and  $n$  is the refractive index of the medium. The relation between wavenumber  $k$  and the frequency  $\nu$  is  $k = 2\pi\nu n/c$  (see [50]).

To simulate the radio emission, the particle trajectories are dissected into a large enough number of these endpoints. The numerical calculations can be conducted in either of the two domains. For air shower simulations, both domains are desired. Therefore in order to convert one into the other using a fast-Fourier transformations, an adequate step size has to be chosen in the simulation. With this approach, no assumptions on the emission mechanism were made and the complete electron and positron distributions as simulated by CORSIKA can be taken into account. The electron and positron distribution can be thinned to reduce calculation time.

The simulations are performed on a star-shaped grid of 240 stations, as shown in Fig. 35. The grid is aligned to the shower plane, spanned by the  $\vec{v} \times \vec{B}$  - axis and the  $\vec{v} \times \vec{v} \times \vec{B}$  - axis, where  $\vec{v}$  is the direction of the shower and  $\vec{B}$  the direction of the magnetic field. Afterwards the station positions are projected to the ground, according to its arrival direction. The CoREAS simulations deliver the resulting electric field per

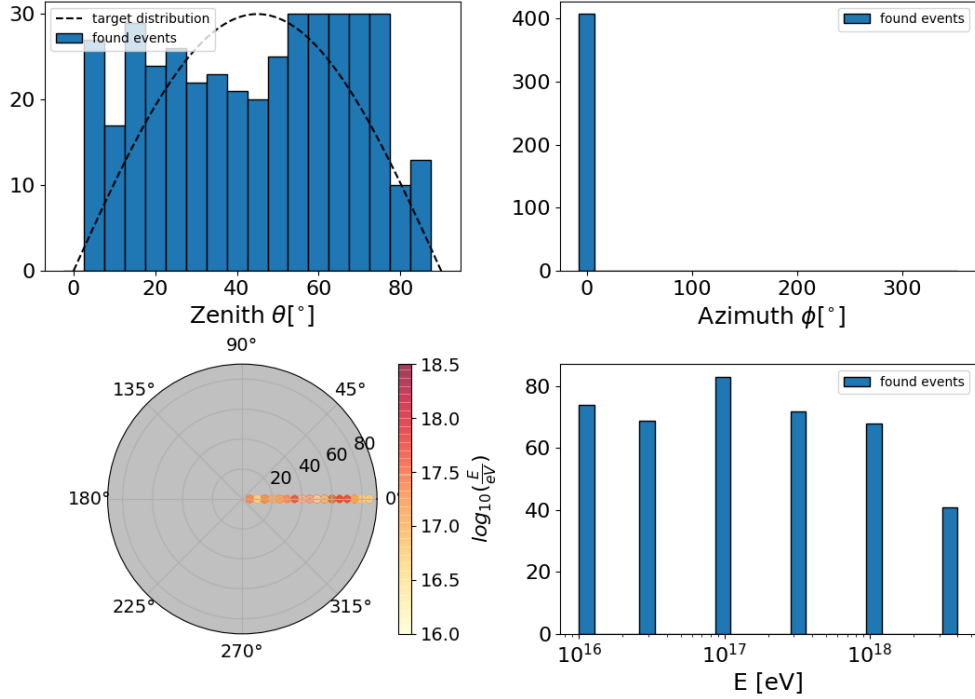


Figure 36: Parameter distribution of the 407 simulated air showers used. Because the magnetic field at Summit Station is almost perpendicular to the ground (inclination  $81.12^\circ$  downwards), the influence of the azimuth angle is ignored for this study. For detailed numbers see Tab. 5. The target distribution for the zenith angle considers the solid angle due to isotropy and the projected area of the detector.

antenna position as a function of time. To obtain the amplitude of each channel, the electric field is folded with the antenna response and the amplifier as described in Sec. 3.1.

The distributions of all shower parameters of the 407 showers are shown in Fig. 36. The simulated showers span an energy range from  $1 \times 10^{16}$  eV to  $3.16 \times 10^{18}$  eV and cover a zenith angle  $\theta$  from  $5^\circ$  to  $85^\circ$ , where  $0^\circ$  are vertical showers. The magnetic field at summit station (declination  $26.06^\circ$ W, inclination  $81.12^\circ$  downwards) is almost perpendicular to the surface and the plane of the azimuth angle  $\phi$ . Therefore, the influence of the azimuth direction  $\phi$  is ignored for this study. The number of air showers for three energy intervals and nine zenith intervals are shown in Tab. 5.

In order to evaluate the trigger parameters, the trigger performance is expressed in terms of the effective area for one station. This has the advantage that no limit is set on the distance between air shower core and detector station.

Due to the star shape of the station grid, the area around one station near the star

Shower energy	0° – 10°	10° – 20°	20° – 30°	30° – 40°	40° – 50°	50° – 60°	60° – 70°	70° – 80°	80° – 90°	Sum
$1 \times 10^{16} \text{ eV} - 3.2 \times 10^{16} \text{ eV}$	10	18	20	17	12	16	20	20	10	143
$1 \times 10^{17} \text{ eV} - 3.2 \times 10^{17} \text{ eV}$	9	16	19	19	20	20	20	20	12	155
$1 \times 10^{18} \text{ eV} - 3.2 \times 10^{18} \text{ eV}$	8	12	11	9	9	19	20	20	1	109
Sum	27	46	50	45	41	55	60	60	23	407

Table 5: Number of showers in each shower energy interval and zenith interval. In total, 407 showers were simulated. There are 109 air shower with energies larger  $10^{18}$  eV, 31 of them arrive under a zenith angle smaller than  $30^\circ$ .

center is much smaller than the area of a station further away, therefore the area a specific station covers has to be known. The calculations are done using a Voronoi diagram [77, 22]. The Voronoi diagram is the nearest-neighbor map for a set of points. This means, that for each station in the star, there is corresponding region consisting of all points of the plane closer to that station than to any other. The Voronoi cell around a station can be identified as the area the station covers. The vertices of the cell around each station are calculated in the shower plane (see Fig. 37 right). The vertices are then transformed to the ground, and the area of each cell is calculated. The last station of each arm has no limitation and is not expected to trigger, therefore their area is set to zero. In order to calculate the effective area of a shower for one station, the areas of the cells in which one station triggered are summed up.

The area on ground of a showers varies with zenith angle (see Fig. 19). With increasing shower energy, a larger area of the footprint is visible to the detector. To determine the effective area over multiple showers, the calculations have to be done for each energy interval and zenith angle separately.

In a next step, the projected area of the detector has to be taken into account. It can be obtained for a certain zenith interval with the limits  $\theta_1, \theta_2$  by using

$$A_{\text{eff}}^{\text{proj}}(\theta) = A_{\text{eff}}(\theta) \cdot \frac{\cos(\theta_1) + \cos(\theta_2)}{2} \quad (14)$$

The projected effective area for shower arriving from above ( $\theta = 0^\circ$ ) is the same as the effective area. If a cosmic ray arrives at  $\theta = 90^\circ$ , the projected effective area is zero. This matches the expectation, that no events from the horizon reach the flat surface of the detector.

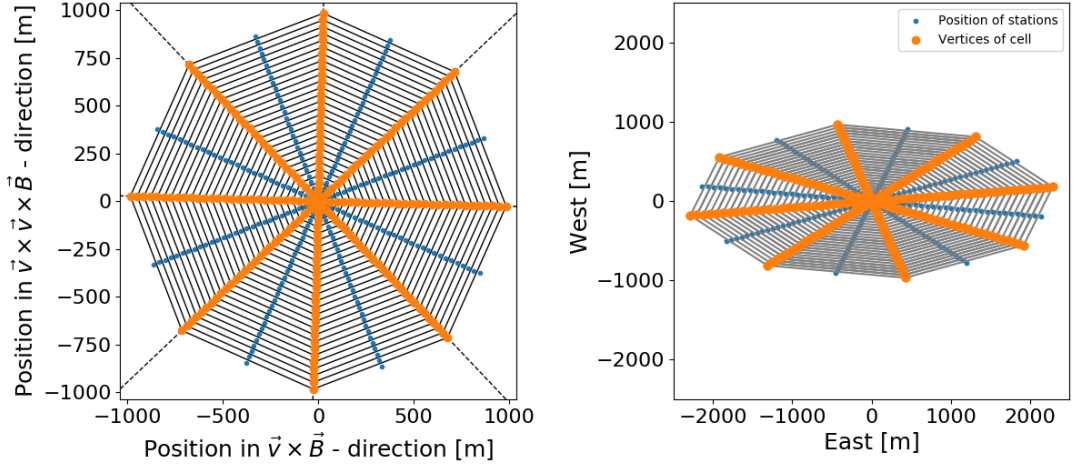


Figure 37: Illustration of the Voronoi diagram used to calculate the area each station has to cover. The blue points are the station positions, the orange points the vertices of the cell around one station. The vertices are first calculated in the shower plane (left) and then projected on ground (right). The area of the cell is calculated on ground. The simulated air shower arrived under a zenith angle  $\theta = 65^\circ$ .

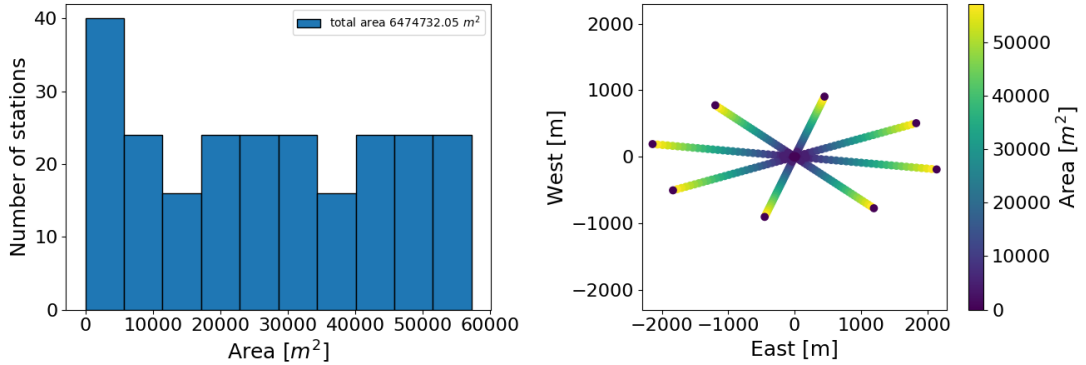


Figure 38: Illustration of the calculated area as shown in Fig. 37. The simulated air shower arrived under a zenith angle  $\theta = 65^\circ$ . The area of the last station of each arm is set to zero. The number of stations in the first area bin is high, because many stations are located in the center of the star, where the corresponding area is small.

## 4.2 Noise

For the simulations, two sources of noise are taken into account: thermal noise from the system and galactic background emission.

The *thermal noise* is expressed as a temperature. Preliminary measurements from the noise temperature of the IGLU board are shown in Fig. 40. They indicate only little increase towards higher frequencies. Therefore the thermal noise is assumed to be constant within frequency. The noise root mean square of the thermal noise  $V_{\text{rms}}^{\text{thermal}}$  is calculated according to:

$$V_{\text{rms}}^{\text{thermal}} = \sqrt{k_B \cdot \Delta f \cdot T_{\text{eff}} \cdot R} \quad (15)$$

where  $\Delta f$  is the bandwidth of the thermal noise,  $R$  is a resistance and  $T_{\text{eff}}$  the effective temperature. Since the thermal noise is expected to be uniform around the antenna, no antenna response is taken into account when calculating the pure thermal noise. As a rough estimation, the noise is applied in a band from 50 MHz to 800 MHz, yielding a  $\Delta f = 750$  MHz, because this band corresponds to the antenna. With a resistance  $R = 50 \Omega$ , and  $T_{\text{eff}} = 340$  K, the  $V_{\text{rms}}^{\text{thermal}} = 13.27 \mu\text{V}$ . The frequency spectrum follows a Rayleigh distribution. In Fig. 39 the traces and the frequency spectrum for all LPDAs are shown.

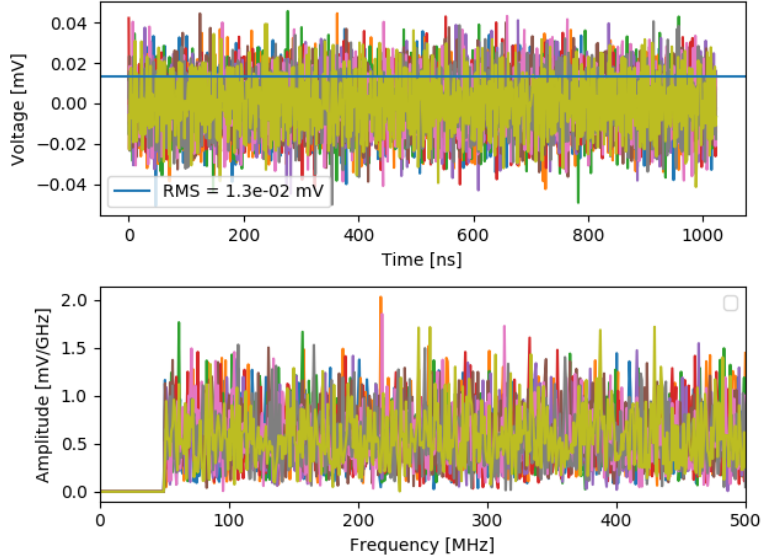


Figure 39: Thermal noise of 340 K, shown for all nine channels without amplification. The blue line indicates the root mean square over all traces, which agrees with the calculation from temperature. Top: Time domain. Bottom: Frequency domain.



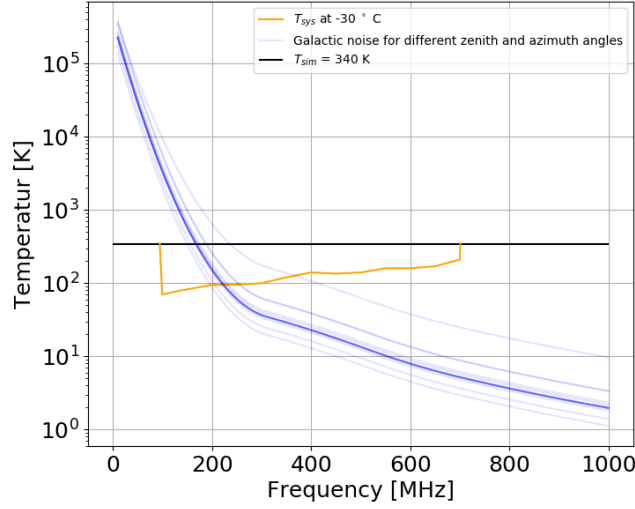


Figure 40: Noise temperature as a function of frequency. The different blue lines indicate the galactic noise temperature, which are retrieved from the GSM model for different zenith and azimuth angles. The orange line shows the preliminary measurements of the noise temperature of the amplifier. The black line indicates the thermal noise temperature of 340 K, which was used for the simulations.

As model of *diffuse galactic radio emission* the Galactic Sky Model (GSM) by [58, 60] is used. It predicts the all-sky temperature at any frequency between 10 MHz and 100 GHz. It interpolates over eleven data sets (at 10, 22, 45 and 408 MHz and 1.42, 2.326, 23, 33, 41, 61, 94 GHz). The predicted sky maps have an angular resolution of  $5.1^\circ$ . The model is reported to be accurate between 1% and 10% on a relative scale (i.e. not accounting for errors in reference maps). The model was later improved by [79].

From the GSM the sky temperature for the antenna field of view was calculated. The visible patch of sky depends on the time of the day. In Fig. 41, the radio sky at 110 MHz is shown. The left image is in galactic coordinates, the galactic disk is visible as well as two bright radio sources to the left (Cassiopeia A and Cygnus Loop) [37]. They are also visible over Greenland, as the image on the right-hand side shows.

With variation in the visible part of the sky, the galactic noise changes. In Fig. 42, the variation within the galactic noise are shown over one day. Since the galactic center is not visible at any time, the variations are small. Therefore, the noise was calculated for one point in time only.

The output of the GSM Map can be translated to a spectral radiance  $B$  per solid angle as a function with  $\delta$  being the declination and  $\alpha$  describing right ascension. For

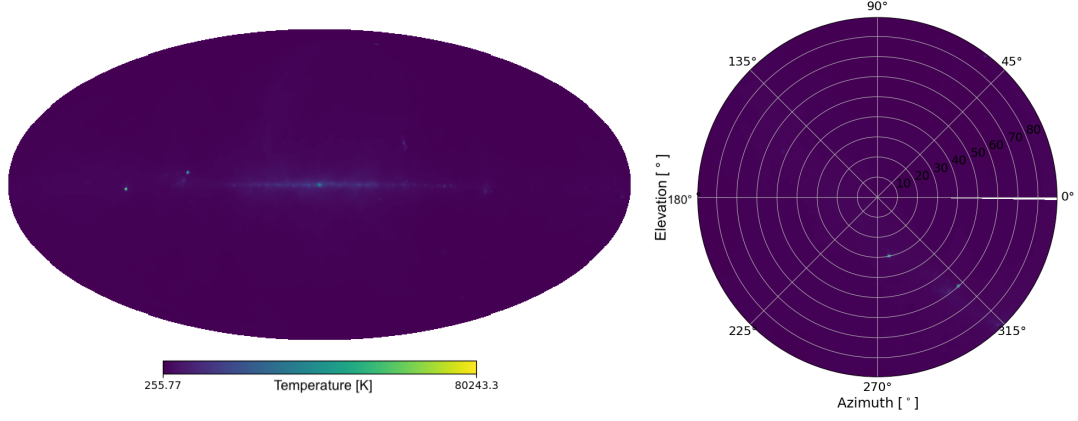


Figure 41: Radio sky from GSM map at 110 MHz. Left: Galactic coordinates. Right: Field of view for the location of RNO-G at summit station (latitude 72.58° N, longitude 38.48° W). The date is 2019/01/01 at 00:00.

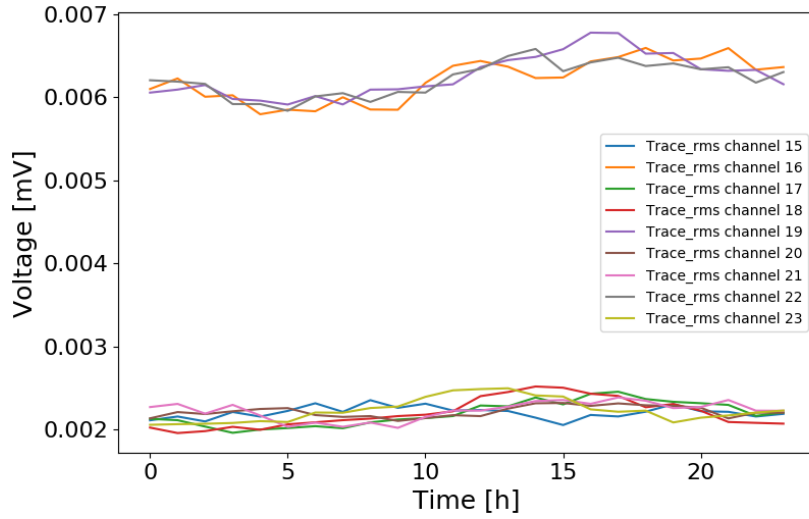


Figure 42: Variation of the galactic noise over one day, simulated for antennas at the location of RNO-G. The date is 2019/01/01.

low frequencies, the Rayleigh-Jeans law approximates the spectral radiance at a given temperature  $T$  [66]. The spectral radiance is

$$B(\alpha, \delta, \nu) = \frac{2k_B}{c^2} \nu^2 T(\alpha, \delta, \nu) \quad (16)$$

where  $k_B$  is the Boltzmann constant and  $c$  the speed of light, which leads to the unit of  $[B] = \text{W m}^{-2} \text{Hz}^{-1} \text{sr}^{-1}$ . The received spectral power density  $S_\nu$  at some frequency  $\nu$  is then

$$S_\nu = \frac{2k_B}{c^2} \nu^2 T(\alpha, \delta, \nu) d\Omega. \quad (17)$$

with  $d\Omega$  being the solid angle of a patch of the sky.

For a monochromatic plane wave, the electric field is connected to the spectral power density with:

$$E_\nu = \sqrt{\frac{S_\nu(\theta, \phi, \nu)}{c \cdot \epsilon_0}} \quad (18)$$

with  $c$  being the speed of light and  $\epsilon_0$  being the vacuum permittivity. The total electric field is the sum over all frequencies.

$$E_{\text{total}} = \int E_\nu d\nu \quad (19)$$

The results is shown in Fig. 43. The galactic noise changes with the frequency and is significantly higher for upward-facing channels. The highest contribution is from frequencies around 80 MHz.

The total noise for each channel is the sum of thermal and galactic noise, together with the amplification in the SURFACE board. The results for one upwardfacing channel are shown in Fig. 44. The galactic noise is dominante up to 110 MHz, for higher frequencies the contribution from the galactic noise decreases and the thermal component is dominant. The frequency spectrum of an air shower signal (see Fig. 27) shows as maximum at 80 MHz, which is the same frequency were the galactic noise dominates. Therefore the trigger passband has to be determined carefully.

### 4.3 Threshold and frequency band

As pointed out in Sec. 3.3, determining the optimal parameters of the trigger is a multidimensional problem. The limiting factor for the threshold is the 1 Hz noise trigger rate the hardware is able to store, because of a limited communication bandwidth. The

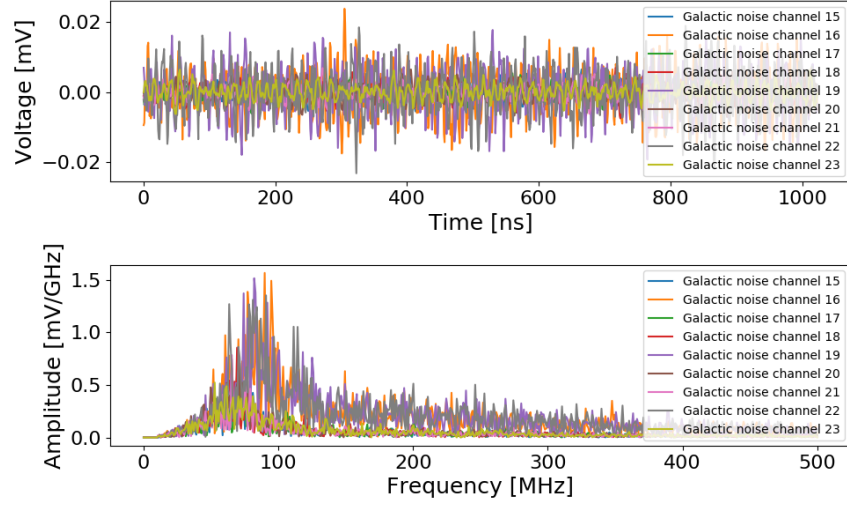


Figure 43: Galactic noise for all nine LPDAs. Channel 16, 19 and 22 are orientated upwards to the sky, while the other channels are faced diagonally downwards. Therefore the galactic noise is higher at the upward channels. Top: time domain. Bottom: Frequency domain.

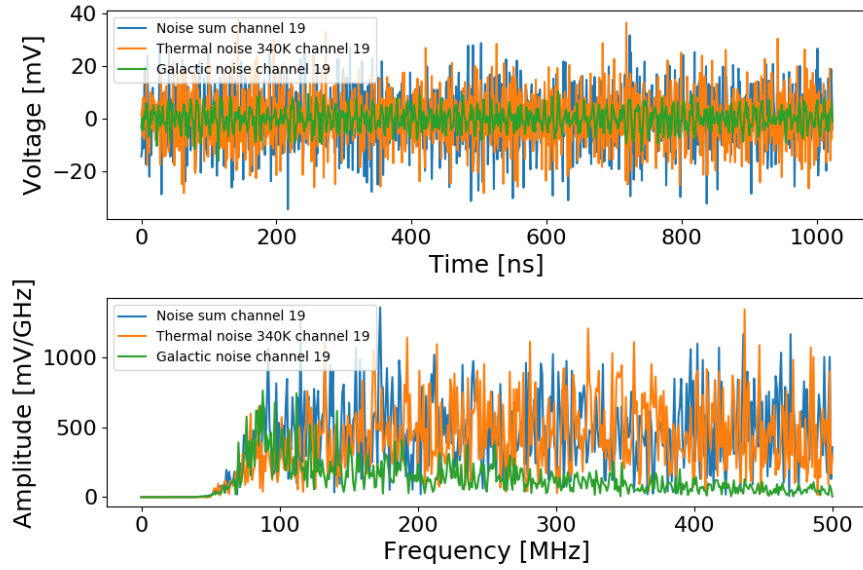


Figure 44: Thermal noise (orange), galactic noise (green) and their sum (blue) for one upward facing channel with amplification. The galactic noise dominates until  $\sim 130$  MHz, from thereon, the thermal noise is dominant. Top: time domain. Bottom: Frequency domain.

data comes from both triggers, the phased array in the ice and the envelope trigger at the surface. The phased array trigger already has a trigger rate of 1 Hz. Therefore, the surface trigger rate should be significantly smaller (around 0.1 Hz).

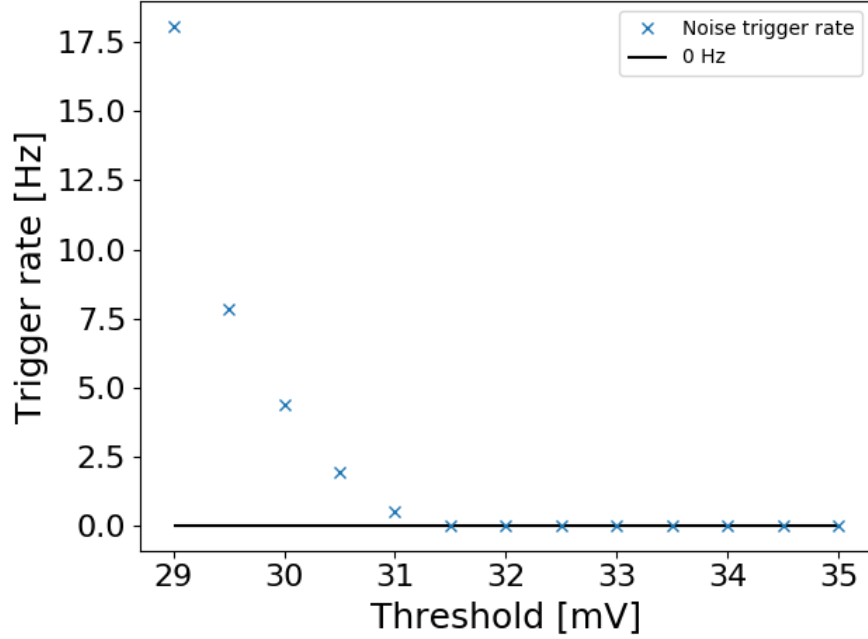


Figure 45: Trigger rate in Hz as a function of trigger threshold for a passband from 80 MHz to 180 MHz. The black line indicated a noise trigger rate of 0 Hz.

Different passbands between 80 MHz and 400 MHz are tested on the noise described previously. The smallest bandwidth is 30 MHz. Each trace is 1024 ns long and has a sampling rate of 1 GHz. This means, that the trigger checks every 1023 ns if the trigger criteria are fulfilled. To obtain a resolution of 0.5 Hz for the noise trigger rate, the trigger needs to test on  $2 \times 10^6$  traces. Therefore the noise trigger rate is chosen to be  $< 0.5$  Hz. The final threshold is selected by testing different thresholds on their corresponding noise trigger rate. Once the noise trigger rate falls below 0.5 Hz, the threshold is determined. An example for the slope of the noise trigger rate in the passband from 80 MHz to 180 MHz is shown in Fig. 45. The final threshold of the passband is the threshold, where the noise trigger rate turns zero for the first time, here 32.5 mV.

The threshold for each passband tested is shown in Fig. 46. The threshold increases with higher bandwidths. The iso-voltage lines follow roughly the passbands with the same bandwidths. The 30 MHz bandwidths seems to have a lower threshold when choosing a higher lower cutoff frequency. The 25 mV voltage line has also a little step when changing the lower cutoff frequency from 90 MHz to 100 MHz. This matches the expectation, since at lower frequency the galactic noise has a higher contribution, while the thermal noise

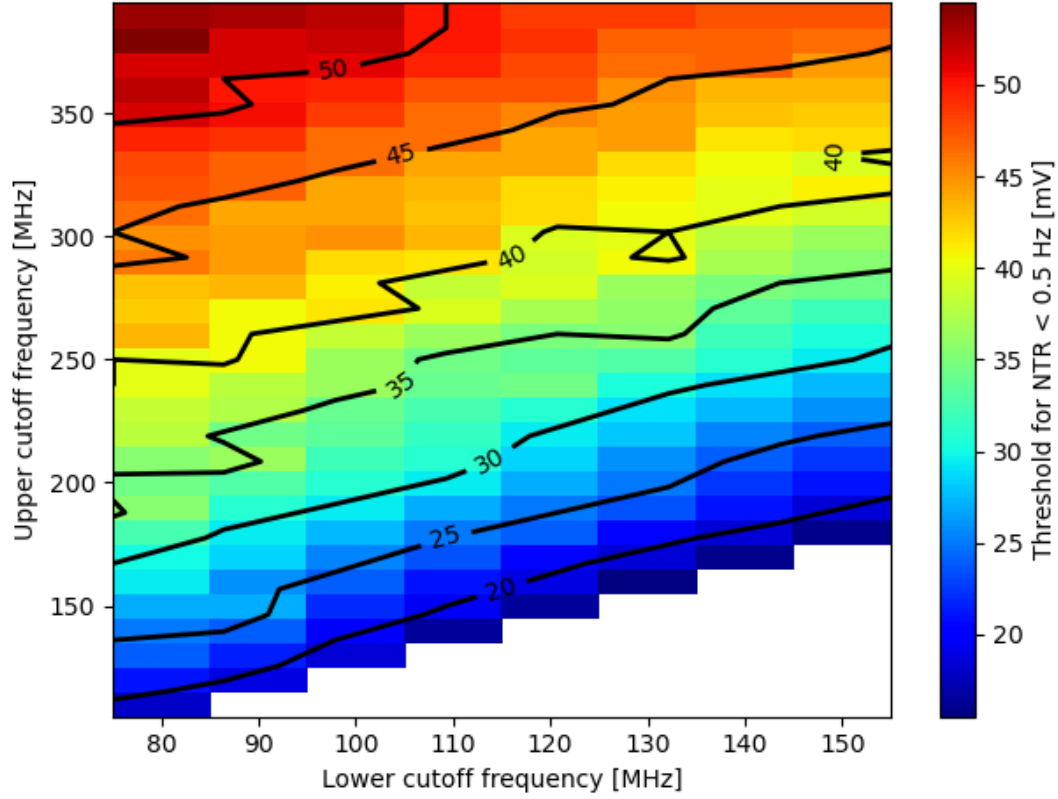


Figure 46: Thresholds for a noise trigger rate  $< 0.5$  Hz (color and iso-voltage lines) as function of lower cutoff frequency (x-axis) and upper cutoff frequency (y-axis).

is constant over frequency.

The passband and the corresponding threshold are tested on the air shower set described in Sec. 4.1. It is important to figure out, how much a slightly higher threshold in the lower passbands from 80 MHz to 130 MHz is relevant for air shower signals which have their maximum at 80 MHz.

The results for three different energy bins are shown in Fig. 47 and Fig 48. While the two lower energy bins contain the full zenith angle band from  $0^\circ$  to  $90^\circ$ , in the highest energy bin, only one air shower is more inclined than  $80^\circ$ , therefore this one is taken out. The last diagram shows the zenith band  $60^\circ$  to  $80^\circ$  in which most neutrino and muons are expected (compare to Fig. 18). With increasing energy the effective area of one station increases drastically.

For the energy interval  $1 \times 10^{16}$  eV– $3.2 \times 10^{16}$  eV only statistical fluctuations are visible. The fraction of triggered air showers in all passbands are too low to determine a

passband. Towards higher energy the sensitivity of the detector increases, which makes the differences between the passbands better visible. The frequency spectrum of the air showers stay unchanged. Overall, a passband at lower frequencies is preferred. In the  $10^{18} \text{ eV} - 3.2 \times 10^{18} \text{ eV}$  energy a passband starting at 80 MHz is in favor. The maximum effective area is from 80 MHz to 120 MHz. This passband is also preferred when looking at an arrival direction of  $60^\circ$  to  $80^\circ$  in Fig. 48 bottom.

Hardware wise, it is difficult to have such a narrow bandwidth filter, especially compared to the broad band sensitivity of the antenna. Therefore a bandpass filter of 80 MHz to 180 MHz will be implemented in the trigger. The effective area will decrease slightly, at the same time the robustness against noise increases. This is important because no measurements are done at summit station so far. If an unexpected noise source occurs within the chosen bandwidth it will be difficult to change the trigger settings accordingly. With a larger bandwidth more frequencies are taken into account and single peaks have less influence. Because the frequency band still starts at 80 MHz the maximum of the signal frequency spectrum will still be measured.

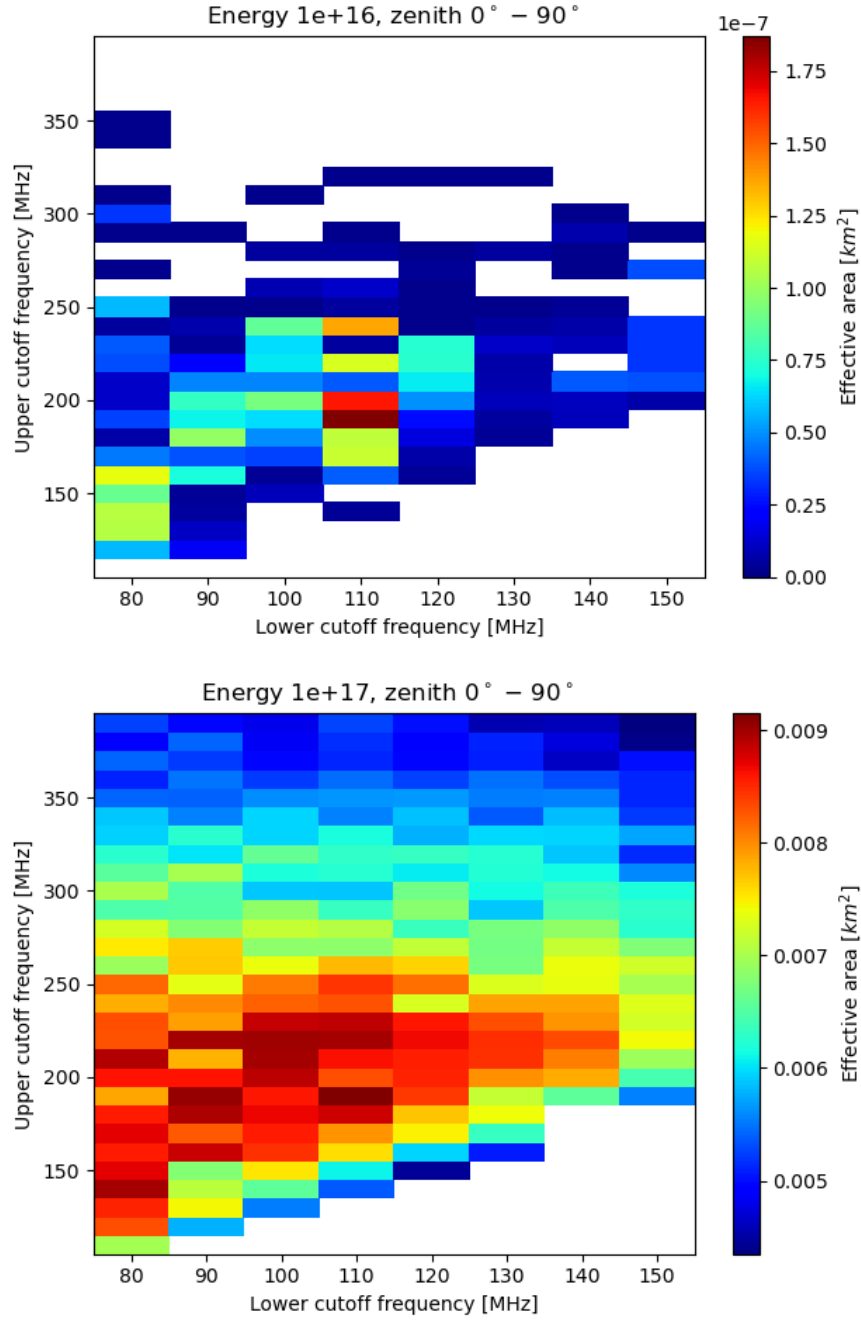


Figure 47: Effective area for different energy intervals and zenith angles. Top left:  $10^{16}$  eV –  $<10^{17}$  eV for zenith angles from  $0^\circ$  to  $90^\circ$ . Top right:  $10^{17}$  eV –  $<10^{18}$  eV for zenith angles from  $0^\circ$  to  $90^\circ$ .



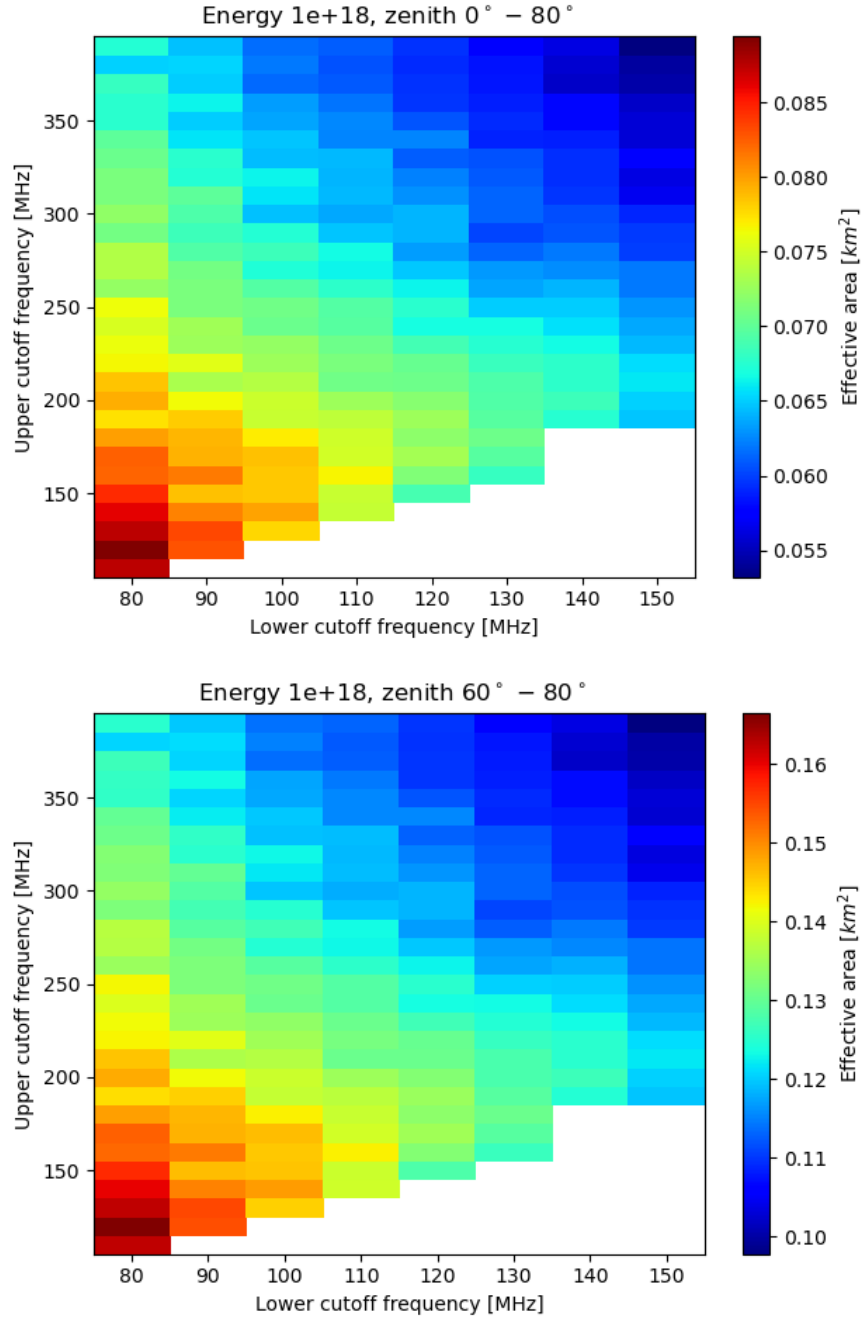


Figure 48: Effective area for different energy intervals and zenith angles. Bottom left:  $10^{18}\text{ eV} - <3.3 \times 10^{18}\text{ eV}$  for zenith angles from  $0^\circ$  to  $80^\circ$ . Bottom right:  $10^{18}\text{ eV} - <3.3 \times 10^{18}\text{ eV}$  for zenith angles from  $60^\circ$  to  $80^\circ$ , which corresponds to the arrival direction from which most neutrinos and muons are expected.

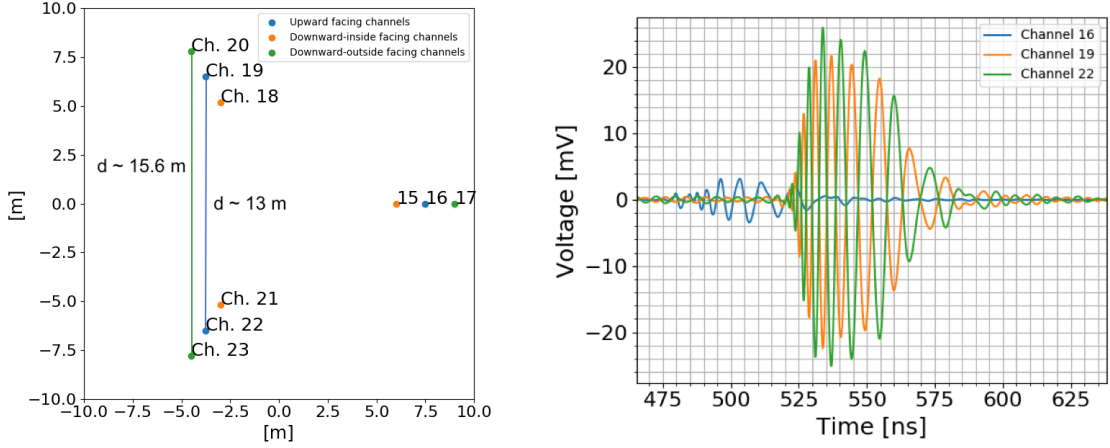


Figure 49: Left: Visualization of the antenna positions for the surface component of one station. The color code indicates the orientation of the antenna. The lines show the distance between antennas. Right: Channel traces for an air shower arriving at  $\theta = 85^\circ$  from a direction aligned with the channels 15 to 17. The time interval between the upward facing channels (16, 19, 22) matches the calculations based on distance and velocity of light in ice.

#### 4.4 Coincidence

The coincidence check includes the number of channels which have to pass the threshold, and a time interval within the threshold exceed must occur. The time interval is set according to the time a radio signal needs to travel the distance between two antennas. The velocity of the radio signal is the velocity of light in media, e.g. air. In Fig. 49 the distances between different antenna position are shown. The longest distance is between two outer antennas ( $\sim 15.6$  m), the radio signal would need  $t = s/c_{\text{air}} \approx 52$  ns. The distance between two upward facing antennas is  $\sim 13$  m, and  $\sim 43$  ns respectively. This time difference is also visible in the traces, shown in Fig. 49 right. Channel 16 records the signal first, later channel 19 and channel 22 measure the signal simultaneously. The shower arrives at  $\theta = 85^\circ$  and a direction ( $\phi = 0^\circ$ ) aligned with the arm hosting channel 15 to channel 17.

The time difference between the starting point of the pulse in channel 16 and channel 22 is roughly  $520 \text{ ns} - 480 \text{ ns} = 40 \text{ ns}$ . This is comparable to  $43 \text{ ns}$  predicted by the velocity of light in air. The difference of  $3 \text{ ns}$  is within the uncertainty due to the scale of the grid. The number coincidence is tested on a broad time window, here  $80 \text{ ns}$ , to avoid that any channel is excluded due to the timing. Fig. 50 compares the effective area of one station

Passband	Coincidence number	Threshold
80 – 120 MHz	1	28 mV
	2	21.5 mV
	3	19 mV
80 – 180 MHz	1	42 mV
	2	31.5 mV
	3	28 mV

Table 6: Calculated threshold for a noise trigger rate  $< 0.5$  Hz. Shown are the values for different passbands and coincidence numbers. The coincidence window is set to 80 ns.

for one, two or three coincidences. The threshold changes due to different noise trigger rates. The threshold is expected to be high, if the noise needs to pass the threshold only once. The threshold decreases the more coincidences are required. The values for the different coincidences are listed in Tab. 6. The requirement of two coincidences lowers the threshold significantly. Three coincidences still decreases the threshold, but the effect is smaller.

The highest effective area is achieved when having a coincidence of two channels. The third channel passes less often. Since the threshold at two coincidences is lower, two coincidences are chosen.

The coincidence window is large compared to the calculated 43 ns. Therefore different time windows in which the coincidence need to happen are tested, here 50 ns, 60 ns, and 80 ns. The threshold changes only a little bit, see Tab. 7.

The effective area for the different coincidence windows is shown in Fig. 51. A coincidence window of 60 ns seems to be in favor, but since the threshold changes only minimally, no real influence is identifiable at this scale.

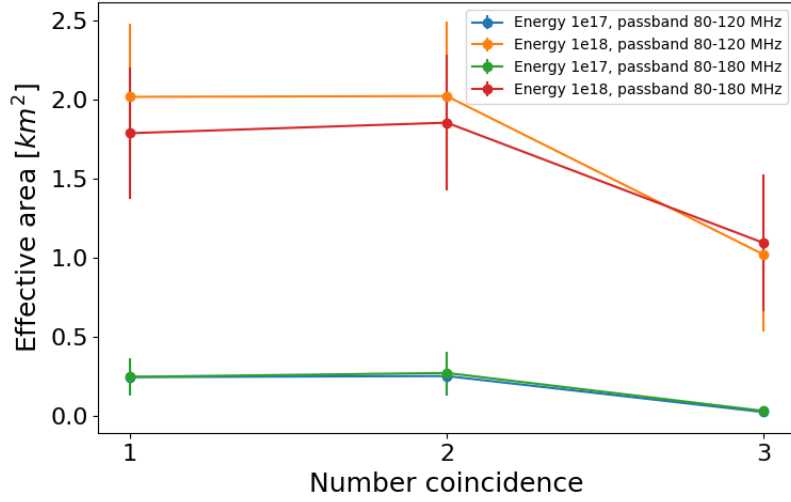


Figure 50: Effective area for one station calculated for different coincidence numbers (x-axis) The colors indicate different energy bins and passbands. A number coincidence of two channels is in favor.

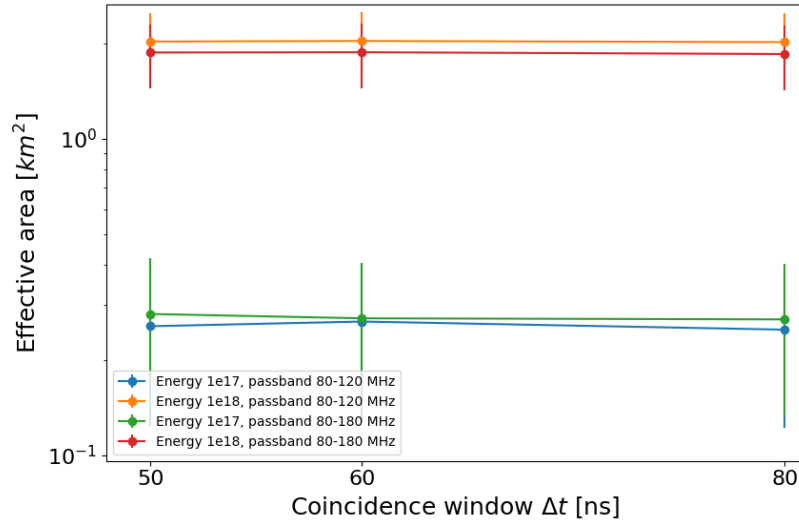


Figure 51: Effective area for one station calculated for different coincidence windows (x-axis). The colors indicate different energy bins and passbands. A coincidence window of 60 ns for two channels seems slightly preferable.

Passband	Coincidence window	Threshold
80 – 120 MHz	50	21 mV
	60	21 mV
	80	21.5 mV
80 – 180 MHz	50	31.5 mV
	60	31.5 mV
	80	32 mV

Table 7: Calculated threshold for a noise trigger rate  $< 0.5$  Hz. Shown are the values for different passbands and coincidence windows. The number coincidence is set to two, following the previous calculations. The changes in the time window are too small to have a real influence on the trigger rate.

	Optimal Passband	Hardware compatible Passband
Trigger Passband	80 – 120 MHz	80 – 180 MHz
Threshold	21 mV	31.5 mV
Coincidence window	60 ns	60 ns
Coincidence number	2	2

Table 8: Optimized trigger settings for two passbands.

## 4.5 Optimal trigger settings

The previous sections suggest a passband starting from 80 MHz. While simulations show a bandwidth of 40 MHz to be optimal, this is difficult to implement in hardware. Therefore a system compatible passband of 80 MHz to 180 MHz will be built, which makes the trigger more robust against noise. The coincidence check implies a time interval of 60 ns in which two channels need to exceed the threshold. The corresponding threshold is 31.5 mV according to a noise trigger rate smaller than 0.5 Hz. The parameter for both passbands are shown in Tab. 8.

The implementation of the bandpass filter in hardware will be difficult. In simulation a bandpass with a sharp cutoff (order 10, see Fig. 52 left) was assumed. Hardware wise, it is unlikely to get a high rejection at frequencies above 500 MHz without good isolation. Therefore the cutoff implemented will fall slower, more like a Chebyshev filter of 3rd

order, shown in Fig. 52 right. This means, that frequencies outside the band are less suppressed and introduce additional noise.

Once the station is deployed it will be possible to adjust the threshold. This provides the opportunity to account for differences between the simulated and implemented filters. The threshold controls the trigger rate, therefore a high noise trigger rate due to unknown sources of noise can be avoided. The adjustment is not possible for the chosen bandpass. The coincidence check is also programmable, this means, that it can be adjusted to the given conditions once the station is deployed.

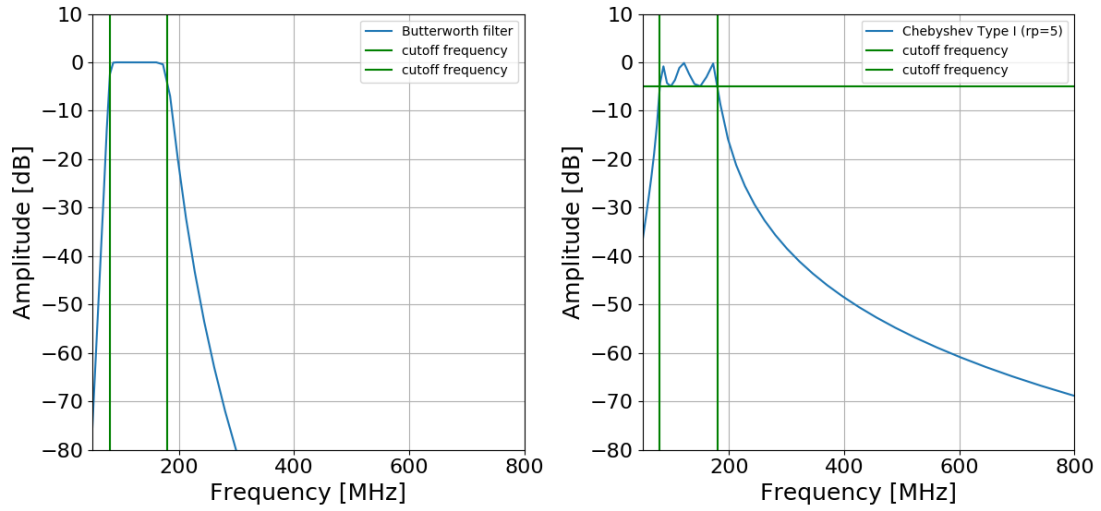


Figure 52: Comparison of a analog Butterworth filter of order 10 (left) used in the simulation studies and a Chebyshev filter of 3rd order (right) which models the filter used in the hardware. Shown is the amplitude of suppression for different frequencies. The green lines indicate the cutoff frequencies.

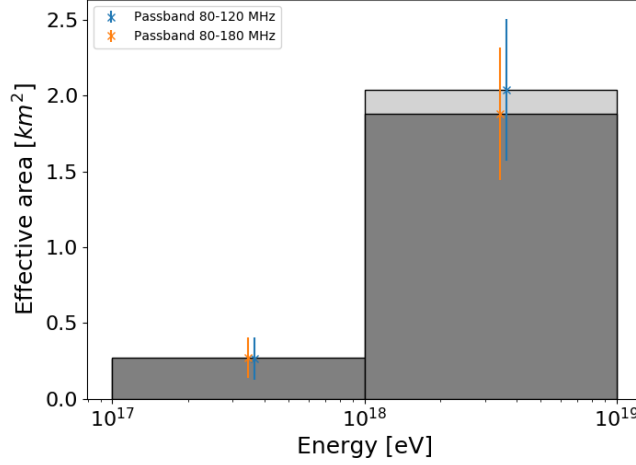


Figure 53: Projected effective area of one RNO-G station shown for different energy bins and passbands. The indicated uncertainty is the 68% CL. The energy refers to the energy of the cosmic ray. The grey bars indicate the width of the energy bin. The markers are placed next to each other to improve readability

## 5 Efficiency analysis

Following the optimization of the surface trigger parameters, the efficiency in detection air showers and the expected number of measured air showers will be calculated. To obtain the muon veto efficiency the triggered muons have to be investigated more in detail. The last sections discuss the implications for RNO-G and further improvements of the analysis.

### 5.1 Air shower efficiency

The air shower efficiency is expressed as effective area per station. The effective area describes the area around a station in which a shower with a certain energy and arrival direction will be detected. The projected area of the detector was taken into account. The calculation method is described in Sec. 4.1.

In Fig. 53, the effective area for different cosmic ray energy bins is shown. If the cosmic ray has a higher energy, a larger area is visible on ground. For energies in the range of  $1 \times 10^{16}$  eV to  $1 \times 10^{17}$  eV the effective area is negligibly small, and therefore not shown. The difference between the optimized passband from 80 MHz to 120 MHz and the hardware compatible passband from 80 MHz to 180 MHz is only visible at high energies.

In Fig. 54 the distribution of the effective area over different zenith intervals is shown.

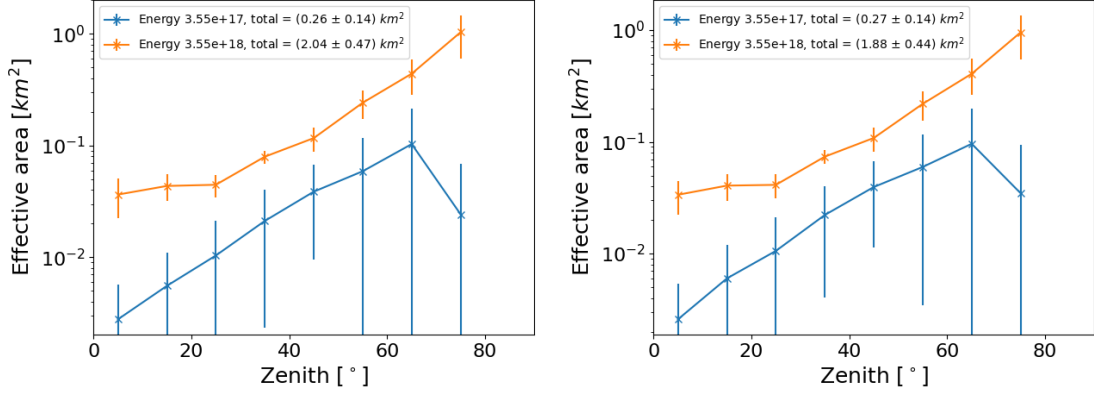


Figure 54: Projected effective area of one RNO-G station shown for different zenith angles. The total number is the effective area for one energy bin. The energy stated in the label is the center of the energy bin. The marker is in the center of the zenith bin. The indicated uncertainty is the 68% CL. Left: Passband 80 MHz to 120 MHz. Right: Passband 80 MHz to 180 MHz

The zenith angle refers to the arrival direction of the cosmic ray. Because only one shower was simulated for  $\theta > 80^\circ$  in the higher energy bin, the zenith is only shown up to  $80^\circ$ . The footprint of an air shower gets larger and fainter for inclined showers. Therefore the effective area increases with higher zenith angles only for higher energies. For energies between  $1 \times 10^{17}$  eV and  $1 \times 10^{18}$  eV the effective area peaks in the zenith bin from  $60^\circ$  to  $70^\circ$ . This means, one station is most sensitive to showers which have an energy above  $1 \times 10^{18}$  eV and are inclined ( $>60^\circ$ ). The different passbands only make a difference at energies above  $1 \times 10^{18}$  eV. The error bars shown indicate the uncertainty of a 68% CL of the effected area.

A similar approach to lower the energy threshold for the detection of  $\gamma$ -ray induced air showers by optimizing the observed frequency bands was taken in [21]. They are suggesting a passband from 100 MHz to 190 MHz. In difference to the simulation done for RNO-G, not the lowest lower cutoff frequency is in favor. This might be explained by a higher galactic noise at South Pole (the galactic center is visible there), since this is the dominant noise in lower frequency range. This explanation contradicts the stated detection efficiency in the paper. In [21] a detection efficiency of 100 % is claimed for  $\gamma$ -ray induced air showers with energies above  $1.4 \times 10^{15}$  eV. In order to measure air showers with this energy, the threshold, and the noise respectively should be substantially lower than assumed in Greenland. The shown noise temperature differs only slightly from the



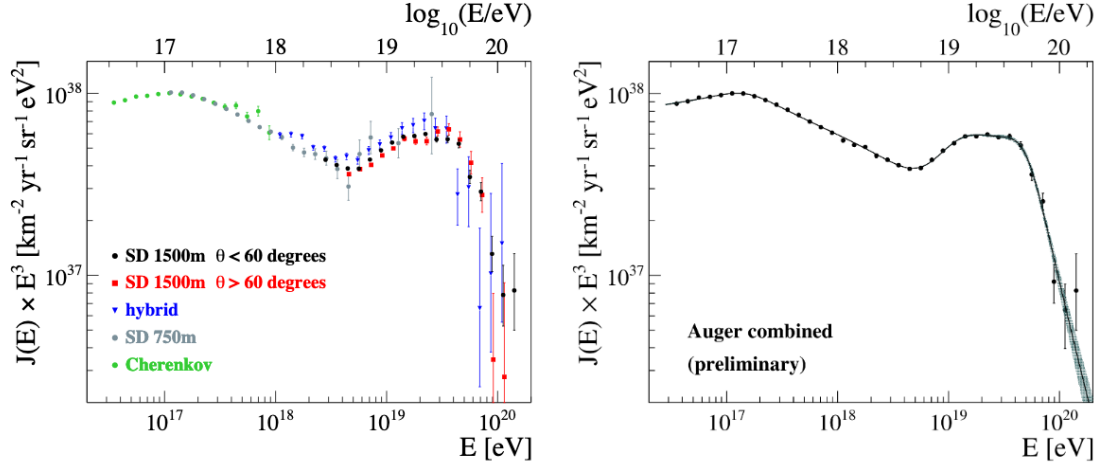


Figure 55: Energy spectra measured using the Pierre Auger Observatory. Left: Several independent and complementary data sets, namely events detected with the the surface detector (SD), hybrid events, detected with the fluorescence detector and at least one water-Cherenkov detector, and events detected with the High Elevation Auger Telescopes (HEAT), here labeled as Cherenkov. Right: Spectrum obtained by combining the different measurements. Fig. from Ref. [76]

RNO-G assumptions. An other reason could be that different antennas and hardware is used. The spacing between the antennas is only 125 m. A detailed check of the signal chain could provide a better insight.

## 5.2 Expected number of events

In order to determine the expected numbers of cosmic ray events, the flux  $J$  of cosmic rays at different energies  $E$  and the solid angle  $\Omega$  of the visible sky has to be taken into account. It follows:

$$N_{\text{CR}} = A_{\text{eff}}^{\text{proj}} \cdot \int \int J \cdot \Omega dE dt \quad (20)$$

The solid angle depends on the zenith bin with the limits  $\theta_1, \theta_2$  and on the azimuth  $\phi$ . Since all azimuth angles are visible, the integral over  $d\phi$  yields  $2\pi$ .

$$\Omega = \int_{\phi_1}^{\phi_2} \int_{\theta_1}^{\theta_2} \sin(\theta) d\theta d\phi = 2\pi \cdot (1 - \cos(\theta_2)) - (1 - \cos(\theta_1)) \quad (21)$$

The cosmic ray flux from  $1 \times 10^{16.5}$  eV to  $1 \times 10^{20}$  eV is measured and published by the Auger collaboration [76], see Fig. 55. The flux steepens from  $1 \times 10^{17}$  eV up to  $3 \times 10^{18}$  eV, afterwards the flux increases again.

Energy bin [eV]	$E \cdot J [m^{-2}s^{-1}sr^{-1}]$	Effective area [ $m^2$ ]	Number of CR [1/day]
$1 \times 10^{17} - 1 \times 10^{18}$	$1.493 \times 10^{-10}$	$271\,064 \pm 135\,287$	$3.05 \pm 1.69$
$1 \times 10^{18} - 1 \times 10^{19}$	$7.935 \times 10^{-13}$	$1\,878\,547 \pm 437\,034$	$0.12 \pm 0.03$

Table 9: Flux from the Auger combined spectrum (ICRC 2019) [76]. The flux  $J$  is converted to two energy bins. The effective area and the numbers of cosmic rays are calculated for one RNO-G station with a trigger passband of 80 – 180 MHz. The uncertainty is the 68% CL of the effective area.

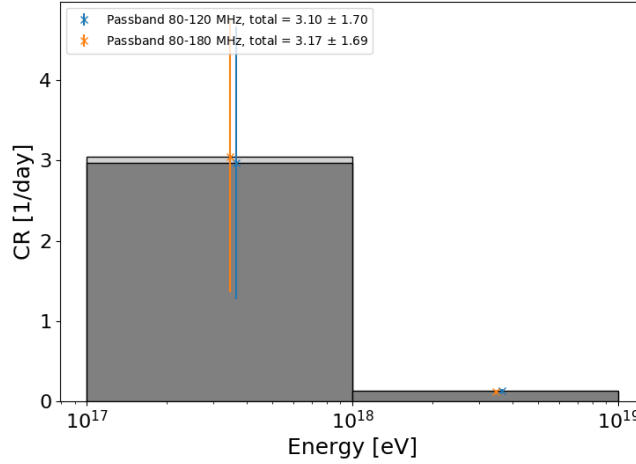


Figure 56: Expected numbers of cosmic rays detected with one RNO-G station per energy bin. The uncertainty is the 68% CL of the effective area. The markers are placed next to each other to improve readability.

The published data is converted to two energy bins. The results are shown on Tab. 9. The flux in the energy bins differ by a factor  $10^3$ . Although the effective area for the higher energy bin is larger, more cosmic rays are expected to be detected with energies between  $1 \times 10^{17}$  to  $1 \times 10^{18}$  (see Fig. 56).

In Fig. 57, the expected number of detected cosmic rays for one RNO-G station per zenith angle bin are shown. While in the energy bin from  $1 \times 10^{18}$  to  $1 \times 10^{19}$  the contribution to the total number of cosmic ray events of a zenith bin increases slightly with inclination, the lower energy bin has a maximum between  $60^\circ$  to  $70^\circ$ . This matches the calculation of the effective area (see Fig. 54), where this zenith bin was slightly higher. Due to the differences in the flux, this feature becomes more visible, and should be proven by measurements. The indicated error bars only show uncertainties due to the effective area. Systematic uncertainties due to the antenna response, the filter used in hardware,

the noise temperature of the system which will be build or the energy scale of the cosmic ray flux are not included in the calculations and will affect the total numbers of cosmic rays detected.

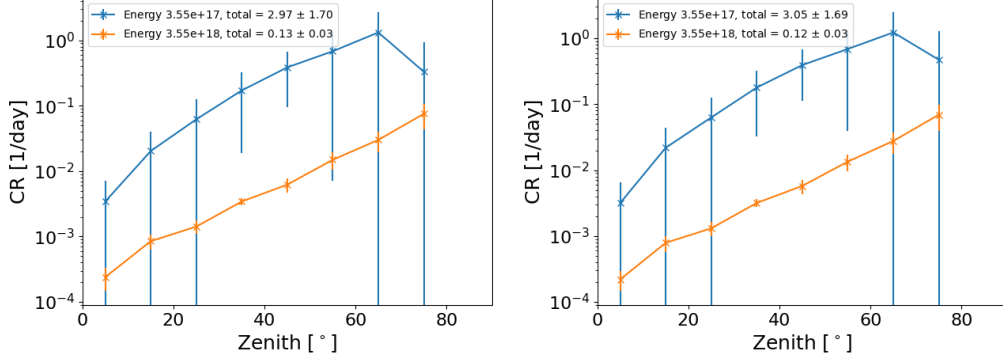


Figure 57: Expected numbers of cosmic rays detected with one RNO-G station for different zenith angles. The energy stated in the label is the center of the energy bin. The flux is expected to be isotrop. The uncertainty is the 68% CL of the effective area. Left: Passband from 80 – 120 MHz. Right: Passband from 80 – 180 MHz.

### 5.3 Muon veto efficiency

For RNO-G it is necessary to estimate the efficiency to veto air showers which are expected to produce a muon. This muon can produce a particle cascade in ice on which the phased array triggers. This leads to a false positive detection of a neutrino event.

The air shower detection efficiency is dependent on the shower energy, the arrival direction and the distance from the shower core to the station. The stations are separated by 1 km (next neighbor) and 1.4 km (diagonal neighbor). Inside the RNO-G array, a shower should be measured by a station within  $\sim 700$  m given that the induced voltage is high enough. The trigger efficiency was calculated using the total set of 407 air showers and divide them into different energy, zenith and distance bins. Afterwards the fraction of the shower that triggers was determined for each bin. The simulated results are illustrated in Fig. 58. For energies between  $1 \times 10^{18}$  to  $3.2 \times 10^{18}$  almost every shower can be detected, if it is within 100 m of a station. The highest detection efficiency for this energy bin is reached for zenith angles between  $50^\circ$  to  $60^\circ$ . For energies between  $1 \times 10^{17}$  to  $3.2 \times 10^{17}$  the highest detection efficiency is for less inclined angles is around  $40^\circ$  to  $50^\circ$ . This can be explained with the shower footprint. For more inclined shower the footprint

becomes larger and fainter. The measured voltage at the antenna is therefore smaller at higher angles. Air shower with energies above  $1 \times 10^{19}$  eV are rare, and no simulations were done at these energies. However, with higher energies the amplitude is expected to scale linearly. Therefore the trigger efficiency is expected to increase further.

To determine the veto efficiency, the muons inducing a shower in the ice on which the phased array triggers have to be known. The trigger efficiency of an air shower depends on its energy, zenith angle and distance to station. These parameters have to be obtained from each muon. It is assumed that the muon direction is the same as the shower arrival direction. The distance from air shower core to station can be deducted from the muon vertex position in ice. The vertex position can be projected along the arrival direction onto ground (here border between ice and air). This yields the core position where the air shower axis reaches the ground.

By evaluating the simulations done for [36] the muon energy, the arrival direction and the distance between core and station can be analyzed. The number of triggered muons per station and year was calculated by [36] and shown in Fig. 59. Muons with an energy around  $1 \times 10^{16}$  eV trigger most often. At lower muon energies the calculated number of triggered muons decreases, but the uncertainties are greater.

Fig. 60 shows a distribution of muons that trigger the in ice array with respect to the distance between station and air shower core. The simulated muon energy is in the range from  $1 \times 10^{15}$  eV to  $3 \times 10^{18}$  eV. The black line shows the total distribution for all energy and zenith bins. The most muons stem from an air shower with a core position within 700 m around a station. After 700 m, the trigger efficiency on air showers decreases fast. For inside the array it follows, that the station that records the muon trigger in ice is not necessarily the same as the station which is closed to the air shower. That means, that all stations have to be evaluated together to identify a possible muon trigger. On the left-hand side of Fig. 60, it is visible that muons with energies between  $3 \times 10^{15}$  eV to  $1 \times 10^{17}$  eV make 85% of the total number of muons. Muons with lower energy are more likely to trigger near the station. For energies up to  $3 \times 10^{16}$  eV, all muons are expected to stem from a shower within 700 m of a station. The zenith distribution on the right-hand side shows the biggest contribution from muons and air showers which arrive under a zenith angle between  $40^\circ$  to  $60^\circ$ . Every zenith bin has its maximum around 300 m, the maximum decreases with a higher inclination. The core positions of air showers that

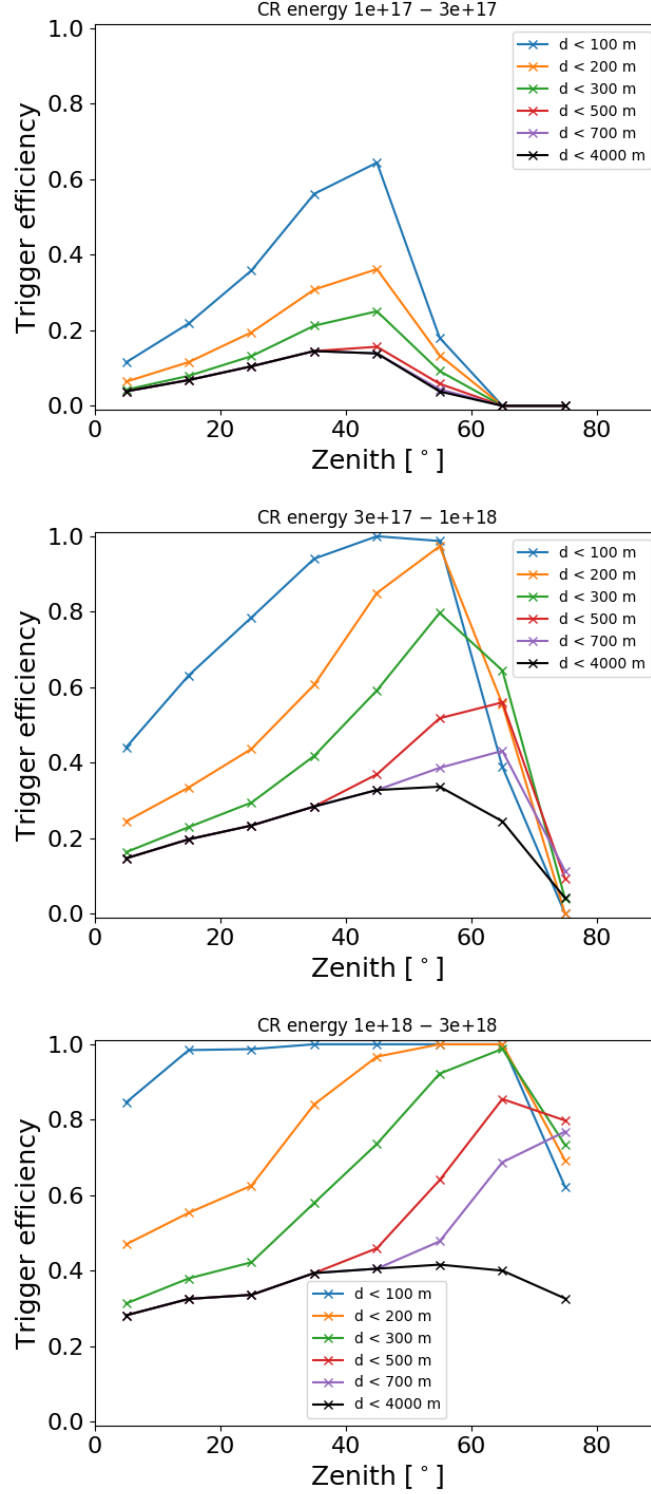


Figure 58: Simulated trigger efficiency on air showers shown for different zenith angles and different distances between station and shower core. The black line indicates the average efficiency for all distances within the footprint. Top: Energy bin from  $1 \times 10^{17}$  to  $3.2 \times 10^{17}$ . Mid: Energy bin from  $3.2 \times 10^{17}$  to  $1 \times 10^{18}$ . Bottom: Energy bin from  $1 \times 10^{18}$  to  $3.2 \times 10^{18}$ .

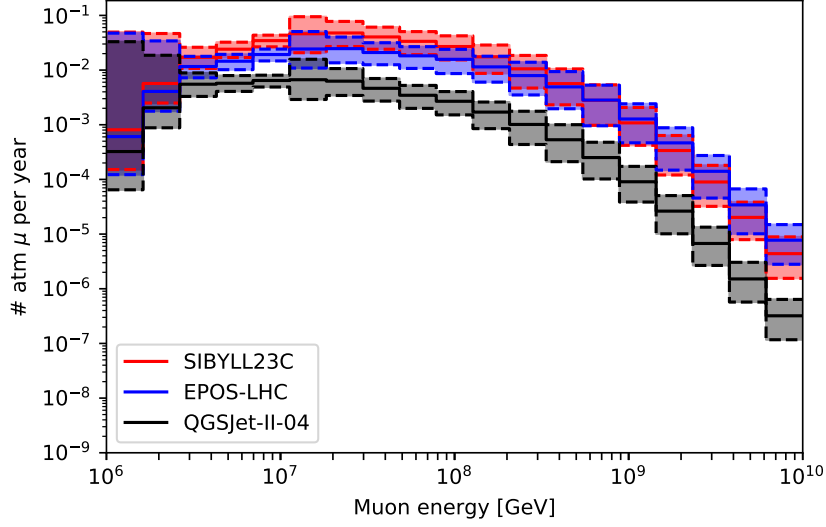


Figure 59: Number of triggered atmospheric muons per station per year at Summit Station. Each color represents a different hadronic model, as specified in the legend. The bands include the range of expected events for the different simulated thresholds of the in ice trigger as well as the 68 % CL contour corresponding to the effective area uncertainty.

arrive with a zenith angle up to  $41^\circ$  is most likely within 600 m around a station. More inclined muons can reach greater distances, therefore their local maximum is lower.

To obtain the muon veto efficiency the Bayes' theorem can be used. The probability to veto a muon  $\mu$  given an energy  $E_\mu$ , zenith angle  $\theta$  and the distance  $d$  between core and station can be calculated with:

$$p(\text{veto}|\mu(E_\mu, \theta, d)) = \sum_i p(\text{trigger}_{\text{CR}}|\text{CR}_i(E_{\text{CR}}, \theta, d) \cdot p(E_{\text{CR},i}|E_\mu) \quad (22)$$

As mentioned before, the arrival direction for cosmic ray induced air shower and muon are assumed to be the same. The probability to trigger on a cosmic ray air shower with energy  $E_{\text{CR}}$ , zenith angle  $\theta$  and distance  $d$  written as  $p(\text{trigger}_{\text{CR}}|\text{CR}(E_{\text{CR}}, \theta, d))$  can be drawn from the previous calculations. The mapping between the shower energy and the resulting muon is more challenging.

The cosmic ray spectrum at energies between  $1 \times 10^8$  eV to  $1 \times 10^{20}$  eV is taken from [30]. To obtain the total muon flux for different energies and zenith angles the Software MCEq (Matrix Cascade Equations) described in [33, 34] is used. To connect muon energy and cosmic ray energy, the cascade equations of a cosmic ray air shower have to be solved.

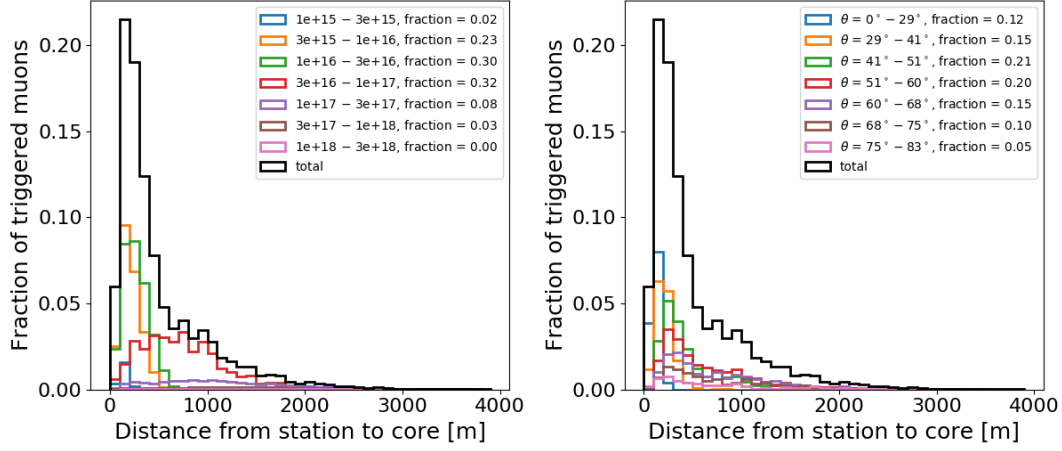


Figure 60: Simulations for muons which trigger the phased array in ice. The black line shows the distribution for muons according to their fraction on different distances (in 100 m bins), including all energy and zenith bins. The black line is normalized to one. The different colors indicate different energy bins (left) and zenith bins (right) and their fraction of all neutrinos.

This is done for different particles types of the primary ( $pr$ ) cosmic ray, namely proton, helium, carbon and iron, and for different cosmic ray energies (10 bins between  $1 \times 10^{15}$  eV to  $1 \times 10^{20}$  eV). The four elements are selected to model different masses. Once the muon flux for a specific cosmic ray induced shower is known, it has to be folded with the actual number of the primary to obtain the muon flux for all cosmic rays. The number of the different primaries can be drawn from the total cosmic ray flux, here calculated from [30]. The muon flux shows, that a muon with a specific energy can stem from different cosmic rays with different energies. The probability  $p(E_{\text{CR}}|E_{\mu})$  is calculated by

$$p(E_{\text{CR}}|E_{\mu}) = \frac{\sum_{pr} N_{\mu}(E_{\text{CR}}, E_{\mu}, \theta, pr) \cdot N_{\text{CR}}(E_{\text{CR}}, \theta, pr)}{\sum_{E_{\text{CR}}} \sum_{pr} N_{\mu}(E_{\text{CR}}, E_{\mu}, \theta, pr) \cdot N_{\text{CR}}(E_{\text{CR}}, \theta, pr)} \quad (23)$$

The number of muons  $N_{\mu}$  is calculated for each shower, therefore it has to be summed over all possible primaries  $pr$ . The number of cosmic rays  $N_{\text{CR}}$  is calculated from the cosmic ray flux and also need to be summed over all primaries. This sum is normalized by summing over all possible cosmic ray energies the muon can stem from.

The distribution for different muon energies stemming from a cosmic ray with a certain energy is shown in Fig. 61.

The plot shows, that a muon with a given energy can stem from air showers with  $\sim 5$  different cosmic ray energies, meaning difference of  $\sim$  a factor 100. In general, the

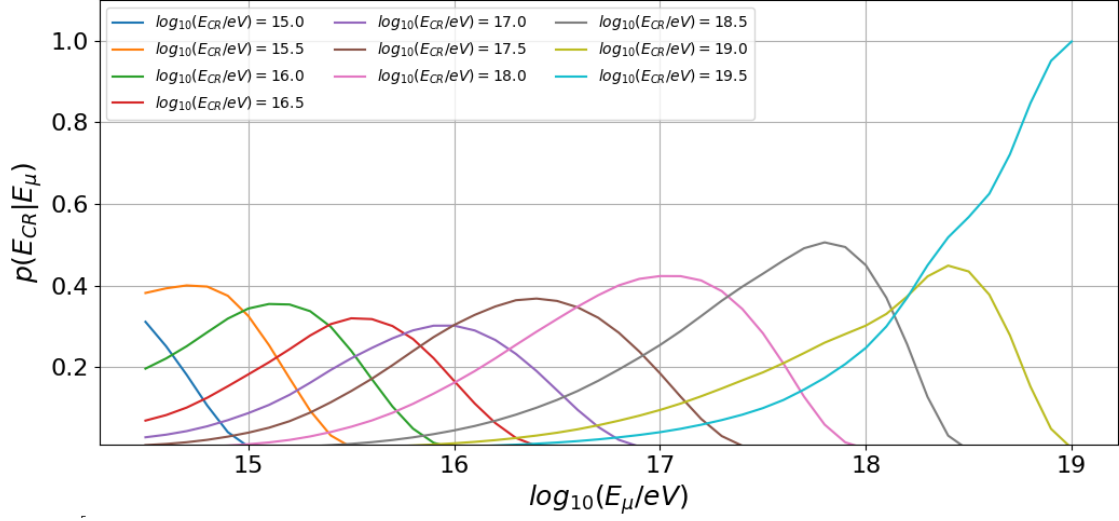


Figure 61: Distribution of the probability for a cosmic ray with a given energy to produce muons with the shown energy. The different colors indicate different cosmic ray energies. The x-axis indicates the energy of the produced muon, the y-axis shows the probability that a cosmic ray with the energy indicated in the label produce a muon.

cosmic rays are most likely to produce a muon with an energy  $\sim$  factor 10 lower. Muons with an energy of  $1 \times 10^{15}$  eV still trigger the phased array. The lowest possible energy of an air shower they could stem from is  $3 \times 10^{15}$  eV. Unfortunately, the surface detector is only sensitive from  $1 \times 10^{17}$  eV on, which reduces the veto efficiency for muons with energies  $< 1 \times 10^{16}$  eV. For air showers above  $3 \times 10^{18}$  eV no simulations were made, and therefore no trigger efficiency is determined. Therefore, the trigger efficiency is assumed to be constant from  $3 \times 10^{18}$  eV on.

To obtain the veto efficiency, the muon are sorted based on its muon energy and zenith angle to stem from an air shower with a certain energy. For each of these possible air showers a trigger efficiency is assigned according to the core position (derived from the muon vertex) and the zenith angle (same as muon zenith angle). To obtain the veto efficiency for one muon the weighted mean of the probabilities to trigger on the possible air showers is calculated. The results are shown in Fig. 62. For air showers with a energy higher than  $3 \times 10^{17}$  eV the trigger efficiency is assumed to be constant, because no simulations were made. Therefore, the veto efficiency is underestimated for these energies in comparison with the lower energies. So far, the veto efficiency is only calculated for one station, considering only muons with a core position closer than 700 m.



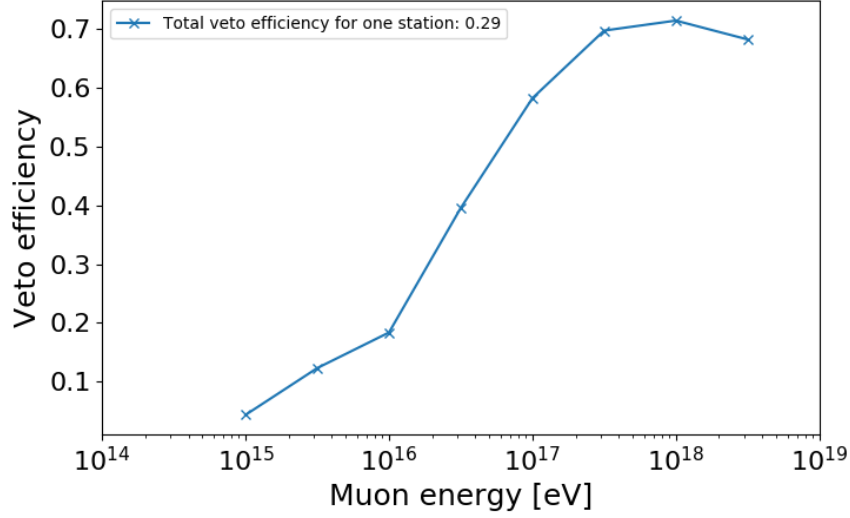


Figure 62: Veto efficiency for muons with different energies for one station. Only muons that stem from an air shower with a core position closer than 700 m are taken into account. The trigger efficiency above  $3 \times 10^{18}$  eV is assumed to be constant.

The overall veto efficiency is 29 %. If a full array is built, a muon with a distance greater than 700 m is more likely to be vetoed by a different station, which is closer to the shower core. This holds not true for air showers with a core position outside of the array. The muon can still trigger on a station at the edge of the array. Therefore, in-ice trigger at the edge of the array have a smaller veto efficiency and should be studied carefully.

#### 5.4 Implications for RNO-G and further improvements

The previous study shows, that three upward facing LPDAs at the surface of each station are able to detect air showers and provide a veto mechanism on muon events. Simulations with the optimized trigger settings indicate, that air showers from  $1 \times 10^{17}$  eV can be detected, especially if they are close to a station. For lower energies, the noise needs to be lower than expected. This could be true, if the temperature of the system is smaller than assumed. So far, no in field measurements are provided.

For RNO-G, the measurement of cosmic rays comes with many advantages. Cosmic rays are a good calibration source for the surface component and the in-ice detector. The radio pulse of an air shower is very similar to an Askaryan pulse expected from a neutrino event. Both are very short bipolar pulses of just a few nanoseconds length which are difficult to generate artificially. Therefore measuring cosmic rays fully tests

the neutrino detector under realistic conditions. Furthermore, the radio emission of air showers is well understood so that the reconstructed signal properties can be verified by theoretical predictions.

To improve the muon veto, a statistical analysis could help to decide if a in-ice shower is induced by a muon or neutrino. This is important for in-ice trigger at the edges of the array. The trigger efficiency is reduced, because the muon can travel longer distances, while the air shower signal is not detectable at the same place. This estimation could improve if a whole array is simulated instead of a single station. This gives the opportunity to calculate, if the air shower from a muon that travels longer than 700 m is measured by a different station. At the same time, it is possible to check if an air shower is visible at one or more stations at all. The prediction for the muon veto would be also more exact, if CoREAS simulations for air showers with energy above  $3 \times 10^{18}$  eV would be produced. So far it is not done, because these showers are rare and the simulations require computational resources. In general, a more exact prediction of the trigger and veto efficiency would be possible with in field measurements of the noise and the hardware response.

## 6 Summary and Conclusions

Neutrinos are the ideal messenger to identify sources of ultra-high energy cosmic rays in the universe. The main mechanism at the origin of neutrinos is the production of pions in the interactions of cosmic rays with other hadrons or photons. Because of their neutral charge and their interaction channel, neutrinos point straight back to their origin. A promising technique to measure neutrinos above 10 PeV is the detection of radio signals generated by the Askaryan effect. The effect is caused by neutrino-induced particle cascades in dense media e.g. ice.

Starting in 2021, the Radio Neutrino Observatory in Greenland will be deployed. Building on the experience gained with ARA, ARIANNA and ANITA, the detector will be equipped with in-ice detector strings and a surface component. The surface component extends the effective volume of the neutrino detector only slightly, but is also sensitive to signals coming from above, such as from extensive air showers.

Previous studies have shown that muons stemming from an air shower can induce particle cascade in ice which are indistinguishable from real neutrino events. The catastrophic energy loss of a muon may occur as often as detectable neutrino events are expected. Therefore, muons are a non-negligible background. By building the detector with surface antennas the established method of radio detection of extensive air showers can be used to identify incoming muons via their origin, namely the air shower. Once an air shower is detected, the signal is stored and can be used as veto mechanism in the neutrino detection.

To obtain an efficient veto, a surface trigger mechanism has to be developed and optimized. The surface trigger is based on the trace envelope of each channel which has to exceed a simple threshold. Once the signal is recorded, it will be amplified and filtered by a bandpass. A coincidence check including a number of channels which have to pass the threshold within a certain time interval will be performed. The threshold for a corresponding frequency band is obtained by determine a noise trigger rate  $< 0.5$  Hz, which is a data rate the hardware is capable to process. The total noise consists of thermal noise of the system and galactic noise. An analysis based on more than 400 CoREAS air showers suggest a passband from 80 MHz to 120 MHz. Although galactic noise is increased at lower frequencies, the effective area is largest with the lowest possible lower

cutoff frequency (80 MHz). The narrow passband of 40 MHz is difficult to implement in hardware. Therefore a frequency band of 80 MHz to 180 MHz is chosen, which reduces the efficiency slightly, but makes the trigger more robust against noise. By requiring a number coincidence of two channels, the threshold can be lowered significantly. The time window has only little influence on the threshold, but 60 ns seem to be in favor.

The trigger parameters are simulated for different air showers to determine the effective area. One RNO-G station will be sensitive to air showers from  $1 \times 10^{17}$  eV on. The highest effective area is achieved for inclined air showers. In combinations with the cosmic ray flux as measured by the Pierre Auger Observatory the expected number of detected cosmic rays,  $3.17 \pm 1.69$  per day, is obtained. A trigger efficiency of 100 % is achieved for air showers with an energy from  $1 \times 10^{18}$  eV, arriving with a zenith angle between  $60^\circ$  to  $70^\circ$  within 300 m of a station. To obtain the muon veto efficiency, the probability that a muon with a given energy stems from an air shower with a certain energy is calculated. The possible air showers differ in energy by  $\sim$  a factor 100. The probability to trigger on each shower considering cosmic ray energy, arrival direction and position of shower core, is calculated and summed up accordingly. The overall efficiency for one station considering only muons with an air shower core within 700 m around a station is 29 %.

## References

- [1] A. Aab et al. “The Pierre Auger Observatory: Contributions to the 34th International Cosmic Ray Conference (ICRC 2015)”. In: *Proceedings, 34th International Cosmic Ray Conference (ICRC 2015): The Hague, The Netherlands, July 30-August 6, 2015*. 2015. arXiv: 1509.03732 [astro-ph.HE].
- [2] M. G. Aartsen et al. “Differential limit on the extremely-high-energy cosmic neutrino flux in the presence of astrophysical background from nine years of IceCube data”. In: *Phys. Rev. D* 98.6 (2018), p. 062003. DOI: 10.1103/PhysRevD.98.062003. arXiv: 1807.01820 [astro-ph.HE].
- [3] M. Aartsen et al. “Characterization of the atmospheric muon flux in IceCube”. In: *Astroparticle Physics* 78 (2016), pp. 1–27. DOI: <https://doi.org/10.1016/j.astropartphys.2016.01.006>.
- [4] P. Abreu et al. “Antennas for the detection of radio emission pulses from cosmic-ray induced air showers at the Pierre Auger Observatory”. In: *Journal of Instrumentation* 7.10 (Oct. 2012), P10011–P10011. DOI: 10.1088/1748-0221/7/10/p10011.
- [5] M. Ackermann et al. “The spectrum of isotropic diffuse gamma-ray emission between 100 MeV and 820 GeV”. In: *Astrophys. J.* 799 (2015), p. 86. DOI: 10.1088/0004-637X/799/1/86. arXiv: 1410.3696 [astro-ph.HE].
- [6] H. R. Allan. “Elementary Particle and Cosmic Ray Physics”. In: *Progress in Elementary Particle and Cosmic Ray Physics* 10 (1971), pp. 169–302.
- [7] P. Allison et al. *Constraints on the Diffuse Flux of Ultra-High Energy Neutrinos from Four Years of Askaryan Radio Array Data in Two Stations*. arXiv:1912.00987. 2019.
- [8] P. Allison et al. “Design and Performance of an Interferometric Trigger Array for Radio Detection of High-Energy Neutrinos”. In: *Nucl. Instrum. Meth.* A930 (2019), pp. 112–125. DOI: 10.1016/j.nima.2019.01.067. arXiv: 1809.04573.
- [9] P. Allison et al. “Performance of two Askaryan Radio Array stations and first results in the search for ultrahigh energy neutrinos”. In: *Phys. Rev. D* 93.8 (2016), p. 082003. DOI: 10.1103/PhysRevD.93.082003. arXiv: 1507.08991 [astro-ph.HE].

- [10] P. Allison et al. “Design and initial performance of the Askaryan Radio Array prototype EeV neutrino detector at the South Pole”. In: *Astroparticle Physics* 35.7 (2012), pp. 457–477. DOI: <https://doi.org/10.1016/j.astropartphys.2011.11.010>.
- [11] P. Allison et al. “First constraints on the ultra-high energy neutrino flux from a prototype station of the Askaryan Radio Array”. In: *Astroparticle Physics* 70 (2015), pp. 62–80. DOI: <https://doi.org/10.1016/j.astropartphys.2015.04.006>.
- [12] J. Alvarez-Muñiz et al. “Coherent Cherenkov radio pulses from hadronic showers up to EeV energies”. In: *Astroparticle Physics* 35.6 (Jan. 2012), pp. 287–299. DOI: [10.1016/j.astropartphys.2011.10.002](https://doi.org/10.1016/j.astropartphys.2011.10.002).
- [13] A. Anker et al. “Targeting ultra-high energy neutrinos with the ARIANNA experiment”. In: *Advances in Space Research* 64.12 (Dec. 2019), pp. 2595–2609. DOI: [10.1016/j.asr.2019.06.016](https://doi.org/10.1016/j.asr.2019.06.016).
- [14] ARA Collaboration et al. *Recent Results from The Askaryan Radio Array*. 2019. arXiv: 1907.11125 [astro-ph.HE].
- [15] D. Ardouin et al. “Radio-Detection Signature of High Energy Cosmic Rays by the CODALEMA Experiment”. In: *Nucl. Instrum. Meth. A* 555 (2005), p. 148. DOI: [10.1016/j.nima.2005.08.096](https://doi.org/10.1016/j.nima.2005.08.096). arXiv: [astro-ph/0504297](https://arxiv.org/abs/astro-ph/0504297).
- [16] T. Asch. “Self-triggering of radio signals from cosmic ray air showers”. PhD thesis. 2009. DOI: [10.5445/IR/200074959](https://doi.org/10.5445/IR/200074959).
- [17] G. A. Askar’yan. “Coherent Radio Emission from Cosmic Showers in Air and in Dense Media”. In: *Soviet Journal of Experimental and Theoretical Physics* 21 (May 1965), p. 658.
- [18] P. Auger et al. “Extensive Cosmic-Ray Showers”. In: *Rev. Mod. Phys.* 11 (3-4 July 1939), pp. 288–291. DOI: [10.1103/RevModPhys.11.288](https://doi.org/10.1103/RevModPhys.11.288).
- [19] J. Avva et al. “An in situ measurement of the radio-frequency attenuation in ice at Summit Station, Greenland”. In: *J. Glaciol.* 61 (2015), pp. 1005–1011. DOI: [10.3189/2015JoG15J057](https://doi.org/10.3189/2015JoG15J057). arXiv: 1409.5413 [astro-ph.IM].

- [20] J. Avva et al. “Development Toward a Ground-Based Interferometric Phased Array for Radio Detection of High Energy Neutrinos”. In: *Nucl. Instrum. Meth.* A869 (2017), pp. 46–55. DOI: 10.1016/j.nima.2017.07.009. arXiv: 1605.03525 [astro-ph.IM].
- [21] A. Balagopal V. et al. “Search for PeVatrons at the Galactic Center using a radio air-shower array at the South Pole”. In: *The European Physical Journal C* 78.2 (Feb. 2018). DOI: 10.1140/epjc/s10052-018-5537-2.
- [22] C. B. Barber, D. P. Dobkin, and H. Huhdanpaa. “The Quickhull Algorithm for Convex Hulls”. In: *ACM Transactions on Mathematical Software* 22.4 (Dec. 1996), pp. 469–483. DOI: 10.1145/235815.235821.
- [23] S. W. Barwick et al. “Design and Performance of the ARIANNA HRA-3 Neutrino Detector Systems”. In: *IEEE Trans. Nucl. Sci.* 62.5 (2015), pp. 2202–2215. DOI: 10.1109/TNS.2015.2468182. arXiv: 1410.7369 [astro-ph.IM].
- [24] S. W. Barwick et al. “Constraints on Cosmic Neutrino Fluxes from the Antarctic Impulsive Transient Antenna Experiment”. In: *Phys. Rev. Lett.* 96 (17 May 2006), p. 171101. DOI: 10.1103/PhysRevLett.96.171101.
- [25] S. Barwick et al. “A first search for cosmogenic neutrinos with the ARIANNA Hexagonal Radio Array”. In: *Astroparticle Physics* 70 (2015), pp. 12–26. DOI: <https://doi.org/10.1016/j.astropartphys.2015.04.002>.
- [26] P. Bezyazeev et al. “Measurement of cosmic-ray air showers with the Tunka Radio Extension (Tunka-Rex)”. In: *Nucl. Instrum. Meth. A* 802 (2015), pp. 89–96. DOI: 10.1016/j.nima.2015.08.061. arXiv: 1509.08624 [astro-ph.IM].
- [27] M. Bleicher et al. “Relativistic hadron-hadron collisions in the ultra-relativistic quantum molecular dynamics model”. In: *Journal of Physics G: Nuclear and Particle Physics* 25.9 (Sept. 1999), pp. 1859–1896. DOI: 10.1088/0954-3899/25/9/308.
- [28] R. Bracewell. *The Fourier Transform and its Applications*. Second. Tokyo: McGraw-Hill Kogakusha, Ltd., 1978.
- [29] C. Deaconu et al. “Measurements and Modeling of Near-Surface Radio Propagation in Glacial Ice and Implications for Neutrino Experiments”. In: *Phys. Rev.*

- D98.4 (2018), p. 043010. DOI: 10.1103/PhysRevD.98.043010. arXiv: 1805.12576 [astro-ph.IM].
- [30] H. Dembinski et al. “Data-driven model of the cosmic-ray flux and mass composition from 10 GeV to  $10^{11}$  GeV”. In: *PoS ICRC2017* (2017), p. 533. arXiv: 1711.11432 [astro-ph.HE].
  - [31] H. Falcke et al. “Detection and imaging of atmospheric radio flashes from cosmic ray air showers”. In: *Nature* 435.7040 (May 2005), pp. 313–316. DOI: 10.1038/nature03614.
  - [32] A. Fedynitch et al. “A state-of-the-art calculation of atmospheric lepton fluxes”. In: *PoS ICRC2017* (2017), p. 1019. DOI: 10.22323/1.301.1019.
  - [33] A. Fedynitch et al. “Calculation of conventional and prompt lepton fluxes at very high energy”. In: *EPJ Web of Conferences* 99 (2015), p. 08001. arXiv: 1503.00544 [hep-ph].
  - [34] A. Fedynitch et al. “Hadronic interaction model sibyll 2.3c and inclusive lepton fluxes”. In: *Phys. Rev. D* 100 (10 Nov. 2019), p. 103018. DOI: 10.1103/PhysRevD.100.103018.
  - [35] N. Feigl. “Development of a standard test and calibration procedure for the hardware of the Radio Neutrino Detector RNO-G”. MA thesis. FAU, 2020.
  - [36] D. García-Fernández, A. Nelles, and C. Glaser. “Signatures of secondary leptons in radio-neutrino detectors in ice”. In: *Physical Review D* 102.8 (Oct. 2020). DOI: 10.1103/physrevd.102.083011.
  - [37] F. de Gasperin et al. “Cassiopeia A, Cygnus A, Taurus A, and Virgo A at ultra-low radio frequencies”. In: *Astronomy and Astrophysics* 635 (Mar. 2020), A150. DOI: 10.1051/0004-6361/201936844.
  - [38] C. Glaser et al. “NuRadioReco: A reconstruction framework for radio neutrino detectors”. In: *Eur. Phys. J. C* 79.6 (2019), p. 464. DOI: 10.1140/epjc/s10052-019-6971-5. arXiv: 1903.07023 [astro-ph.IM].
  - [39] C. Glaser et al. “NuRadioMC: simulating the radio emission of neutrinos from interaction to detector”. In: *The European Physical Journal C* 80.2 (Jan. 2020). DOI: 10.1140/epjc/s10052-020-7612-8.



- [40] C. Glaser et al. “Results and Perspectives of the Auger Engineering Radio Array”. In: *EPJ Web of Conferences* 135 (2017). Ed. by S. Buitink et al., p. 01006. DOI: 10.1051/epjconf/201713501006.
- [41] P. K. F. Grieder. *Extensive Air Showers: High Energy Phenomena and Astrophysical Aspects - A Tutorial, Reference Manual and Data Book*. 2010. DOI: 10.1007/978-3-540-76941-5.
- [42] C. Haack, C. Wiebusch, et al. “A measurement of the diffuse astrophysical muon neutrino flux using eight years of IceCube data.” In: *PoS ICRC2017* (2018), p. 1005. DOI: 10.22323/1.301.1005. eprint: 1710.01191.
- [43] A. Hallgreen. “In ice neutrino radio detection projects”. In: *PoS NEUTEL2015* (2016), p. 035. DOI: 10.22323/1.244.0035.
- [44] D. Heck et al. “CORSIKA: A Monte Carlo code to simulate extensive air showers”. In: (Feb. 1998).
- [45] W. Heitler. *The quantum theory of radiation*. Vol. 5. International Series of Monographs on Physics. Oxford: Oxford University Press, 1936.
- [46] S. Hoover et al. “Observation of Ultrahigh-Energy Cosmic Rays with the ANITA Balloon-Borne Radio Interferometer”. In: *Physical Review Letters* 105.15 (Oct. 2010). DOI: 10.1103/physrevlett.105.151101.
- [47] A. Horneffer et al. “Air Shower Measurements with LOFAR”. In: *Nucl. Instrum. Meth. A* 604 (2009). Ed. by F. Ameli et al., S20–S23. DOI: 10.1016/j.nima.2009.03.027. arXiv: 0903.2398 [astro-ph.IM].
- [48] T. Huege, M. Ludwig, and C. W. James. “Simulating radio emission from air showers with CoREAS”. In: (2013). DOI: 10.1063/1.4807534.
- [49] T. Huege. “Radio detection of cosmic ray air showers in the digital era”. In: *Physics Reports* 620 (Mar. 2016), pp. 1–52. DOI: 10.1016/j.physrep.2016.02.001.
- [50] C. W. James et al. “General description of electromagnetic radiation processes based on instantaneous charge acceleration in “endpoints””. In: *Physical Review E* 84.5 (Nov. 2011). DOI: 10.1103/physreve.84.056602.

- [51] C. Kopper et al. “Observation of Astrophysical Neutrinos in Six Years of IceCube Data”. In: *PoS ICRC2017* (2018), p. 981. DOI: 10.22323/1.301.0981. eprint: 1710.01191.
- [52] I. Kravchenko et al. “Performance and simulation of the RICE detector”. In: *Astropart. Phys.* 19 (2003), pp. 15–36. DOI: 10.1016/S0927-6505(02)00194-9. arXiv: astro-ph/0112372 [astro-ph].
- [53] I. Kravchenko et al. “RICE limits on the diffuse ultrahigh energy neutrino flux”. In: *Phys. Rev. D* 73 (8 Apr. 2006), p. 082002. DOI: 10.1103/PhysRevD.73.082002.
- [54] A. A. Lagutin, R. I. Raikin, and T. L. Serebryakova. “Air shower universality from 1014 to 1022 eV”. In: *Journal of Physics: Conference Series* 409 (Feb. 2013), p. 012092. DOI: 10.1088/1742-6596/409/1/012092.
- [55] H. Landsman, L. Ruckman, and G. Varner. “AURA—A radio frequency extension to IceCube”. In: *Nuclear Instruments and Methods in Physics Research Section A: Accelerators, Spectrometers, Detectors and Associated Equipment* 604.1, Supplement (2009). ARENA 2008, S70–S75. DOI: <https://doi.org/10.1016/j.nima.2009.03.030>.
- [56] J. Matthews. “A Heitler model of extensive air showers”. In: *Astropart. Phys.* 22 (2005), pp. 387–397. DOI: 10.1016/j.astropartphys.2004.09.003.
- [57] A. Nelles et al. “Recent results from the ARIANNA neutrino experiment”. In: *EPJ Web of Conferences* 135 (2017). Ed. by S. Buitink et al., p. 05002. DOI: 10.1051/epjconf/201713505002.
- [58] A. de Oliveira-Costa et al. “A model of diffuse Galactic radio emission from 10 MHz to 100 GHz”. In: *Monthly Notices of the Royal Astronomical Society* 388.1 (July 2008), pp. 247–260. DOI: 10.1111/j.1365-2966.2008.13376.x.
- [59] S. Ostapchenko. “Monte Carlo treatment of hadronic interactions in enhanced Pomeron scheme: QGSJET-II model”. In: *Phys. Rev. D* 83 (1 2011), p. 014018. DOI: 10.1103/PhysRevD.83.014018.
- [60] D. C. Price. *Data Files for PyGSM: Python interface to the Global Sky Model*. Zenodo, Oct. 2019. DOI: 10.5281/zenodo.3479985.
- [61] J. Reed. *An Introduction to Ultra Wideband Communication Systems*. Jan. 2005.

- [62] M. Risse. “Properties of extensive air showers”. In: *Acta Phys. Polon. B* 35 (2004). Ed. by M. Jezabek and H. Wilczynski, pp. 1787–1798. arXiv: `astro-ph/0402300`.
- [63] RNO-G Collaboration et al. “Design and Sensitivity of the Radio Neutrino Observatory in Greenland (RNO-G)”. In: *To be submitted for JINST* (2020). arXiv: `2010.12279 [astro-ph.IM]`.
- [64] R. S. Roger et al. “The radio emission from the Galaxy at 22 MHz”. In: *Astronomy and Astrophysics Supplement Series* 137.1 (May 1999), pp. 7–19. DOI: `10.1051/aas:1999239`.
- [65] B. Rossi and K. Greisen. “Cosmic-Ray Theory”. In: *Rev. Mod. Phys.* 13 (4 Oct. 1941), pp. 240–309. DOI: `10.1103/RevModPhys.13.240`.
- [66] G. Rybicki and A. Lightman. *Radiative Processes in Astrophysics*. Physics textbook. Wiley, 2008.
- [67] P. Schellart et al. “Detecting cosmic rays with the LOFAR radio telescope”. In: *Astronomy and Astrophysics* 560 (Dec. 2013), p. 14. DOI: `10.1051/0004-6361/201322683`.
- [68] O. Scholten, K. Werner, and F. Rusydi. “A macroscopic description of coherent geo-magnetic radiation from cosmic-ray air showers”. In: *Astroparticle Physics* 29.2 (Mar. 2008), pp. 94–103. DOI: `10.1016/j.astropartphys.2007.11.012`.
- [69] O. Scholten, K. D. de Vries, and K. Werner. “Coherent radiation from extensive air showers”. In: *Nuclear Instruments and Methods in Physics Research Section A: Accelerators, Spectrometers, Detectors and Associated Equipment* 662 (Jan. 2012), S80–S84. DOI: `10.1016/j.nima.2010.11.125`.
- [70] H. Schoorlemmer et al. “Energy and flux measurements of ultra-high energy cosmic rays observed during the first ANITA flight”. In: *Astroparticle Physics* 77 (Apr. 2016), pp. 32–43. DOI: `10.1016/j.astropartphys.2016.01.001`.
- [71] F. Schröder. “Status of the radio technique for cosmic-ray induced air showers”. In: *Nuclear and Particle Physics Proceedings* 279-281 (Oct. 2016), pp. 190–197. DOI: `10.1016/j.nuclphysbps.2016.10.027`.
- [72] F. Schröder et al. “Tunka-Rex: Status, Plans, and Recent Results (ARENA 2016)”. In: *EPJ Web of Conferences* 135 (Nov. 2016). DOI: `10.1051/epjconf/201713501003`.

- [73] F. G. Schröder. “Radio detection of cosmic-ray air showers and high-energy neutrinos”. In: *Progress in Particle and Nuclear Physics* 93 (Mar. 2017), pp. 1–68. DOI: 10.1016/j.pnnp.2016.12.002.
- [74] J. Schulz et al. “Status and Prospects of the Auger Engineering Radio Array”. In: *PoS ICRC2015* (2016), p. 615. DOI: 10.22323/1.236.0615.
- [75] J. Stachurska et al. *First Double Cascade Tau Neutrino Candidates in IceCube and a New Measurement of the Flavor Composition*. 2020. arXiv: 1908.05506.
- [76] The Pierre Auger Collaboration et al. *The Pierre Auger Observatory: Contributions to the 36th International Cosmic Ray Conference (ICRC 2019)*. 2019. arXiv: 1909.09073 [astro-ph.HE].
- [77] G. Voronoi. “Nouvelles applications des paramètres continus à la théorie des formes quadratiques. Premier mémoire. Sur quelques propriétés des formes quadratiques positives parfaites.” In: *Journal für die reine und angewandte Mathematik* 133 (1908), pp. 97–178.
- [78] K. Werner, K. D. de Vries, and O. Scholten. “A realistic treatment of geomagnetic Cherenkov radiation from cosmic ray air showers”. In: *Astroparticle Physics* 37 (2012), pp. 5–16. DOI: <https://doi.org/10.1016/j.astropartphys.2012.07.007>.
- [79] H. Zheng et al. “An improved model of diffuse galactic radio emission from 10 MHz to 5 THz”. In: *Monthly Notices of the Royal Astronomical Society* 464.3 (Oct. 2016), pp. 3486–3497. DOI: 10.1093/mnras/stw2525.

## List of Abbreviations

ADC	Analog to digital converter
AERA	Auger Engineering Radio Array
ANITA	Antarctic Impulsive Transient Antenna
ARA	Askaryan Radio Array
ARIANNA	Antarctic Ross Ice Shelf Antenna Neutrino Array
AURA	Antarctic Under-Ice Radio Array
CC	Charged current
CODALEMA	COsmic Detection Array with Logarithmic ElectroMagnetic Antennas
CoREAS	Corsika-based Radio Emission from Air Showers
CORSIKA	COsmic Ray SIMulations for KAscade
CR	Cosmic ray
DPMJet	Dual Parton Model with Jet production
GRAND	Giant Radio Array for Neutrino Detection
GSM	Galactic Sky Model
Hpol	Horizontal polarized (antennas)
IGLU	In-ice Gain with Low-power Unit
KASCADE	KARlsruhe Shower Core and Array DETector
LOFAR	LOW Frequency ARray
LOPES	LOFAR PrototypE Station
LPDA	Logarithmic Periodic Dipole Antenna
LPM effect	Landau–Pomeranchuk–Migdal effect
MCEq	Matrix Cascade Equations
NC	Neutral current
QGSJET-II	Quark-Gluon-String model with Jet production
RICE	Radio Ice Cherenkov Experiment
RNO-G	Radio Neutrino Observatory Greenland
SIBYLL	No acronym. The sibyls were oracles in Ancient Greece
SKA-low	Square Kilometre Array - low
SNR	Signal to Noise Ratio

TAROG	Taiwan Astroparticle Radiowave Observatory for Geo-synchrotron Emissions
TREND	Tianshan Radio Experiment for Neutrino Detection
Tunka-Rex	Tunka Radio Extension
UHE	Ultra high energy
UrQMD	Ultra-relativistic-Quantum-Molecular-Dynamics approach
VEL	Vector Effective Length
Vpol	Vertical polarized (antennas)

## Acknowledgements

As this thesis represents the very last requirement for my masters degree, I would like to thank all the people who where willing to share their knowledge with me, and the people who helped me to process it. Getting into physics research was a big goal of mine, and I am happy that I can now contribute to such a great project.

I would like to express my very great appreciation to my supervisor Anna Nelles, who is able to foresee any problem which may arise. Thank you for having me in your group and provide a surrounding where I could learn and grow.

I would like to offer my special thanks to Anna Franckowiak who stepped in to supervise my work. Thank you also, for providing a first glimpse into the field of astro-particle physics.

I would like to thank the whole RNO-G collaboration based in Europe and the United States, who provided important discussions about the development of RNO-G. Thank you Eric, for answering all the vague electronic questions I had and implementing my suggestions into hardware.

I am particularly grateful for the assistance given by the people at DESY Zeuthen. Thank you Christoph, for always having a good idea how to proceed when I was clueless. Daniel, thank you, for answering my questions so precise and for encouraging me to question also the smallest detail. Thank you Ilse, for make me believe in my abilities and for sharing a creative side. Steffen, thank you, for taking the time to deal with my question and develop reasonable answers. Zack, thank you for the good jokes and an office I am always happy to enter. Nora, thank you for the warm welcome in Erlangen and responding to all the hardware question I had. My special thanks are extended to the other PhD students at DESY Zeuthen, sharing coffee at the lake recharged my batteries.

Finally I have to thank my family and friends who stand by me, even when I disappear into the science world.

## **Selbstständigkeitserklärung**

Ich erkläre hiermit, dass ich die vorliegende Arbeit selbstständig verfasst und noch nicht für andere Prüfungen eingereicht habe. Sämtliche Quellen einschließlich Internetquellen, die unverändert oder abgewandelt wiedergegeben werden, insbesondere Quellen für Texte, Grafiken, Tabellen und Bilder, sind als solche kenntlich gemacht. Mir ist bekannt, dass bei Verstößen gegen diese Grundsätze ein Verfahren wegen Täuschungsversuchs bzw. Täuschung eingeleitet wird.

Berlin,